ISTITUTO NAZIONALE DI FISICA NUCLEARE

Laboratori Nazionali di Frascati

INFN-16-15/LNF
20 Dicembre 2016

The PADME experiment Technical Proposal

Mauro Raggi[1], Venelin Kozhuharov[2], Paolo Valente[3]

[1)] *INFN, Laboratori Nazionali di Frascati, Via E. Fermi 40, I-00044 Frascati, Italy*

[2)] *University of Sofia "St. Kl. Ohridski", Sofia, Bulgaria*

[3)] *INFN, Sezione di Roma, P.le A. Moro, 2, I-00185 Roma, Italy*

Published by
Laboratori Nazionali di Frascati

The PADME experiment Technical Proposal

The PADME Collaboration*

Editors: Mauro Raggi[a,1], Venelin Kozhuharov[b,2],
and Paolo Valente[c,3]

[a] *INFN Laboratori Nazionali di Frascati, Via E. Fermi, 40 – I-00044 Frascati (Rome), Italy.*
[b] *University of Sofia "St. Kl. Ohridski", Sofia, Bulgaria.*
[c] *INFN Sezione di Roma, P.le A. Moro, 2 – I-00185 Rome, Italy.*

January 25, 2016

Istituto Nazionale
di Fisica Nucleare

*The PADME Collaboration

M. Raggi, R. Bedogni, F. Bossi, B. Buonomo, E. Capitolo, C. Capoccia, R. De Sangro, G. Finocchiaro, L. Foggetta, A. Ghigo, M. Palutan, G. Piperno, B. Sciascia, T. Spadaro.

INFN Laboratori Nazionali di Frascati, Via E. Fermi, 40 – I-00044 Frascati (Rome), Italy.

V. Kozhuharov, G. Georgiev, L. Tzankov.

University of Sofia "St. Kl. Ohridski", Sofia, Bulgaria.

P. Valente, F. Ferrarotto, S. Fiore, E. Leonardi, G. Organtini.

INFN Sezione di Roma, P.le A. Moro, 2 – I-00185 Rome, Italy.

G. Chiodini, A. Caricato, M. De Feudis, B. M. Martino, G. Maruccio, A. Monteduro, S. Spagnolo.

INFN Sezione di Lecce, Via Arnesano – I-73100 Lecce, Italy.

U. Dosselli.

INFN Sezione di Padova, Via Marzolo 8, I-35131 Padova, Italy.

Contents

Chapter 1

Executive summary

The long standing problem of reconciling the cosmological evidence of the existence of dark matter with the lack of any (up to now) clear experimental observation of it, has recently revived the idea that the new particles are not directly connected with the Standard Model (SM) gauge fields, but only through mediator fields or "portals", connecting our world with new "secluded" or "hidden" sectors. This concept, which is quite natural in many SUSY models and appears in string theory, is more general and can be realized by adding a new gauge symmetry to the SM. One of the simplest models just adds an additional $U(1)$ symmetry, with its corresponding vector boson. All SM particles will be neutral under this symmetry, while the new field will couple to the charged particles of the SM with an effective charge ϵe, so that this new particle is often called "dark photon" (or U boson, or also A').

Additional interest arises from the observation that such a new particle, in particular a dark photon in the mass range 1 MeV/c^2 to 1 GeV/c^2 and coupling $\varepsilon \sim 10^{-3}$, would justify the discrepancy between theory and observation for the muon anomalous magnetic moment, $(g-2)_\mu$.

Up to now, almost all direct searches have been performed in colliding-beams and fixed target experiments, by producing the dark photon in the analogous of the Bremsstrahlung process ($e^-(Z) \to e^-(Z)A'$) or of neutral meson electromagnetic decays ($\pi^0, \eta \to \gamma A$), and then looking at its decay back to SM particles, i.e. $A' \to e^+e^-$ and, for masses higher than $2m_\mu$, $A' \to \mu^+\mu^-$. These experiments provide quite stringent limits, in particular the $(g-2)_\mu$ band has been practically ruled out. However, all these measurements rely on the strong assumption that no particle lighter than the A' exists in the hidden sector. In this other more general – and probably more interesting case – the branching fraction to SM particles will be suppressed by a factor ϵ^2, and the dark photon would dominantly decay in "invisible" particles in the hidden sector.

An alternative approach, so far not exploited by any experiment, would be to use the lower cross-section annihilation process (analogous of the pair production): $e^+e^- \to \gamma A'$. In such a fixed target experiment, knowing the quadri-momentum of the incoming positron and by measuring the quadri-momentum of the SM photon, one can search for a non-zero missing mass: $M^2_{miss} = P_{e+} - P_\gamma$.

The idea at the basis of the PADME experiment is then to exploit the possibility of producing a positron beam with well defined and easily tuneable parameters, using the LINAC of the DAΦNE accelerator complex, and the extraction line of the Beam-Test Facility (BTF), mainly with the objective of extending the exclusion – or even better, aiming at the discovery – of a dark photon in a relevant part of the mass and coupling range interesting for the $(g-2)_\mu$ problem.

The basic elements of the experiments are: a well defined positron beam, striking a very thin, active target, capable of monitoring the interaction point, a vacuum region for avoiding spurious positron interactions, a sweeping magnet – with the additional task of measuring the momentum of the interacting positrons, thus improving the rejection of the Bremsstrahlung background – and a fine-segmented, high-resolution calorimeter, for reconstructing the momentum of the single SM photon. In order to reduce the Bremsstrahlung rate in the inner part, the calorimeter has a central hole, shadowed by a smaller, fast "small angle" calorimeter.

The electron beam from the DAΦNE LINAC can produce 40 ns long positron pulses at 50 Hz, of energy up to 650 MeV, with an intensity of $\approx 10^4$ particles/bunch. We expect to collect 10^{13} positrons on target in a run of 1–2 years, thus allowing us to reach the $\epsilon \sim 10^{-3}$ sensitivity up to a dark photon mass of ≈ 26 MeV/c^2. This performance can be further improved by upgrading the LINAC: in terms of sensitivity by extending the beam pulse above 40 ns (we expect to reach at least the 200 ns range), thus allowing scaling the statistics keeping the same pile-up probability, and in terms of mass reach, by upgrading the maximum energy (by reaching the GeV limit we can extend up to 32 MeV/c^2).

The main element of the experiment is, also from the point of view of the cost, the calorimeter. In order to keep under control the pile-up due to multiple interactions of the positrons with the target, it is desirable to have a very fast photon detector. This requirement restricts the choice for the calorimeter material to inorganic scintillating crystals. We have the opportunity of reusing the BGO crystals from the electromagnetic calorimeter of the former L3 experiment at LEP. The final choice of the calorimeter size, granularity and distance from the target (in order to have a sufficiently high acceptance) will be driven by the total number of crystals available.

One other important element, from the point of view of cost and also complexity, is the sweeping/analysing magnet. We have agreed with CERN the loan of an existing spare dipole from the SPS transfer line, capable of providing the required field (of order 0.4 T) over a quite wide gap (20 cm height) and length (1 m), which is suited to the present design of the PADME experiment. The side of the magnetic field region will be instrumented with segmented scintillators, in order to detect positrons having lost energy by Bremsstrahlung radiation, and thus being more curved inside the magnetic field. However, only positrons with a radius of curvature large enough to be inside the magnet acceptance will be detected. A large fraction of the Bremsstrahlung spectrum is instead very soft ($1/E_\gamma$), so that the irradiating positron stays very close to the nominal $E = E_0$ trajectory. We are then considering to add another veto detector, with high-resolution 2D imaging capability (e.g. a Silicon pixel detector), to be placed inside the not interacted beam.

The active target, which is a very small device, from the detector technology point of view is challenging. In order to optimize the dark photon cross section with respect to the SM electromagnetic background, the basic requirements are: lowest possible Z, and high density. We also require the capability of detecting the position and the intensity of the incoming positrons, in order to monitor the beam variation during the data taking. We are considering as baseline option a polycrystalline synthetic diamond segmented in x and y grafitized strips (for reading out the signal), of 50 μm thickness.

In this Technical Proposal we describe the full experimental setup, based on the requirements of the $A' \to$ "invisible" experiment, with a baseline choice of all the detectors and elements of the experiment. In some cases the choice is quite robust and based on detailed studies, sometimes already on an advanced design, in some other cases we feel that more investigation would be necessary, in order to optimize both the performance and the cost of the experiment, and we have thus indicated an alternative solution. We have tried, for the latter cases, to keep the basic requirements fixed, so that the target experiment sensitivity is guaranteed, although with not negligible differences in terms of complexity, time needed for development and realisation, and – last but not least – cost.

Chapter 2

The dark photon physics

2.1 Secluded sector extensions of SM

The most general low energy extensions of the Standard Model (SM) are so called “dark sectors” due to their extremely weak interaction with the known Standard Model sector. The dark sectors could consist of rich phenomenology and states. The connection between the standard sector and the dark sector is usually obtained through a mediator - a particle which possesses both SM and dark sector quantum numbers. Alternatively the SM fields could have charge (either direct of an effective charge induced through loops or mixing) under the newly introduced interactions among the dark sectors. Both scenarios are viable and a few categories of models depending on the spin and parity of the mediator are on the market. The most common limitation is to consider only extensions with operators in the Lagrangian with dimension at most four, to simplify the picture and to give a separate attention to the infrared physics only.

Depending on the type of the mediator few “portals” to the hidden sector could be identified [1]:

- Scalar portal: The most general scenario employing an additional scalar particle is through its interactions with the Standard Model Higgs boson. This includes both operators of third and fourth order resembling the Higgs potential in the Lagrangian:

$$\mathcal{L} \sim \mu S H^{+} H + \lambda S^{2} H^{+} H. \tag{2.1}$$

  Since the best way to look for such type of new particles is through the study of Higgs decay final states and Higgs properties, the best machines to address this scenario are of course high energy colliders.

- Pseudoscalar portal: A solution to the strong CP problem is the introduction of a new Peccei-Quinn global $U(1)$ symmetry which is broken spontaneously. The pseudo Nambu-Goldstone boson of this breaking is the axion. The interaction between the axion and the Standard Model fermions is given by a term in the Lagrangian like:

$$\mathcal{L} \sim \frac{\partial_{\mu} a}{f_a} \bar{\psi}_f \gamma^{\mu} \gamma_5 \psi_f. \tag{2.2}$$

  While the parameters of the axion, its mass M_a and coupling α_a to ordinary SM fields, are functions of the breaking scale f_a of the Peccei-Quinn symmetry, other axion-like particles (ALPs) may well exist and their parameters are free. The couplings of the ALPs to photons and SM fermions are also arbitrary.

- Neutrino portal: The existing puzzle in the neutrino mass sector provides input for few interesting models explaining this phenomena. A possible existence of a sterile neutrino may lead to the addition of Yukawa terms:

$$\mathcal{L} \sim Y_N LHN. \tag{2.3}$$

  This sterile neutrino is SM singlet and could be produced in the early Universe. If the relic abundance and interactions strength with the dark matter are sufficient they will delay the dark matter kinetic decoupling and will allow the solution of the problem with the missing small scale structures like satellite galaxies [2].

- Vector portal:

  The most general interaction of the dark photons with the Standard Model fermions can be written in the form:

$$\mathcal{L} \sim g' q_f \bar{\psi}_f \gamma^\mu \psi_f A'_\mu, \tag{2.4}$$

  where g' is the universal coupling constant of the new interaction and q_f are the corresponding charges of the interacting fermions.

In addition to the possibilities described so far other new interactions may also involve existence of new particles interacting with SM fermions. They could be made anomaly-free (like in the case of B-L as a gauge symmetry) and then the interaction term could be of order $D \leq 4$. The tree level process may again proceed through vector particles that are neutral under any of the SM gauge groups.

The vector portal offers a very rich phenomenology and has been recently extensively tested experimentally at low energies. This scenario may include also any of the possible new interactions involving neutral mediators. All they may be grouped in the so called dark photon (DP) models. They do not require the introduction of UV physics and can be probed efficiently at high intensity and low energy machines.

2.2 Dark photon models

The dark photon model predicts the existence of a new neutral vector particle (A') which has a non vanishing coupling to the SM fermions of the form described in equation (2.4). This A' could itself be the mediator between the visible and the dark sector but the mediation can also be realised in different ways.

The origin of the coupling of A' to the fermion fields could originate different models. Since almost any extension of the Standard Model introduces new symmetries and gauge groups, the wide range of possibilities go from maximally universal models to including only single type of fermions (leptons or quarks) or even a single generation. Few examples of these models are presented below to illustrate the variety of possibilities presently explored by theoreticians.

2.2.1 Kinetic mixed dark photon

One of the simplest and best motivated dark photon models is the so-called "kinetic mixing" model, in which a new $U(1)'$ group is introduced that is responsible for the interactions between the particles in the dark sector. It mimics the Standard Model hypercharge interaction and its carrier, the dark photon (A', also called U-boson, dark boson, secluded photon), could mix with the ordinary photon [3], [4, 5]:

$$\mathcal{L}_{mix} = -\frac{\epsilon}{2} F_{\mu\nu} F'^{\mu\nu}. \tag{2.5}$$

When the electroweak symmetry breaks, this introduces an effective interaction between the fermions and the dark photon in the form

$$\mathcal{L} \sim \epsilon e \bar{\psi} \gamma^{\mu} \psi A'_{\mu}, \tag{2.6}$$

where the charges of the individual fermions are exactly the electromagnetic ones. In this scenario the new interaction couples with the same strength to both leptons and quarks. All the processes are therefore determined by a single new parameter, the mixing stregth ϵ, and this explains the predictive power of the kinetic mixing model.

The dark photon could be either massive or massless, as in the case of [4]. The mass term of the dark photon breaks the gauge invariance of the dark interactions and can be generated through different mechanisms. In the minimal dark photon model the mass term of the gauge vector field A' is introduced through an interaction term of A' with a scalar of the form:

$$\mathcal{L}_{mass} \sim \frac{1}{2}(\partial^{\mu}\alpha + mA'^{\mu})(\partial_{\mu}\alpha + mA'_{\mu}). \tag{2.7}$$

In unitary gauge the Stückelberg mechanism leads exactly to the well-known mass term for spin-1 field. In this case there are no extra particles needed to have massive dark photon, leaving the phenomenology of the model unchanged. Other possibilities, such as the introduction of a new scalar dark Higgs or the introduction of a coupling of the A' to the Standard Model Higgs, have been also explored. In both cases the introduction of new degrees of freedom modifies the resulting phenomenology with respect to the minimal kinetic mixing model.

The kinetic mixing model may include also other dark sector particles, χ, which couple without suppression with the dark photon.

2.2.2 Non-Kinetic mixed dark photon

2.3 Dark photon production

The production of kinetic mixed A' can arise through a variety of mechanisms and its estimation is not that straightforward in most of the cases. Few particular cases have been recently deeply investigated: dark photon production in meson decays, in lepton-on-target experiments, and in proton on target experiments. We concentrate our attention only on the production in electron-positron on target collision which is relevant for the PADME proposal.

Being mixed with the Standard Model photon, the A' also shares its production mechanisms in e-on-target collisions: Bremsstrahlung and annihilation processes (Fig.).

In analogy with photon Bremsstrahlung the A' could be emitted in the so called A'-strahlung. The production rate is calculated in the Weizsäcker-Williams approximation [12]. If the electron energy is E_0 and the dark photon is emitted with energy $E_{A'} = xE_0$ then the differential cross section is:

$$\frac{d\sigma}{dx\, d\cos\theta_{A'}} \approx \frac{8Z^2\alpha_{QED}^3\epsilon^2E_0^2x}{U^2}\frac{\chi}{Z^2} \times \left[(1-x+x^2/2) - \frac{x(1-x)m_{A'}^2E_0^2x\theta_{A'}^2}{U^2}\right], \tag{2.8}$$

where $\theta_{A'}$ is the emission angle of A' with respect to the incoming electron, Z is the atomic number of the target material,

$$U = U(x, \theta_{A'}) = E_0^2x\theta_{A'}^2 + m_{A'}^2\frac{1-x}{x} + m_e^2x, \tag{2.9}$$

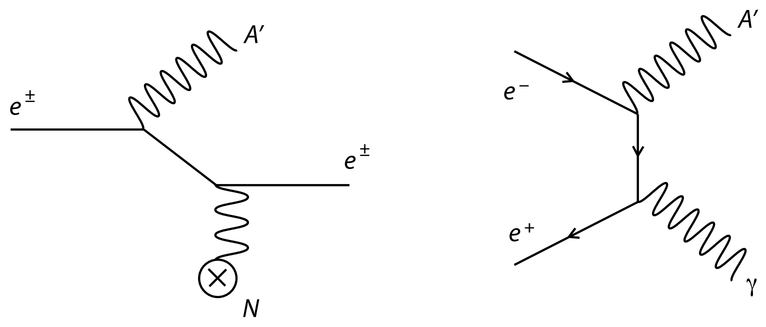

Figure 2.1: The A' production processes: on the left the Bremsstrahlung $e^{\pm}N \to Ne^{\pm}A'$ and on the right the annihilation $e^+e^- \to \gamma A'$.

and for given nuclei:

$$\chi = \chi(E_0, m_{A'}) = \int_{t_{min}}^{t_{max}} dt \frac{t - t_{min}}{t^2} G_2(t). \tag{2.10}$$

where $t_{min} = (m_{A'}^2/2E_0)^2$, $t_{max} = m_{A'}$, and $G_2(t)$ is a general electric form factor [12]. This widely used approximate formula, however, could lead to up to 30% overestimation of the cross section for low $O(1)$ GeV beam energies [13].

Another possibility for leptonic production of dark photon is through annihilation process, in electron positron collisions. This can be obtained both using e^+e^- colliders or positron beams impinging on a fixed target. For center of mass energy s large compared to $2m_e$ and $m_{A'}$ so that both may be disregarded, the cross section is $2\epsilon^2$ times the ordinary process:

$$\sigma(e^+e^- \to \gamma A') = 2\epsilon^2 \sigma(e^+e^- \to \gamma\gamma). \tag{2.11}$$

If $m_{A'}$ cannot be neglected as compared to the center of mass energy s the cross section can be obtained, neglecting m_e, from [14]:

$$\frac{d\sigma(e^+e^- \to \gamma A')}{d\cos\theta} = \frac{\alpha\epsilon^2}{2s^2(s - m_{A'}^2)} \left(\frac{s^2 + m_{A'}^4}{\sin\theta^2} - \frac{(s - m_{A'}^2)^2}{2} \right) \tag{2.12}$$

which reduces to the previous one for $s >> m_{A'}^2$.

2.4 Dark photon decay modes

Massive kinetic mixed dark photon ($m_{A'} > 2m_e$) decay modes depend upon its mass and can in principle include all pairs of Standard Model leptons and light mesons. In absence of new dark matter states with mass lower than $m_{A'}/2$ the predominant decay is into SM particles "visible decays". On the contrary, if any χ particle exists the decay to SM particles is suppressed by ϵ^2 and the A' predominantly decays in "invisible".

For dark photon masses $m_{A'} < 2m_e$, only the three photon decay, mediated via an electron box diagram, is allowed. The decay length then dramatically increases so that, on the scale of the PADME experiment, the dark photon can be safely considered a stable particle.

2.4.1 The "visible" dark photon decays

The partial decay width of the dark photon visible decays in the case of $M_{A'} > 2m_l$ with a lepton pair in the final state is given by [15]:

$$\Gamma_{A' \to l^+ l^-} = \frac{1}{3}\alpha\epsilon^2 M_{A'}\sqrt{1 - \frac{4m_l^2}{M_{A'}^2}}\left(1 + \frac{2m_l^2}{M_{A'}^2}\right), \tag{2.13}$$

For higher masses A' hadronic decay modes are allowed as well. The partial decay width in this case can be written as:

$$\Gamma_{A' \to had} = \frac{1}{3}\alpha\epsilon^2 M_{A'}\sqrt{1 - \frac{4m_\mu^2}{M_{A'}^2}}\left(1 + \frac{2m_\mu^2}{M_{A'}^2}\right) \times \frac{\Gamma(e^+e^- \to hadrons)}{\Gamma(e^+e^- \to \mu^+\mu^-)}(E = M_{A'}). \tag{2.14}$$

Summarizing equations (2.13) and (2.14) the decay fraction for the DP into SM particles is shown in Fig. 2.2.

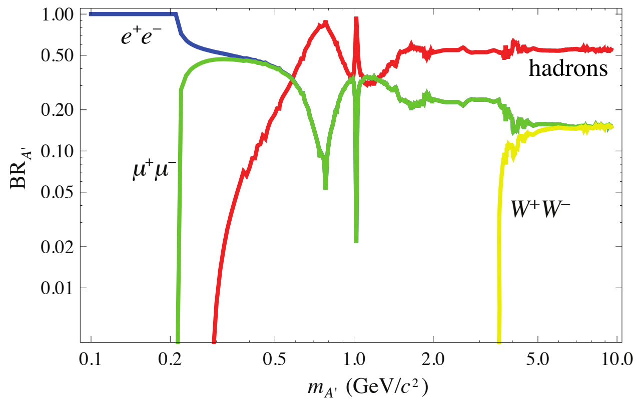

Figure 2.2: Dark photons decay modes and their branching fractions for different dark photon mass values.

The dark photon lifetime will be proportional to $1/(\epsilon^2 M_{A'})$ and the particle is relatively long lived. The very wide panorama of final states for the "visible decays" allowed for the exploration of a significant part of the parameter space by using existing datasets, together with several dedicated experiments.

2.4.2 The "invisible" dark photon decays

As mentioned, the kinetic mixing model may include also other dark sector particles, χ which are lighter than the A' and couple without suppression to it. If the mass of those particles is lower than $m_{A'}/2$ then the DP dominant decay rate to χ is given by [16]:

$$\Gamma_{A' \to \chi\chi} = \frac{1}{3}\alpha_D M_{A'}\sqrt{1 - \frac{4m_\chi^2}{M_{A'}^2}}\left(1 + \frac{2m_\chi^2}{M_{A'}^2}\right), \tag{2.15}$$

where α_D is the coupling constant of the dark photon to the dark sector. An interesting possibility appears when $\alpha_D >> \alpha\epsilon^2$ and $m_\chi < 1/2m_{A'}$. Such scenario is natural since there is no necessity to suppress the interactions in the hidden sector. The DP will then decay promptly into dark matter particles $A' \to \chi\chi$, being its lifetime proportional to $1/(\alpha_D M_{A'})$, escaping undetected by most of the present experiments.

Chapter 3

Experimental status of dark photon searches

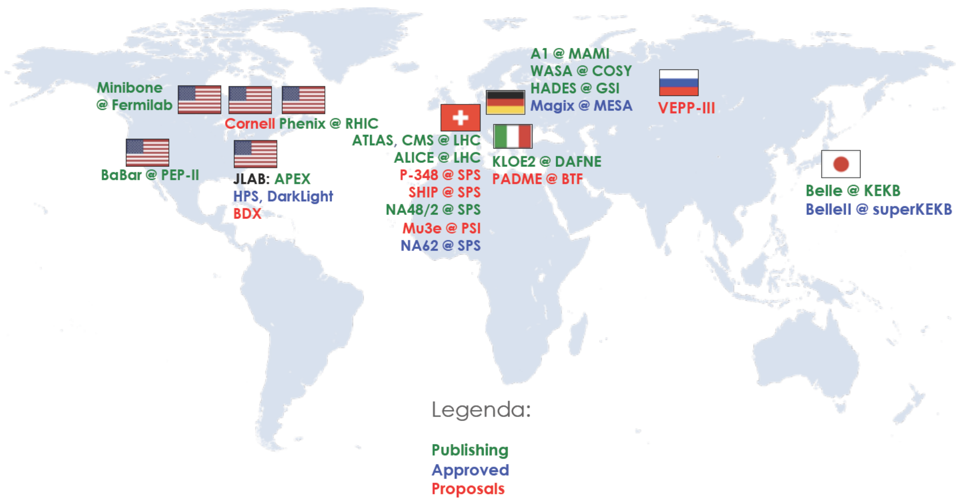

Figure 3.1: Map of the most important experiments working on dark photon searches.

The massive dark photon models ($M_{A'} > 2m_e$) are very predictive and the associated phenomenology is therefore very rich. This encouraged a large number of experimental searches exploiting very different techniques, together with the study of data samples collected from the flavour physics experiments of last decade (BaBar, NA48, KLOE). The main effort in searching for the dark photon is at present concentrated in the United States and in particular at the Jefferson Laboratory, but new initiatives are populating Europe as well (see Fig. 3.1).

Generally, the biggest uncertainty in the experimental results interpretation is related to the existence or the lack of new light states χ charged under the new $U(1)$ symmetry, which would open additional dark decay channels changing the exclusions panorama. For this reason exclusion limits have to be carefully interpreted comparing underlining hypotheses to avoid confusion. Two major categories of models are identified, “visible” or “invisible”, on the basis of the DP decay modes, depending on whether the existence of light dark matter states χ is allowed or not. Visible decay models, even if more popular, are less general because there is no reason a priori to assume that the DP is the lightest state in the dark sector.

3.1 Present status of "visible" dark photon searches

The experiments devoted to visible decay searches rely on the assumption that the dark photon is the lightest state of the dark sector and is therefore forced to decay into Standard Model particles. Regardless of its mass the DP always has a significant decay fraction into lepton pairs and at low masses the BR fraction is dominated by electron and muon pairs decays. A lot of experimental activity, using already collected data samples and dedicated experiments, has been searching for the decay $A' \to e^+e^-$ or $A' \to \mu^+\mu^-$, recently allowing to completely exclude the $(g-2)_\mu$ favoured parameter region in the hypothesis of decays into Standard Model particles.

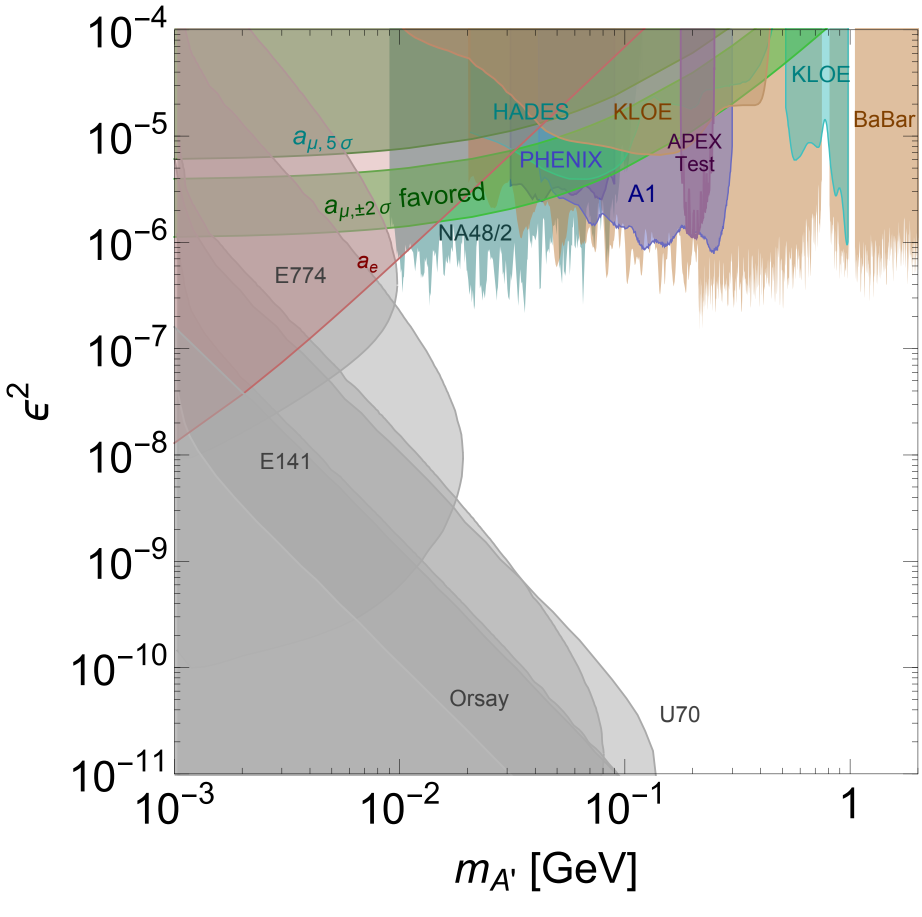

Figure 3.2: Constraints in the ϵ^2 versus $M_{A'}$ plane for dark photons that decay directly to SM particles in the region of interest for the PADME proposal (Figure adapted from [8]).

All of the measurement collected in Fig. 3.2 can be classified, according to the applied technique, into three different categories: dump experiments (grey), fixed target experiments, meson decay experiments. Being limited by different production and detection technique they populate different regions of the plot mass vs. coupling shown in Fig. 3.2.

Despite the fact that the region preferred by muon $g-2$ has been recently completely covered, the interest in searching for dark photon decaying into Standard Model particles is still high due to a large part of the parameter space still to be explored. In fact, although the opportunity to explain the present muon $g-2$ anomaly through the dark photon was an exciting perspective, there are still many SM anomalies that can be clarified by dark sector models and therefore the physics case for DP searches with "visible" decay technique is still very clear. For this reason several laboratories are planning to explore dark photon parameter space with dedicated experiments in the next decade.

A dedicated run to search for the dark photon visible decays with the PADME experimental setup up requires the construction of a magnetic spectrometer to reconstruct e^+e^- pairs invariant mass and a new dedicated target. Nevertheless preliminary studies shows that the experiment could access a still unexplored region of the parameter space in 1 year of data taking.

3.2 Present status of "invisible" dark photon searches

The invisible decay searches are based on the hypothesis that at least one new dark sector particle χ of mass lower than $m_{A'}/2$ exists in the dark sector. Under this rather general assumption the DP predominantly decays in the non SM states, escaping detection in past experiments. All decays into Standard Model particles are therefore suppressed by a factor ϵ^2 strongly reducing the effectiveness of the visible decay searches. As a result, the parameter space for invisible decays is much less constrained by direct searches as shown in Figg. 3.3 and 3.4.

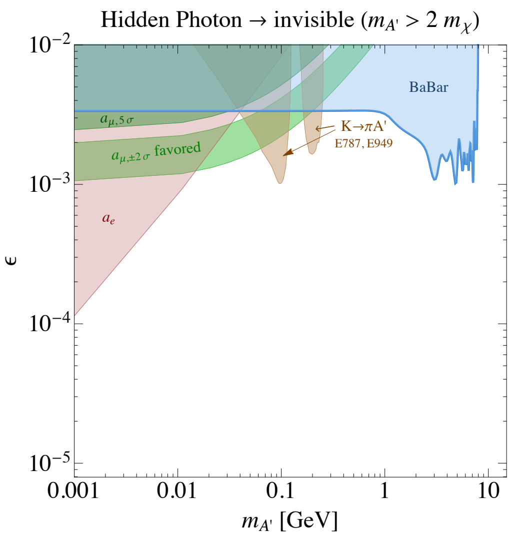

Figure 3.3: Exclusion limits for $A' \to \chi\bar{\chi}$ through missing mass searches.

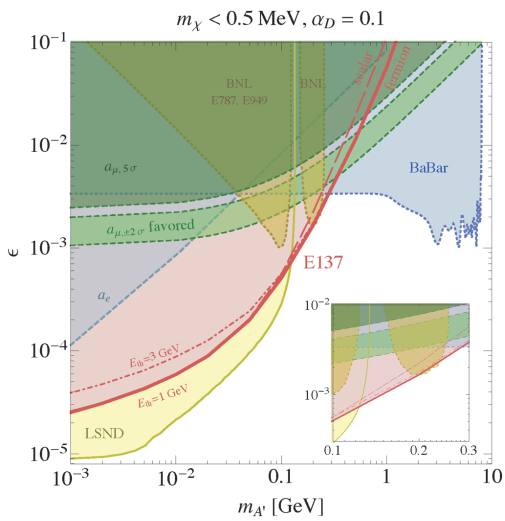

Figure 3.4: Exclusion limits for $A' \to \chi\bar{\chi}$ through dark matter scattering process.

3.2.1 Invisible decay search techniques

There are several experimental strategies proposed so far to detect the DP in this scenario: the first one consists in detecting the dark matter particles χ obtained in the decay of DP produced by A'-strahlung into a dump, by means of their scattering into a massive downstream detector. The second technique consists in searching for missing mass into kinematically constrained processes regardless of the A' decay chain. Being described by different models involving different number of free parameters, the exclusions obtained with the two different techniques cannot be directly compared. For this reason they are represented in two different diagrams in Figg. 3.3 and 3.4. Indirect limits coming from $(g-2)_\mu$ and $(g-2)_e$ and Kaon decays are common to both scenarios.

Dark matter scattering searches

The process under investigation consists of two steps described in Fig. 3.5. A beam of dark matter particles χ is obtained through the decay of A' produced in a target through A'-strahlung process, Fig. 3.5 a). The mechanism of dark photon production is described by the parameters ϵ^2 and $M_{A'}$. The dark matter particles can traverse the beam dump due to their weak interaction with ordinary matter and can then be detected through their scattering with nuclei in a dense downstream detector, Fig. 3.5 b).

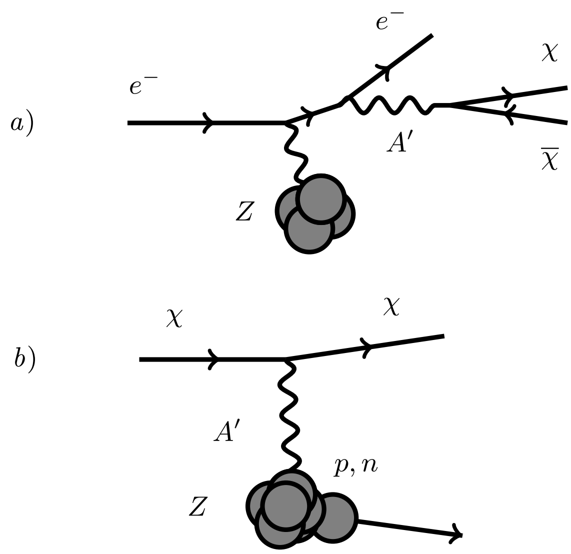

Figure 3.5: a) $\chi\chi$ pair production in electron-nucleus collisions. b) χ scattering off a detector nucleus and liberating a constituent nucleon.

If $m_{A'} < 2m_\chi$, the dominant χ production mechanism in an electron fixed-target experiment is the radiative process with off-shell A'. In this regime, the χ production yield scales as $\sim \alpha_D\epsilon^2/m_\chi^2$. If $m_{A'} > 2m_\chi$, the secondary χ-beam arises from radiative A' production followed by $A' \to \chi\bar{\chi}$ decay. In this regime, the χ production is proportional to $\epsilon^2/m_{A'}^2$. The χ-nucleon scattering in the detector via A' exchange occurs with a rate proportional to $\alpha_D\epsilon^2/2m_{A'}^2$ over most of the mass range.

The combination of the two steps lead to a suppression factor $\epsilon^4\alpha_D/m_{A'}^4$ for the on-shell production, and therefore a very large number of primary particles are necessary. The only possible approach in this case is to dump an extremely intense beam on a high Z thick target. The A'-strahlung production allows to reach high dark photon masses, giving a high discovery potential to this technique. On the other hand, the four parameter space involved in the model, limits somehow its exclusion power.

Recently the experiments E137 and LSND have been reinterpreted [17] in terms of this model leading to the exclusions limits in Fig. 3.4 for the fixed values of $\alpha_D = 0.1$ and $m_\chi < 0.5$ MeV. The

Liquid Scintillator Neutrino Detector (LSND) was a scintillation counter at Los Alamos National Laboratory. It used a 800 MeV proton beam on two different targets over its lifetime, water and a high-Z metal. The experiment collected data from 1993 to 1998. The detector consisted of a tank filled with 167 tons of mineral oil and 6.4 kg of b-PDB organic scintillator material. Cherenkov light emitted by particle interactions was detected by an array of 1220 photomultiplier tubes. LSND sets a strong constraint (yellow region/solid line) [17] if A' interacts with both electrons and quarks (as it would for the kinetic mixing model, but not for example in the case of a leptophilic mediator). Here χ is produced through the cascade decays of neutral pions produced in the proton-target collisions,$\pi^0 \to \gamma A'$ $A' \to \chi\bar{\chi}$ and detected via its scattering with electrons.

For the computation of the detector acceptance all the results of the scattering exclusions, shown in Fig. 3.4, rely on the additional assumption that in the dark sector there is just a single stable state χ lighter than the A'. If this is not the case, exclusion limits boundary may look rather different.

Searches for the dark photon at MiniBooNe

A proposal to search for dark matter at MiniBooNe has been submitted to the FNAL PAC at the end of 2013. The collaboration requests running to collect a total of $2.0{\cdot}10^{20}$ protons on target (POT) in beam off-target mode [18].

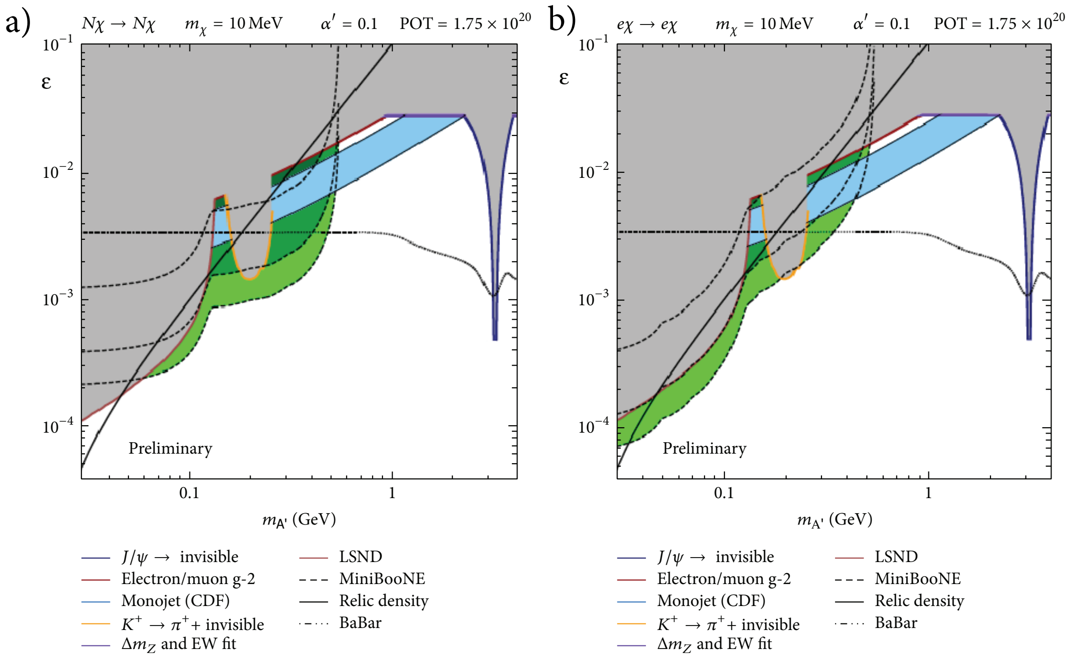

Figure 3.6: a) MiniBooNe expectation for χ nucleus scattering collisions. b) MiniBooNe expectation for χ electron scattering collisions.

The dominant production mode of dark matter particles at MiniBooNe is decays of the mediator particles created by decays of neutral mesons. The dark matter particles can be also made through the direct collisions of protons on the beam dump. The MiniBooNe dark matter search accessible phase space is shown in Fig. 3.6). Here, on the x axis is the dark photon mass, while on the y axis is the kinetic mixing parameter ϵ, assuming the dark matter mass m_χ= 10 MeV and the gauge coupling α_D= 0.1. MiniBooNe exclusion region can be seen in green. MiniBooNe has collected $1.86{\cdot}10^{20}$ POT during a 10 months run in beam off-target mode to reduce neutrino background. Preliminary analysis on 17% of data taking is ongoing to tune the background evaluation. First results are expected for the end of 2015.

Missing mass based searches

The missing mass technique is based on the direct detection of the A' through the measurement of its mass as a missing mass in kinematically constrained final states. Ignoring the decay products of the A', the exclusions provided by this technique can be described with a simplified model using only ϵ^2 and $M_{A'}$ parameters. The production of the A' through e^+e^- annihilation limits the accessible mass region for low energy colliders while the use of meson decays limits the statistical sensitivity due to the relevant meson production cross section. Recently, invisible experiments based on missing energy detection in Bremsstrahlung production have been proposed as well [21]. The exclusion limits obtained in [21] are impressive even if the proposed technique appears to be very challenging from an experimental point of view.

The only limit coming from experimental search in Fig. 3.3 is a preliminary result presented by by BaBar [22] at ICHEP 2008, recently reinterpreted in terms of dark photon exclusion in [23]. The BaBar collaboration performed a bump hunt search for a light scalar particle produced in single-photon decays of the Υ(3S) resonance through the process $\Upsilon(3S) \to \gamma + A^0, A^0 \to$ invisible using a data sample collected with a single photon trigger. They find no evidence for such a processes in a sample of $122 \cdot 10^6$ $\Upsilon(3S)$ decays, setting a preliminary upper limit on its Branching Ratio in the mass range $M_{A^0} < 7.8$ GeV. Reinterpretation in terms of dark photon model led to the exclusion region in blue in Fig. 3.3.

The BESIII experiment has published a search for invisible decays of the η and η' mesons, motivated by the possible existence of light neutral dark matter particles [24]. A sample of $J/\psi \to \Phi\eta(\eta')$ and missing energy is selected by tagging the Φ. No significant signal is observed, and 90% CL limits on the branching ratio $BR(\eta(\eta') \to$invisible) are set. These bounds constrain the invisible dark photon decays through η $(\eta') \to A'A'$, $A' \to$invisible, and cover therefore a very narrow region of the parameter space (see Fig. 3.6).

Indirect limits

In both Fig. 3.3 and Fig. 3.4 additional indirect limits are present. The limits coming from the muon $g-2$ anomaly are still valid in case of invisible DP decays. In addition, bounds to DP invisible decays can be obtained from the process $K^\pm \to \pi^\pm A'$. Authors of [9] computed the rate to be:

$$\Gamma(K^\pm \to \pi^\pm A') = \frac{\epsilon^2 \alpha W^2 m_{A'}^2}{2^{10}\pi^4 m_K^7}\sqrt{\lambda(m_K^2, m_\pi^2, m_{A'}^2)}[(m_K^2 - m_\pi^2)^2 - m_{A'}^2(2m_K^2 - 2m_\pi^2) - m_{A'}^2] \quad (3.1)$$

The BNL E949+E787 combined measurement of $BR(K^+ \to \pi^+\nu\bar{\nu})$ [25] is used to derive the upper bound for the $BR(K^\pm \to \pi^\pm A')$ process. The CERN NA62 experiment [6] will improve the sensitivity in this channel by measuring $BR(K^+ \to \pi^+\nu\bar{\nu})$ with a 10% precision. These kind of limits are however model dependent. In fact if a mass mixing with Standard Model Z-A' is introduced in the model, the bound from $K \to \pi + nothing$ can be weakened by a factor up to ~ 7 as pointed out in [9].

3.3 The PADME physics case

The PADME proposal aims to search for dark photons produced in e^+e^- annihilation process $e^+e^- \to \gamma A'$ through a missing mass search technique by using the positron beam of the DAΦNE LINAC [10]. The experimental technique rely on the detection of the SM recoil photon by a finely segmented inorganic crystal calorimeter, measuring the particle four-momentum to a high precision. This approach allows to detect the dark photon even in the case it is a stable particle, or in the case of A' decays to dark sector particles $A' \to \chi\chi$. With the present maximum positron energy of 650 MeV A' (see Sec.4), masses up to 25.8 MeV/c^2 can be explored. This region of the dark photon parameter space is currently unconstrained by direct measurement (see Fig. 3.3) and PADME has the unique chance to be the first dedicated experiment directly searching for the dark photon invisible decays in a model-independent way in that region.

Even if the region of low A' masses is seriously constrained by $g - 2$ exclusions, these model independent indirect limits rely on extremely precise measurements and complicated theoretical calculation. For this reason defining precise exclusion boundaries is rather difficult and a direct measurement will for sure provide precious information to theorists, even if a discovery is not obtained. The region accessible to PADME is in fact very interesting because it covers an important fraction of the parameter space in which the dark photon could provide an explanation to the present $(g-2)_\mu$ anomaly. Therefore the PADME results, together with other initiative in Cornell and the future measurement at BELLE-II, can contribute to completely cover the $(g-2)_\mu$ region, in case ruling out the dark photon as possible explanation of this long standing anomaly.

Being insensitive to all the new particle characteristic but its mass, the constraints obtained by the PADME experiment can be interpreted in many different scenarios like ALP, dark Higgs and leptonic gauge bosons, whenever a new massive particle is produced.

Another important point in the PADME discovery potential is the very solid experimental technique able to provide very clean observation. In fact if any signal is observed, PADME will be able to measure both the A' mass and the coupling strength ϵ. The determination of the two parameters completely define the new model immediately allowing to compute consequences in many other observables.

Profiting from the presence of an electron beam, background to annihilation can be easily extracted from dedicated electron on target data samples to be compared to positron ones. Moreover any genuine dark photon signal should not appear in the electron data samples in which no annihilation can occur.

Thanks to the possibility of changing the positron beam energy (see Chapter 4), if any region of interest is identified in the A' mass spectrum, the beam energy can be tuned in order to profit from A' production cross section resonant enhancement, thus allowing to falsify possible background fluctuation effects.

Finally, any observation at PADME will provide the center of mass value of the dark photon resonant production, allowing other laboratories to cross-check any claim for discovery.

Bremsstrahlung production provides the PADME experiment with the opportunity to search for a dark photon in visible decays as well. In this case the present constraints are much stronger (see Fig. 3.2) and dedicated sensitivity estimates are still ongoing. Nevertheless preliminary studies show that a dump experiment using slightly modified PADME detector and 10^{20} electrons on target could provide access to unexplored regions of the parameter space in case of decays to lepton pairs as well.

3.4 Additional dark sector searches at PADME

The PADME experiment sensitivity to dark photon models is extensively explored in the present proposal but this is not the unique New Physics model accessible with the PADME experiment. In fact any new particle having a coupling to the electrons can be produced in the collisions of the positron beam on the PADME target. Being the PADME experiment able to detect both charged and neutral particles, final states with new particles decaying into SM leptons of photon can be explored as well. This is the case for example of dark Higgs models or axion-like particle (ALP) models.

3.4.1 Dark Higgs models

In models where the dark photon mass is generated through spontaneous symmetry breaking a dark Higgs (h') is introduced in the dark sector together with the DP. In these non minimal models an associate production of the dark Higgs and the dark photon is possible. In the PADME beam the so called Higgs-strahlung process can be realized:

$$e^+ + e^- \to A'h', \ \textbf{with}\ h' \to A'A', \tag{3.2}$$

Naturalness requires that the two particles have masses of the same order $m_{h'} \sim m_{A'}$. Most of the searches so far focus on this production channel. However those exclusions depend on the extra parameters $m_{h'}$ and α_D and their exclusion power is reduced with respect to the minimal dark photon model.

Depending on the mass hierarchy of the dark photon and dark Higgs several final states are allowed. In the PADME experiment two final states are of particular interest. If the dark Higgs mass is higher than the dark photon one and A' decays to Standard Model leptons, the decay chain $e^+ + e^- \to A'h' \to A'A'A' \to 3(e^+e^-)$ is allowed.

The final state with six in time leptons with null total charge can be observed by PADME even just using the electron and positron veto. If the h' is long lived or decays into non SM particles a final state accessible in PADME will be $2(e^+e^-) + X$. In this case the presence of a tracking spectrometer is very important to reconstruct the four leptons invariant mass. Recent status of the dark Higgs searches is can be found in [26]. Dedicated studies are needed to understand the PADME sensitivity and compare to present exclusions by KLOE, BaBar and Belle experiments.

3.4.2 ALP production in PADME

Axion-like particles (ALPs), relatively light (pseudo-)scalars coupled to two gauge bosons and/or two SMfermions, are a common feature of many extensions of the SM. They could be produced in electron positron collision through a virtual off shell photon decaying into a SM photon and an ALP. The ALP can then decay into different SM particles. Of particular interest to the PADME experiment is the reaction described in Fig. 3.7.

In the mass region below 100 MeV the ALP are long lived and would appear as a missing particle in the PADME setup just like invisibly decaying dark photons. For this reason the selection developed for the dark photon can be applied to the searches of ALP as well. Present status of the ALP searches coupling to photons is presented in Fig. 3.8. The new LEP limits in [11] from three and two photons signature are shaded in green and enclosed by dashed and solid black lines, respectively. The region of few to 30 MeV of interest for the PADME experiment has been partially covered by reinterpretation of LEP data. Nevertheless dedicated sensitivity studies for PADME should be carried out to asses the experiment ultimate sensitivity which could even exceed the one obtained with LEP data.

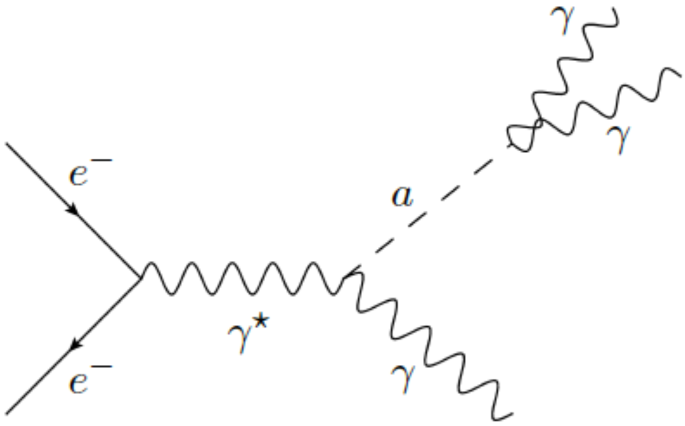

Figure 3.7: Production of ALPs with subsequent decay into two photons.

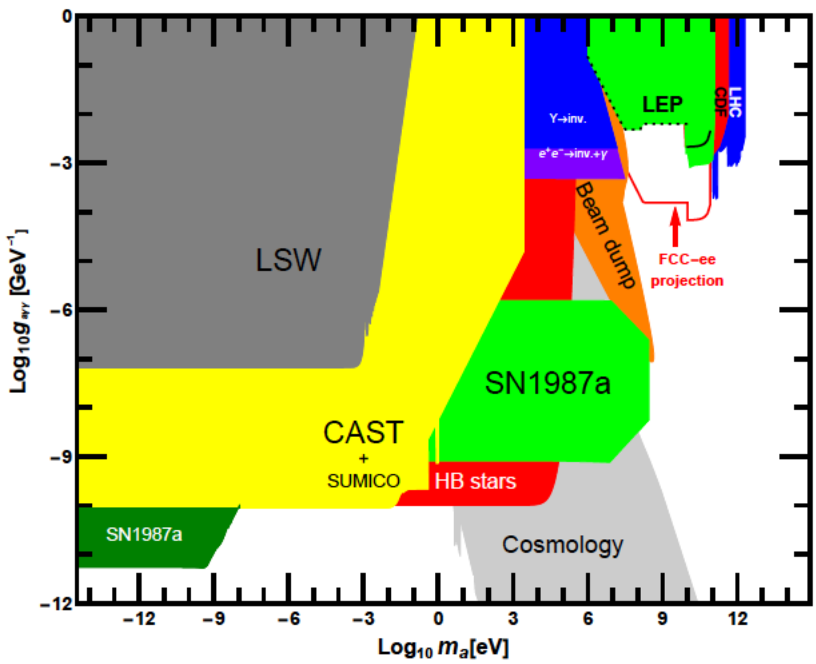

Figure 3.8: Limits on ALP coupling predominantly to photons.

Chapter 4

The PADME beam line

4.1 Requirements for the positron beam

In the PADME approach, a high energy positron beam, with well defined quadri-momentum impinges on a thin, low-Z target, in a well defined position and with the best possible reproducibility. Of course the sensitivity will improve with higher statistics, i.e. with a larger number of interactions of the incoming positrons with the target electrons, but the intensity of the positron beam is ultimately dictated by the pile-up probability in the downstream detector, i.e. the calorimeter for the detection of the SM photon in the $e^+e^- \to \gamma A'$ process.

The pile-up probability, as discussed in 4.2, on the other hand will depend mainly on the timing performance of the calorimeter, i.e. on the characteristic time of the scintillation light, on the risetime and shaping time of the photo-sensors and front-end electronics, etc., but also on the time structure of the beam.

For PADME we propose to use the injector of the DAΦNE e^+e^- collider, located in the Laboratori Nazionali di Frascati (LNF), which is a warm electron LINAC, providing a pulsed positron beam at maximum repetition rate of 50 Hz. The LINAC produces and accelerates electrons and positrons (for collider operation, to an energy of 510 MeV): electrons are emitted at 120 KV by a triode gun, while positrons are produced by electrons, accelerated by the first 4 accelerating sections to ≈ 220 MeV and striking unto a high-Z target, the so-called "positron converter". Electrons and positrons are then injected in a accumulator ring where they are stacked and damped (this ring is thus also called "damping ring"), and from there injected and accumulated in the two main rings of the DAΦNE e^+e^- collider. They can also be extracted to a transfer-line towards the BTF (Beam-Test Facility). A schematic view of the DAΦNE complex is shown in Fig. 4.1.

Having a short pulse with a relatively low repetition rate turns out to be one of the main limitations for the PADME physics reach, as explained in the following paragraphs. Even though the ideal PADME beam would be a continuous or quasi-continuous beam with an average time distance between two positrons larger than the characteristic response time of the calorimeter, it is still possible to perform the PADME experiment at the DAΦNE LINAC, by tuning the beam intensity and width exploiting the flexibility of the BTF beam attenuation system. In the following sections we give a description of the LINAC, of the BTF beam-line and also of some modifications of the infrastructure, aimed at optimizing the positron yield at high energy and the beam parameters for PADME.

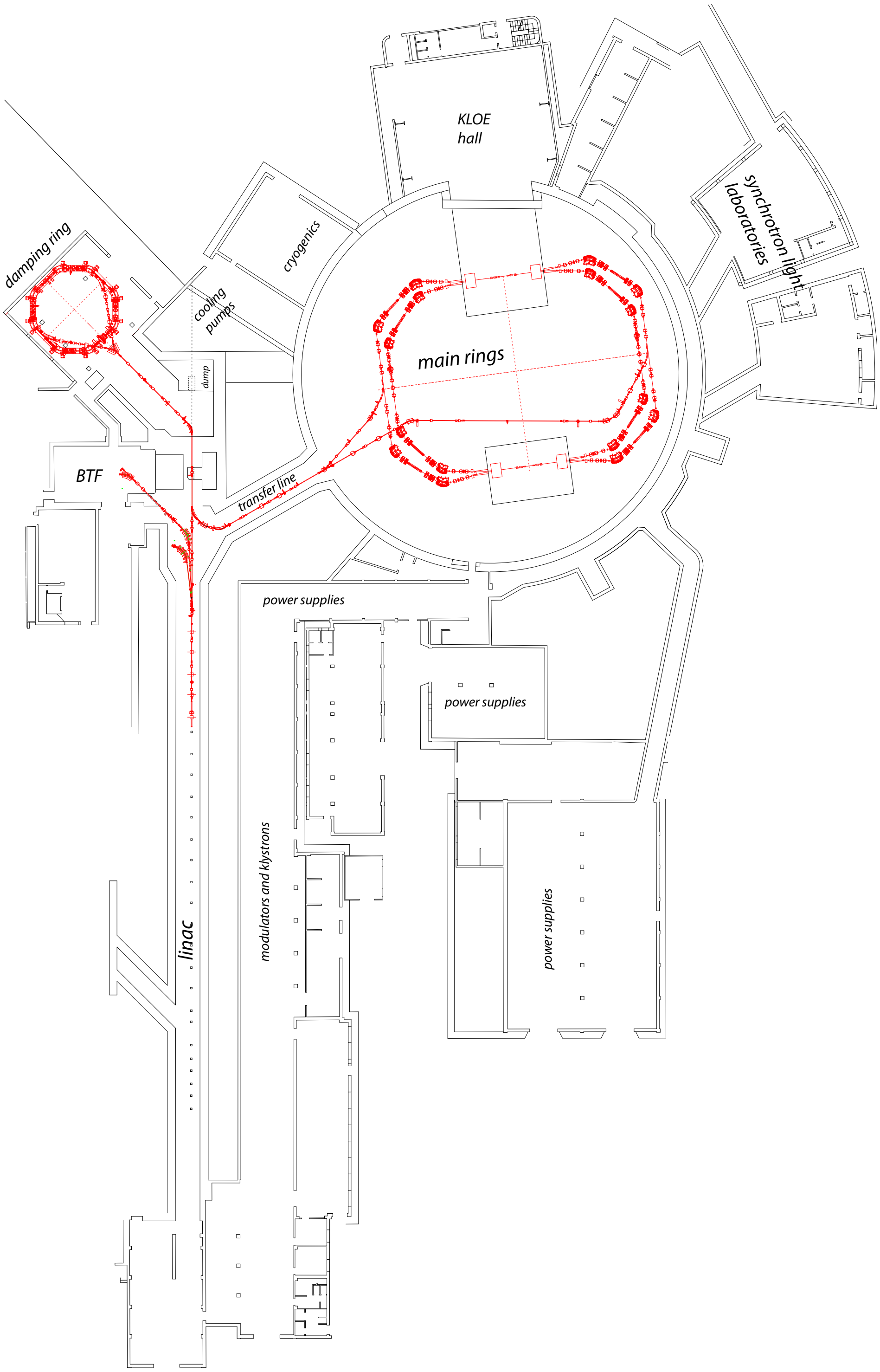

Figure 4.1: The DAΦNE accelerator complex in the Laboratori Nazionali di Frascati (LNF).

4.2 The DAΦNE LINAC

The DAΦNE linear accelerator [27] is a constant gradient, travelling wave, $2/3\pi$, S-band (2856 MHz) LINAC, composed by 15 SLAC-type, 3 m long, accelerating structures, fed by four radio-frequency power stations, each with a modulator supplying a 45 MWp klystron (Thales TH-2128C). As anticipated above, the maximum repetition rate is 50 Hz.

The electron source consists of a gridded triode gun with replaceable cathode. The LINAC has been designed on the model of the two-mile linear accelerator in SLAC, and realized by the TITAN-BETA company; it is operational since 1997. In order to get higher accelerating fields, each klystron is followed by a SLED (SLAC Energy Doubling) system using two coupled cavities, in order to compress the 4.5 μs long RF pulse.

In Fig. 4.2 the configuration of the RF power is shown: three of the klystrons have exactly the same configuration consisting of a vacuum waveguide network with three 3 dB splitters dividing the RF power into four equal parts, each feeding one accelerating section. Half of the power of the fourth klystron is sent to the capture section (CS), the one just downstream the positron converter (PC), while the remaining half is equally divided between two branches: one feeding the P1 section, the other one feeding the pre-buncher, the buncher and the E1 section. With this RF configuration, the nominal accelerating component of the electric field is 24 MV/m in the CS and 18 MV/m in the remaining accelerating sections.

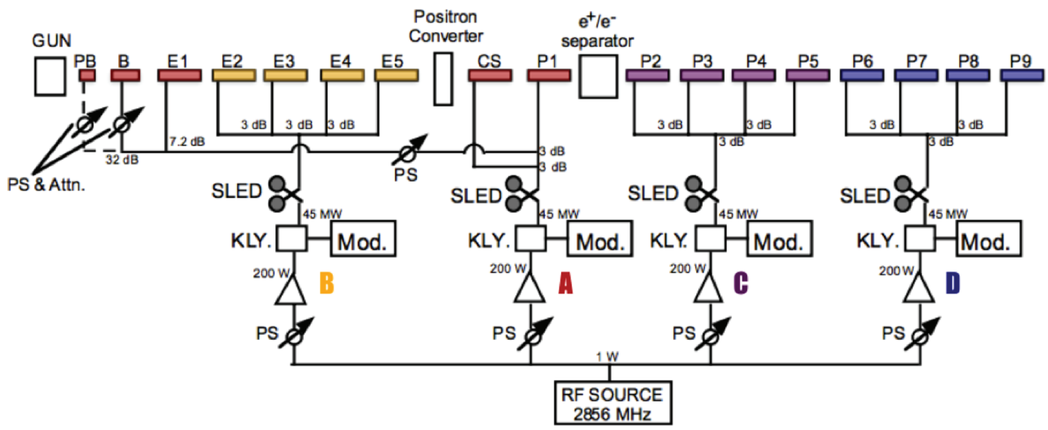

Figure 4.2: Schematic view of the DAΦNE LINAC RF power layout, showing – after the gun – the feeding scheme to the pre-buncher (PB) and buncher (B), followed by the five sections upstream of the positron converter (E1–E5), while downstream of the converter, after the capture section (CS), we have nine sections P1–P9 up to the LINAC output.

After having emitted by the thermo-ionic gun, electrons are accelerated by a pre-buncher, buncher and the E1 accelerating sections, which are immersed in a solenoidal field produced by 14 Helmholtz coils. Between E1 and E2 a quadrupole doublet allows matching the solenoidal focusing with the FODO transporting the beam to the positron converter, composed by two quadrupoles per each of the five accelerating sections (E1–E5). The beam is focussed into a 1 mm (RMS) spot on the converter target by a high gradient quadrupole triplet. Downstream the positron/electron separator, from section P2 to P9, a FODO, composed by 26 quadrupoles completes the focusing scheme.

The time duration of each LINAC pulse is dictated by the characteristics of the pulsing system, providing a rectangular waveform to the gun for the extraction of electrons emitted by the filament,

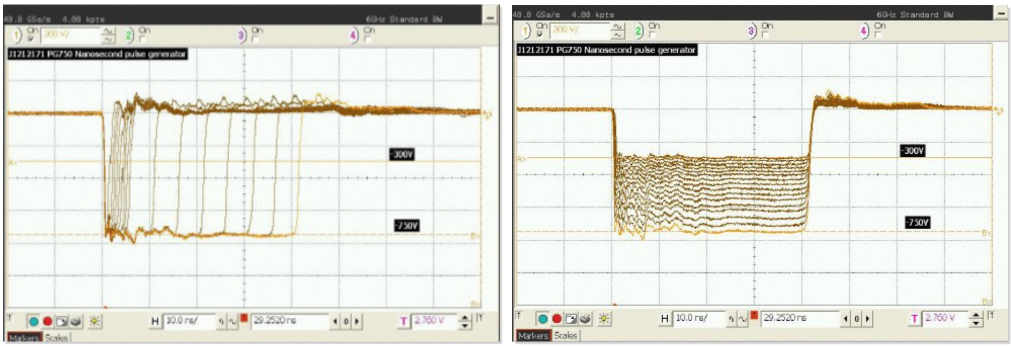

Figure 4.3: The rectangular waveform used to pulse the DAΦNE LINAC gun can be tuned changing its time width (left) and height (right), the horizontal scale is 10 ns/div, vertical scale is 200 V/div.

kept at a fixed bias voltage. In the present (end of 2015) configuration [28], it is capable of delivering pulses of adjustable total width in the range 1.5 to 40 ns, and height (300–750 V), as shown in Fig. 4.3. After acceleration, of course the beam will have a micro-bunched structure at the RF frequency of 2856 MHz. For the injection into the DAΦNE rings, the optimal pulse duration is 10 ns, thus this is the pulse width used during standard operation with the collider (a time profile of the electron pulse detected through the microwave emission with a horn antenna is shown in Fig. 4.4).

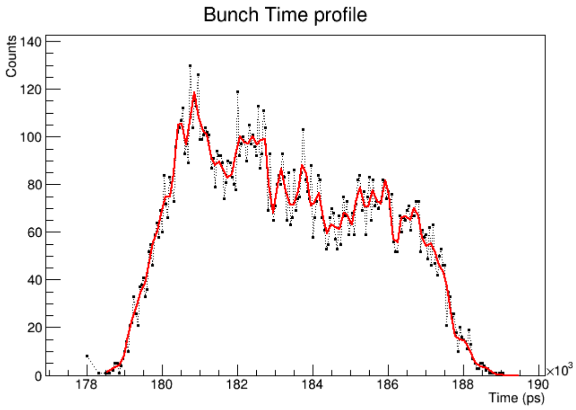

Figure 4.4: Time profile of the electron pulse detected through the microwave emission with a horn antenna (courtesy: AMY Collaboration) with the standard 10 ns setting of the LINAC gun.

In order to measure the spread of accelerated electrons and positrons at the output of the LINAC, the beam can be deviated to the spectrometer line (more details in the following) where it can be momentum-analysed by a 60° dipole magnet followed by a metallic strip detector. Typical momentum distributions are shown in Fig. 4.5, showing a RMS resolution of 0.5%, obtained at 500 MeV energy for pulse duration of 10 and 40 ns.

The relevant parameters of the LINAC are summarized in Tab. 4.1. As discussed in the following, there is the possibility of upgrading the gun pulser, in order to produce (and accelerate) electron bunches longer than 40 ns, most probably up to $\mathcal{O}(200)$ ns, with the advantage of diluting the same – or, even better, a larger – number of positrons in a longer pulse time.

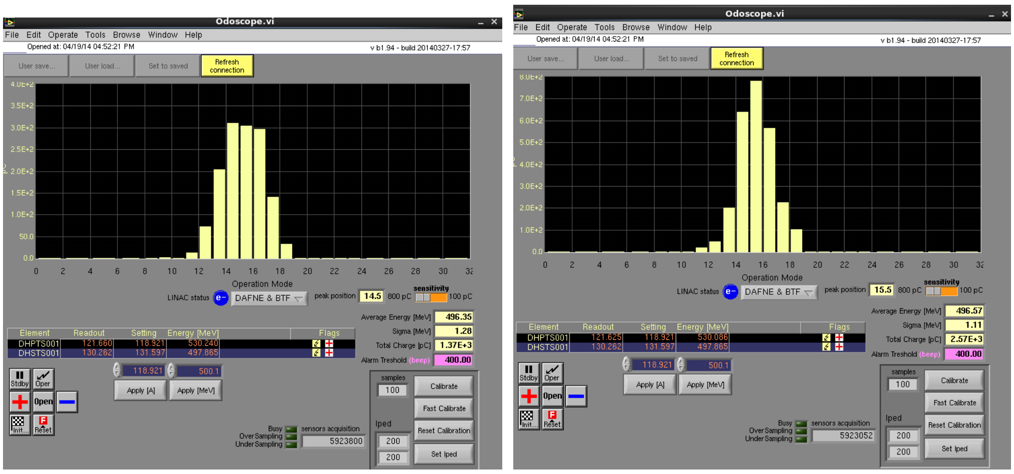

Figure 4.5: Typical momentum distribution of the electron beam at the output of the LINAC, measured on the spectrometer line at 500 MeV energy for 10 ns (left) and 40 ns (right) pulse width.

4.3 DAΦNE Beam-Test Facility

Taking into account the cross section (see Sec. 2.3), in order to have an acceptable occupancy in a inorganic crystal calorimeter (as discussed in section 5.4), the beam intensity for PADME will be in the range from $\mathcal{O}(10^3)$ to several 10^4 positrons per pulse.

The Frascati LINAC, acting as injector of a high-luminosity e^+e^- collider, indeed working in "factory mode", is optimized for producing and injecting in the accumulating rings high charge, 0.5/2 nC, short (10 ns), positron/electron pulses. Since the DAΦNE complex operates at the Φ meson resonance, $\sqrt{s} = 1020$ MeV, the injection system has to deliver 510 MeV electron and positron beams. These parameters correspond to $3.1/12.5 \cdot 10^9$ positrons/electrons in each 10 ns pulse, i.e. very far from the requirements of the PADME experiment.

We indeed plan to use the beam extracted from the LINAC on the separated transfer-line, dedicated to the Beam-Test Facility (BTF), with the possibility of attenuating the beam with a target, and reselecting the beam momentum with a dipole magnet and collimators system [29].

As shown in the scheme of Fig. 4.6, at the end of the LINAC the electron/positron beam can be diverted in three different lines using two pulsed magnets:

- At 0°, to the transfer-line to the damping ring (and from there, back to the pulsed magnet driving it to the transfer-line towards the main rings);
- at 3°, to the BTF beam-line;
- at 6°, to the spectrometer line: a 60° dipole plus a segmented (metallic strip) detector allows measuring the beam energy with a $< 0.5\%$ accuracy.

The DAΦNE timing system can realize different sequences in which a portion of the 50 pulses available in one second are injected to the damping ring, while the remaining ones are deflected on the BTF line. At least one pulse (two during the extraction from the damping ring and injection to the main rings, which is performed at 2 Hz) is sent to the spectrometer line, in order to have a 1 Hz measurement of the LINAC beam energy. A dedicated sequence for the standalone operation of the BTF is available, sending all available 49 pulses to the test-beam, and is used when not injecting

Parameter	**Value**			
Repetition rate	1 to 50 Hz			
Accelerating structure	15 × 3m, SLAC-type, CG, TW, $2/3\pi$			
RF frequency	2856 MHz			
RF power	4 × 45 MWp SLED-ed klystrons, TH2128-C			
Accelerating gradient	18 MV/m (24 MV/m)			
Parameter	**Design value**		**Operational value**	
Pulse length	10 ns		1.5–40 ns	
Gun current	8 A		8 A	
	e^- mode	e^+ mode	e^- mode	e^+ mode
Final energy	800 MeV	550 MeV	510 MeV	510 MeV
e^+ conversion energy		250 MeV		220 MeV
e^- spot at converter		1 mm		1 mm
e^- current at converter		5 A		5.2 A
Emittance (mm·mrad)	1	10	< 1.5	
RMS energy spread	0.5%	1%	0.5%	1%
Maximum current	> 150 mA	36 mA	500 mA	85 mA

Table 4.1: Main parameters (both design and operational values) of the DAΦNE LINAC in Frascati.

for DAΦNE operation. Since there is only one transfer line from the LINAC to the damping ring (also used for the reverse path from the damping ring to the main rings), it is necessary to reverse the polarity of all magnetic elements when switching from the injection of electrons to positrons, and viceversa. In this switching time the LINAC cannot deliver particles. This is a not negligible limitation of the duty-cycle of the BTF beam-line, when operating it together (in "parasitic mode") with the e^+e^- collider.

The range of parameters that can be achieved on the BTF beam-line using the attenuating target is much closer to the PADME requirements. It is worth noticing that actually the operation of the beam-test line can be performed in two different modes:

- in "dedicated" mode, i.e. without using the LINAC for the injection of electrons and positron for the operation of the DAΦNE e^+e^- collider. In this case the full flexibility of the beam production (the gun) and acceleration systems (the accelerating sections fed by the RF power produced by the klystron) can be used;
- in "parasitic" mode, i.e. delivering the BTF line only the LINAC pulses not used for the injection into the DAΦNE rings, which heavily limits the achievable beam parameters, due to the energy and timing requirements for injection in the DAΦNE rings summarized above.

Of course it is also possible to deliver to the BTF line the full LINAC beam, i.e. without intercepting the electrons/positrons with the target and using the selector magnet as a standard bending (at the nominal LINAC beam energy). Taking into account this possibility the resulting sets of parameters for the BTF beam are shown in the following Tab. 4.2 in the various operation modes: operating the LINAC in electron or positron mode, with or without interposing the BTF target, with or without the limitations induced by the simultaneous operation of the collider.

A detailed description on the production of the secondary BTF beam with the dedicated target is given in the next section.

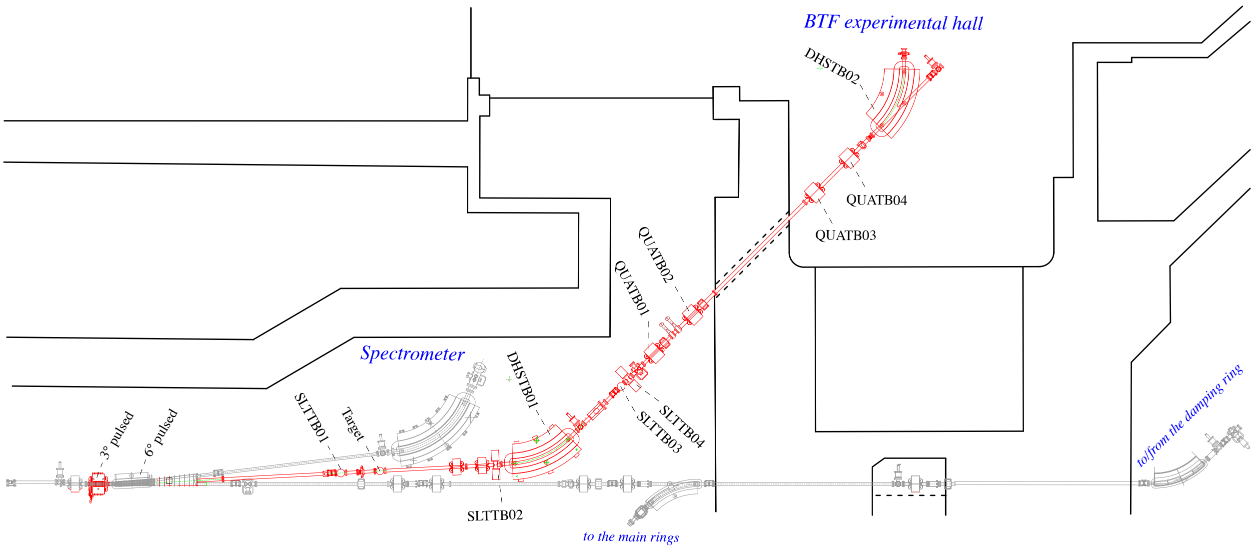

Figure 4.6: Layout of the transfer-line from the LINAC to the damping ring and main rings, and of the BTF line, with all the beam attenuation and focussing elements.

4.4 Secondary beam production in the BTF line

The lowest beam current that can be accelerated and transported from the DAΦNE LINAC is of the order of 1 mA, also due to the limited sensitivity of beam diagnostics (position and intensity, as well as energy and timing). This sets a lower limit for the primary beam of the order of 10^7 particles/pulse. Of course lower intensities can be achieved by scrapering the beam, but with a reduction factor strongly depending on the quality of the beam (e.g. the transverse shape). The most convenient way of producing a very low intensity beam, down to the so-called "single particle" regime, when we deal with a Poissonian distribution of electrons (or positrons) is to intercept the beam with a target, producing a secondary beam. The interaction of the electron beam with a target will produce a broad distribution both in energy and angle, so that if the resulting particles are momentum-selected and collimated (with a given acceptance), a much less intense beam is produced. As in a spectrometer, a well defined energy can be selected by means of a constant magnetic field, introducing a spatial dispersion of particles of different momentum, followed by a collimator, accepting only a given range of momentum.

In Fig. 4.6 the main elements of the BTF attenuation, energy selection and transport of the beam are shown: after being deflected by 3°, a primary LINAC pulse is vertically collimated by the SLTTB01 tungsten slits, in order to tune the primary intensity, and strikes on a extractable Copper target.

The energy selection is performed by the DHSTB01 42° bending magnet, with two horizontal collimators upstream (SLTTB02) and downstream (SLTTB04) of the dipole for momentum definition. After energy selection, a second vertical collimator (SLTTB03) allows a fine intensity tuning. The following elements are essentially a couple of quadrupole doublets (QUATB01–02 and QUATB03–04) with horizontal and vertical correctors, which are used for the transport and focussing of the BTF beam. Finally, in the BTF experimental hall the beam is further deviated by 45° by the DHSTB02 bending magnet, in order to be directed along the main axis of the room.

This technique has several advantages with respect to simply removing particles from the beam

Parameter	**Values**			
Maximum flux	$3.125 \cdot 10^{10}$ s^{-1}			
Spot size (hor.)	0.7–55 mm			
Spot size (vert.)	0.7–25 mm			
Divergence	1–2 mrad			
Parameter	**Parasitic mode**		**Dedicated mode**	
Pulse duration	10 ns		1.5–40 ns	
Repetition rate	Variable (depending on DAΦNE injection status)		1–49 s^{-1} (selectable)	
	With target	**Without target**	**With target**	**Without target**
Particle type (e^+ or e^-)	selectable by users	alternating according to DAΦNE status	selectable by users	selectable by users
e^- Energy (MeV) e^+ Energy (MeV)	25–500 25–500	510 510	25–700 25–500	250–730 250–530
Energy spread	1% at 500 MeV	0.5%	0.5%	0.5%
Intensity	1–10^5	10^7–$1.5 \cdot 10^{10}$	1–10^5	10^3–$3 \cdot 10^{10}$

Table 4.2: Beam parameters achievable in all possible operation modes at the end of the BTF line.

with scapers:

- starting from a monochromatic beam of energy E_0, it allows to produce a beam of any energy in the (almost) full range from 0 to E_0;
- the momentum resolution of the secondary beam is determined by the collimators, thus allowing to get again a narrow band beam;
- the reduction factor depends essentially on the target thickness and from the momentum acceptance;
- both electrons and positrons are produced (of course with different yields) starting from a electron beam;

In the case of the BTF, the secondary beam is produced by means of a step-shaped Copper target, allowing to select three different depths: 1.7, 2 or 2.3 radiation lenghts. The resulting energy distribution, as a function of the angular cut, can be estimated quite accurately with a Monte Carlo simulation: as shown in Fig. 4.7, by selecting forward particles the electron energy distribution gets much more flat, thus allowing to get a reduction factor depending less sharply from the chosen energy.

One of the most important parameters of the positron beam for PADME is the maximum achievable energy, while keeping a good beam quality and allowing to choose an intensity in the range of few 10^3 up to 10^4 particles/pulse. Looking at the correlation between the energy and the angle of the secondary electrons and positrons (shown in Fig. 4.8 for the minimum thickness of the BTF target, corresponding to $1.7X_0$), it is clear that the highest energy secondaries are emitted in the very forward direction, while electrons and positrons emerging from the target at larger angles have a lower maximum energy. Since this can be easily interpreted as the correlation with the number of interactions with target atoms of both deviation from the incoming direction (due to the scattering on nuclei) and energy loss (due to interaction with the atomic electrons), we can

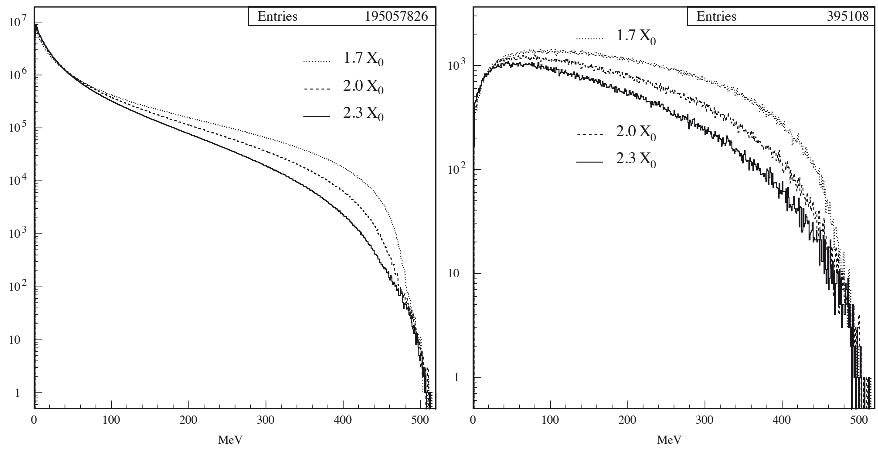

Figure 4.7: Number of electrons as a function of their energy, emerging from the BTF Copper target, with no angular cut (left) and by requiring $\theta < 4$ mrad (starting from 10^8 primary electrons).

try to optimize the production of positrons of highest possible energy as a function of the target thickness.

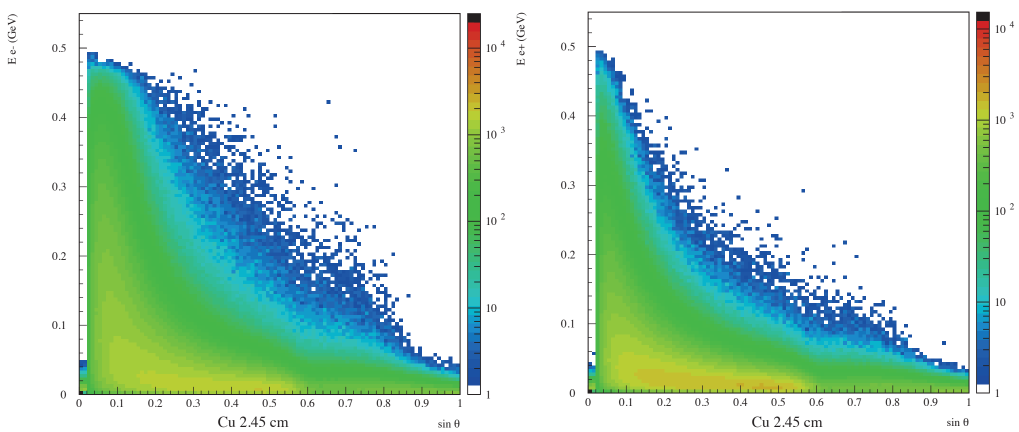

Figure 4.8: Monte Carlo distribution of the momentum (in GeV/c) as a function of the angle (in rad) for 10^8 510 MeV/c electrons impinging on a $1.7X_0$ Copper target (2.45 cm) for secondary electrons (left) and positrons (right).

Since the incoming electron has to produce at least one (on-shell or off-shell) photon that then has to undergo a pair production interacting with the field of a nucleus, one can expect that having a too thin target will decrease the overall (integrated over the energy) positron yield, while for a very thick one, the produced positrons will undergo additional interactions and thus significantly losing energy (by irradiating photons, ionization, etc.); one can expect the optimum to be around $\approx 1X_0$. In addition, due to the collimation for good momentum definition – which also is a requirement for the PADME experiment – only secondaries within a quite tight angular cut will be useful. Varying the thickness of the Copper target in the GEANT-based Monte Carlo of the BTF, we obtain the distribution of positron angle as a function of the momentum shown Fig. 4.9.

Considering an acceptance of the momentum selection system of 1%, we can then estimate the

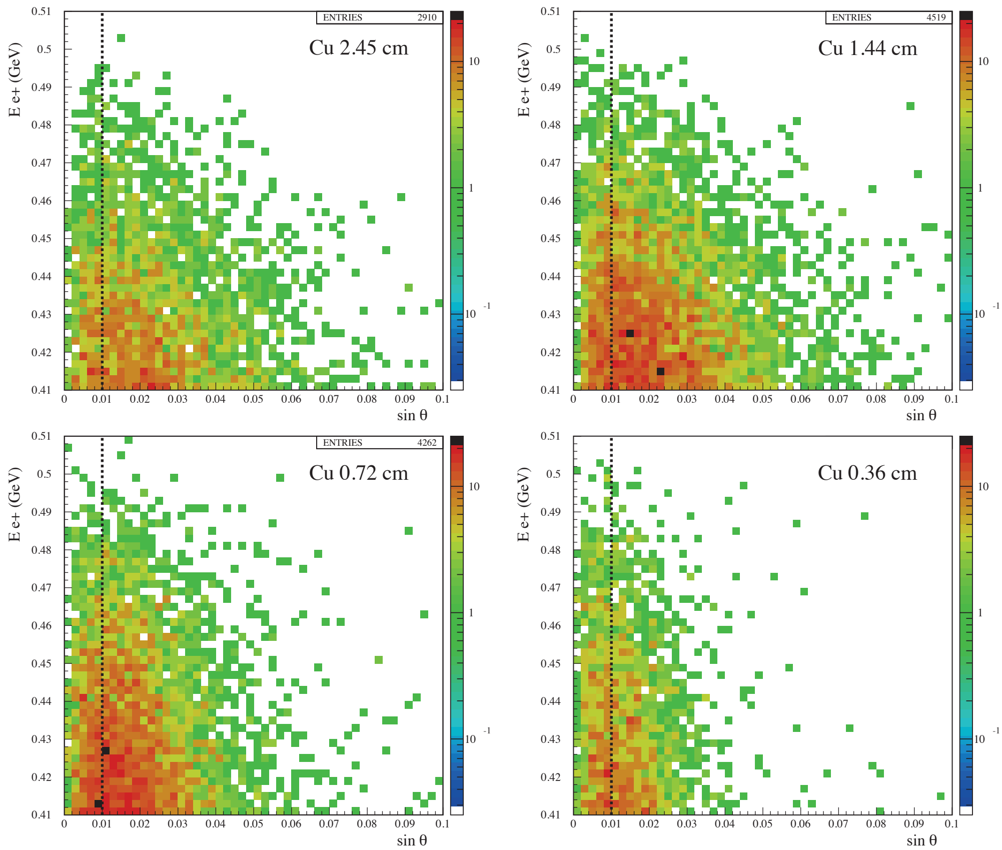

Figure 4.9: Monte Carlo distribution of the positron momentum (in GeV/c) as a function of the angle (in rad) for 10^7 510 MeV/c electrons impinging on a Copper target of decreasing thickness (from left to right, from top to bottom).

number of surviving positrons as a function of the required energy: as shown in Fig. 4.10, the yield will decrease asking for higher energy positrons, but we can see that the optimum will be around or just below one radiation length, in any case well below the minimum thickness of the present BTF target. The simulation has been performed with $E_0 = 510$ MeV primary electrons, but it can be safely scaled to different energies, just expressing the energy of the secondaries in per cent of E_0.

Considering a primary beam current of the order of 1 nC/10 ns, which is routinely used in the standard DAΦNE collder operation, and an overall efficiency of the transport and collimation of the order of 10%, we can produce a 10^4 positron beam by selecting an energy in a range around 90% of the primary energy.

This means that the LINAC can be operated in electron mode, i.e. without the positron converter, thus increasing the maximum energy by 220–250 MeV, since in this case also the first five accelerating sections are used. Starting from 1 nC/10 ns pulses of 730 MeV electrons, we can then produce at least 10^4 positrons selecting an energy $E \approx 650$ MeV (in a 1% band) on a optimized BTF target (with variable thickness adjustable in some range around 0.5–1.0X_0). Would be the beam-line and collimation efficiency significantly lower, we can increase the gun pulse height thus recovering the required beam intensity (at least an order of magnitude of margin). Finally, we do not expect any significant difference running with 40 ns long pulses.

The new optimized target can be realized by machining a block of Oxygen-free Copper block,

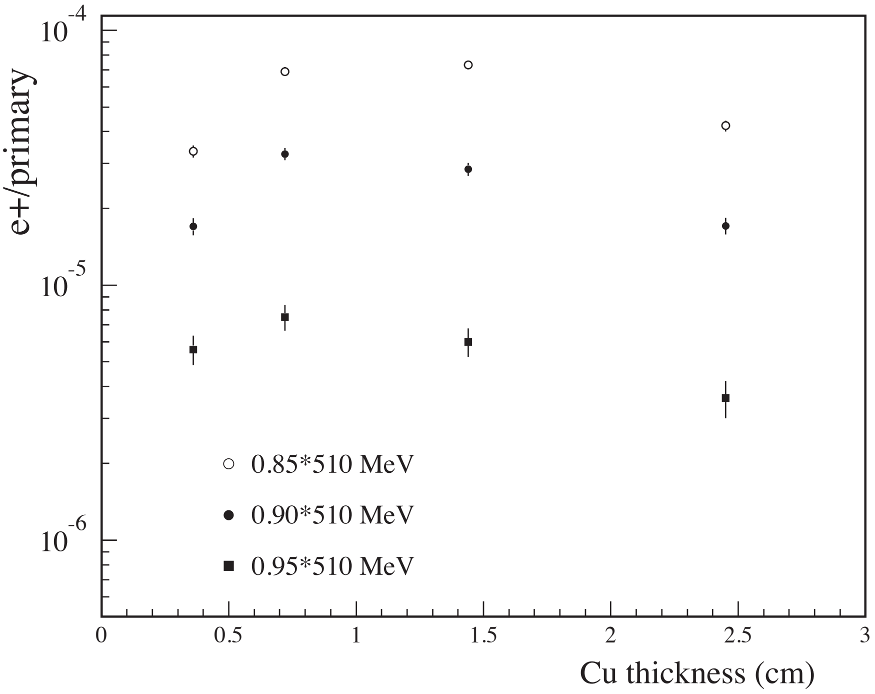

Figure 4.10: Monte Carlo estimate of the positron yield as a function of the thickness of the Copper target, for three values of the selected energy, corresponding to 85%, 90% and 95% of the primary electron energy (510 MeV).

of approximate transverse dimensions 70×160 mm^2 (in order to fit the present target moving system in vacuum), with three or four steps, e.g. 0.5, 0.75, 1.0 radiation lengths, with the option of $1.7X_0$ in order to reproduce the operation with the present target. Taking into account the Copper present cost of 2400 USD/lb and the density of 8.9 g/cm^3, we can estimate a cost for a block of ≈ 2.7 KG of the order of 15 kEur.

4.5 BTF beam spot measurement and optimization

In order to provide fast transverse beam imaging to the facility users, a MEDIPIX silicon pixel detector with FITPIX electronics is available in the BTF standard diagnostics. The sensors have a square pixel of 55 μm side in a 256×256 pixels (overall side length 1.4 mm) layout for a square sensitive area of about 2 cm^2 and 300 μm thickness.

The beam spot is of course dominated by the optics of the transfer line, after electrons (or positrons) have been momentum-selected by the BTF first dipole (DHSTB01). The optimal transport has been calculated for 510 MeV and then checked against data, and has been rescaled for different (lower) selected energies, assuming that the beam is perfectly centered all along the magnetic line. This is not the case, due to the misalignment of some elements, but this can be easily compensated by fine adjustments of the line.

In most of the cases, the BTF beam is used in "single particle" mode, which in general means that the collimators, both the x–y couple downstream of the energy selection, and the x–y couple upstream of DHSTB01 are kept at an opening gap of a few mm. By optimizing the collimators a standard deviation of the order 1 mm can be obtained in both coordinates in the transverse plane.

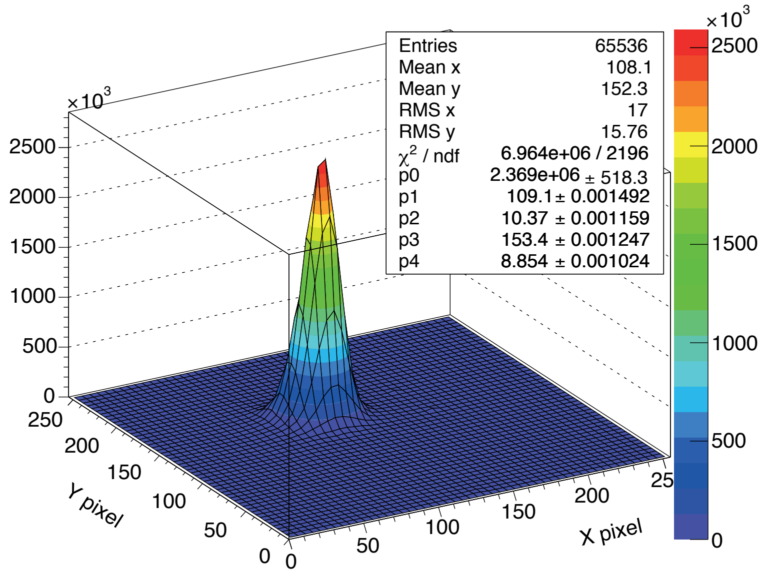

Figure 4.11: Transverse beam spot optimized for “single electron” at 450 MeV, by collimating along the horizontal and vertical axis and optimizing the magnetic line, measured with the FitPIX detector, corresponding to $\sigma_x = 0.57$ mm, $\sigma_y = 0.49$ mm ($p2$ and $p4$ in the fit are in 55μm pixel units).

A smaller beam spot can be obtained by a careful fine-tuning of the magnetic line, adjusting all the quadrupoles (e.g. correcting for the bending component due to bad alignment with respect to the magnetic center). In this configuration a standard deviation of the order of 500μm in both coordinate can be achieved, as shown in Fig. 4.11, largely dominated by the effect of multiple scattering of the beam on the exit window of the vacuum beam pipe (500 μm thick Beryllium) and the few tens of cm of air before the FITPIX detector.

The divergence of the beam in this configuration is of the order of 1 mrad, and has been estimated by measuring the beam spot size at different distances from the beam exit, taking into account the effect of multiple scattering in air.

In order to increase the beam intensity up to the 10^3 particles/pulse range, the main handle is increasing the opening of the horizontal collimator (SLTTB02) upstream of the dipole selecting the beam momentum (DHSTB01), which is the first element after the BTF target (1 m downstream of the target), with the main purpose of limiting the divergence of the secondaries entering the DHSTB01 bending magnetic field. Electrons (or positrons, when selecting positive particles) entering the magnet with an angle will indeed follow a trajectory different from the central one, thus increasing the momentum spread after the downstream collimator (see [31]). This has an impact on the BTF beam spot since the beam-line normally used is the one with an additional 45° bending (DHSTB02, driving the beam along the longer axis of the experimental hall) which of course introduces a significant dispersion (in the bending plane).

The effect of opening the SLTTB02 slits by ≈ 5 mm in order to reach 10^3 electrons at 450 MeV, can be easily seen in Fig. 4.12: while the vertical size is not affected, the horizontal dimension of the beam spot increases up to several mm. In Fig. 4.13 the effect of fully opening the SLTTB02 collimator, reaching the maximum intensity in this configuration of $2.3 \cdot 10^3$ particles/bunch, can be also seen.

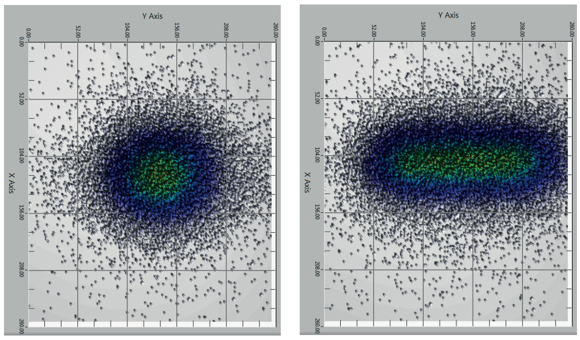

Figure 4.12: Transverse beam spot at 450 MeV energy, with closed SLTTB02 collimator (250 μm opening) yielding a few tens particles/pulse (left) and by opening the slits up to 10^3 particles/pulse (right).

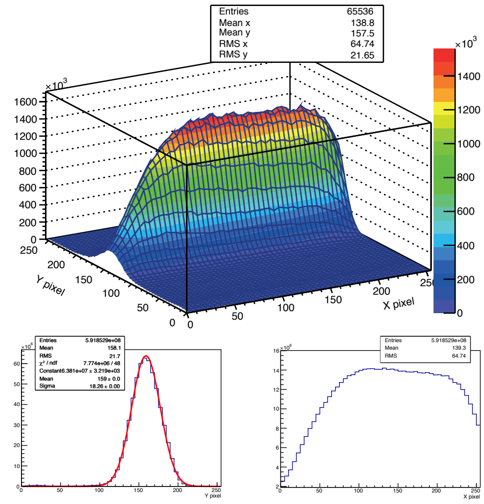

Figure 4.13: Transverse beam spot at 450 MeV energy with the slits of collimator SLTTB02 open, in order to reach $2.3 \cdot 10^3$ particles/pulse: 2D surface plot (top) and projections on the x and y axes (bottom).

However, there are at least two factors that will contribute in recovering a millimetric size also in the horizontal coordinate at the intensity required by PADME:

- Running the LINAC in dedicated mode allows increasing the beam charge, so that a larger fraction of the beam can be lost due to collimation with the SLTTB02 slits, thus reducing the effect of dispersion described above;

- the PADME target will be integrated in the BTF vacuum system, so that the contribution of multiple scattering on the Beryllium exit window (and at least 20 cm of air, for the closer configuration of the FITPIX diagnostics detector) will be absent, thus giving a smaller divergence beam and a smaller spot at the target;

Of course, even though the expected beam parameters have been estimated on the basis of routine measurements of the BTF beam, then adding pretty conservative and reasonable assumptions, a commissioning of the beam-line and a optimization phase should be foreseen, as soon as the improvements foreseen for PADME, e.g. the thinner BTF target, will be built and installed.

4.6 BTF vacuum and installation

The BTF vacuum pipe is normally connected to the LINAC main vacuum, of the order of 10^{-9} mbar. A fast gate valve allows sectioning the BTF from the main LINAC line in case of interlock. The BTF is also equipped with a turbo pumping system in order to achieve a secondary vacuum of 10^{-5}–10^{-6} mbar, when disconnected from the LINAC main line. BTF exit flange are also equipped for connection to a secondary vacuum, in order to connect users vacuum installation and safely pump them.

Probably a higher pressure is tolerable/needed for the large PADME chamber. In our case integration of diamond target will be needed, including the routing out of the vacuum flange of the analog signals (see Sec. 5.2).

Two possible layouts of PADME in the BTF experimental hall are shown in Fig. 4.14; the moveable walls (1 m thick) made of superimposed concrete blocks (for shielding the radiation below the required level outside the experimental hall) are also shown. At the end of July 2015 all of the shielding blocks have been dismounted and removed from the BTF hall; in September they have been remounted in a rearranged configuration, in order to hold on top a new shielding "roof", made of concrete bins (5.5 m long, 50 cm high). The maximum available height in the BTF hall is thus reduced, in the "bunker" area, to 3 m.

4.7 BTF improvements and upgrade

As discussed in the previous sections, there are three main parameters – relevant for the PADME experiment – of the positron beam produced by striking high-energy electrons from the DAΦNE LINAC on the dedicate target, momentum-selected and focussed by the BTF line, and delivered to the test-beam experimental hall:

- the maximum energy at which the PADME intensity (a few 10^3 positrons for a 40 ns long beam pulse) can be achieved;
- the beam pulse duration (presently limited to 40 ns by the gun pulsing system);
- the beam spot size and the beam divergence.

These parameters are correlated: the size and divergence of positron beam depends on the collimation upstream the momentum-selecting dipole, so that closing the slits for getting a beam with lower momentum dispersion and a smaller spot, reduces the intensity or – keeping the intensity fixed – the maximum energy that can be achieved. As already described, some optimization can be done on the beam optics and collimation, but we are also considering dedicated modifications and upgrades of the present beam-line.

We have already described in section 4.4 a possible new target for optimizing the production of high-energy positrons, but there is a complete program of upgrades of the beam-test facility [64] that can be very profitable for PADME, in particular:

- in the shorter term, the extension of beam pulse of the LINAC from 40 ns to ≈200/250 ns;
- in the long term, the energy upgrade of the LINAC, in order to reach 1–1.2 GeV range.

The extension of the beam pulse is grounded on the running performed at the SLAC LINAC (very similar to the DAΦNE one) in the '90s, for performing high-statistics deep inelastic scattering experiments with polarized targets. The main issue is the increasing energy spread, due to beam loading, as the pulse width is increased.

For the experiment E-154 (E-155), 48.8 (48.8) GeV electrons were routinely accelerated in 240 (400) ns pulses with a 0.5% energy spread, while in the test phase, up to 520 ns pulses of 10^{11} electrons were accelerated, as described in [33], by using additional phase inversions in the SLED driving pulse from the klystrons in order to keep a small energy spread even in presence of beam loading (see Fig. 4.15).

The BTF and LINAC teams are now planning to extend the capability of the gun pulsing system from 40 ns up to 1 μs (estimated cost of the order of 80 KEuro), in order to extend the maximum pulse length, first without transient beam loading compensation – probably up to 150–200 ns – and then, by adding phase inversions in the RF system, hopefully up to $\sim$ 500 ns.

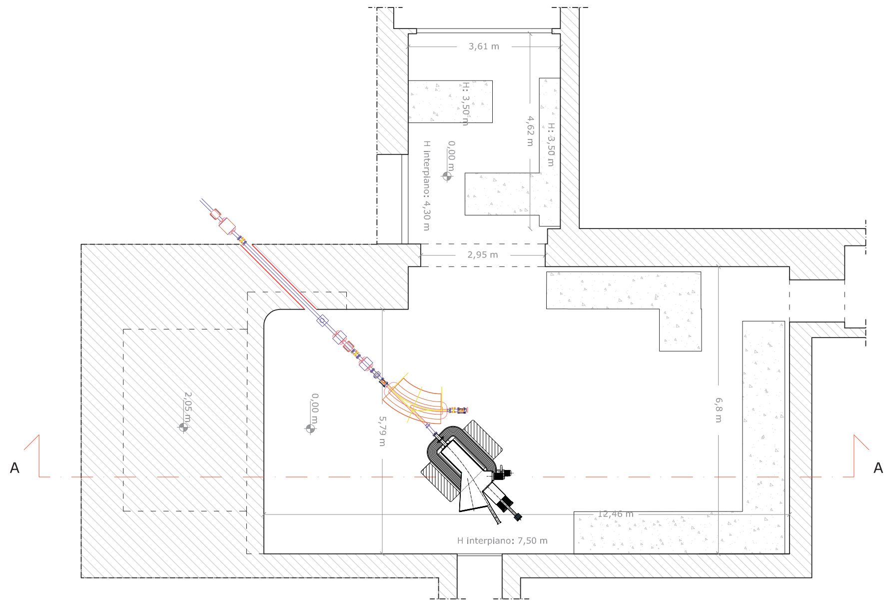

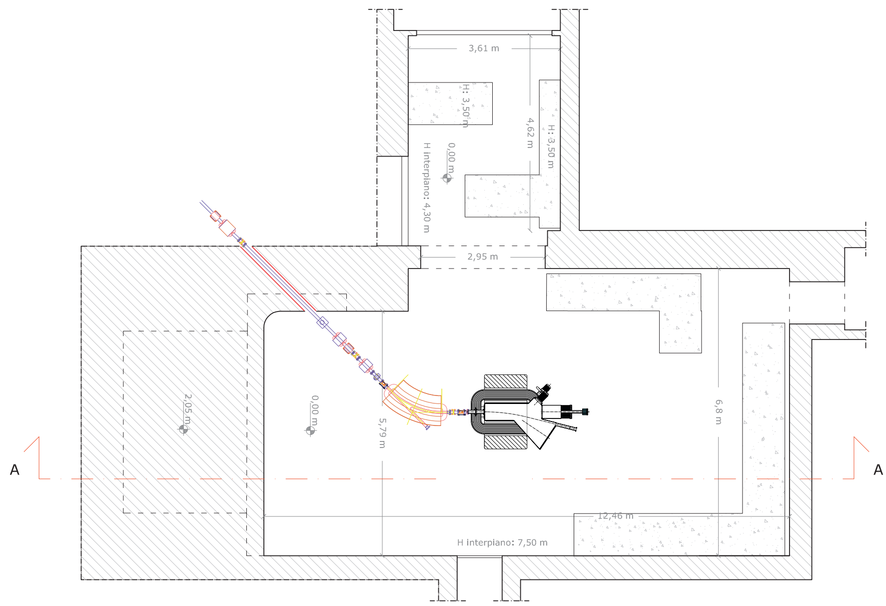

Figure 4.14: Two possible installations of the PADME setup in the BTF experimental hall: along the straight BTF line (top) or at the beam-exit after the 45° bending dipole (bottom). The second option has a major impact on the possible alternative use of the facility, while the first does not allow the installation of a larger calorimeter at 400 cm from the target. The shielding moveable walls made of concrete blocks inside the BTF hall are also shown

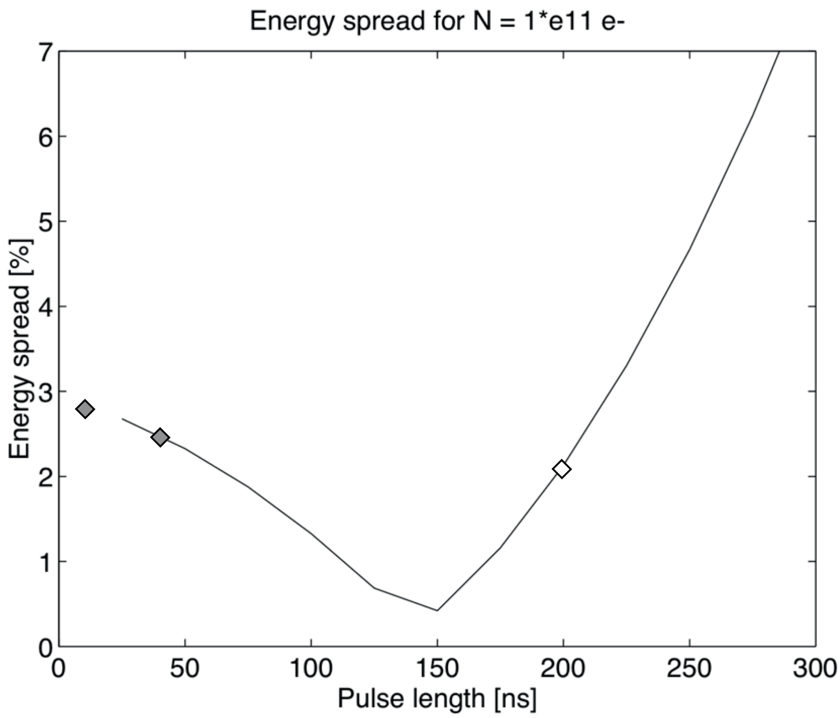

Figure 4.15: Energy spread as a function of the accelerated pulse length in the SLAC LINAC (adapted from [33]).

Chapter 5

The PADME experiment

5.1 General layout

PADME will be a small scale positron on fixed target experiment operating in the DAΦNE BTF hall as described in the previous chapter. The experiment will make use of 49 (out of the 50 available) bunches/s, each with $\sim 5 \cdot 10^3$ positrons to collect a sample of 10^{13} positrons on target in a couple of years. The experiment will search for the process $e^+e^- \to \gamma +$ *nothing* due to the dark photon decaying in the "invisible" channel, i.e. particles remaining undetected. The only measured quantities will be the positron beam four-momentum, provided by the beam line, and the recoil photon four-momentum, measured by a inorganic crystal homogeneous calorimeter.

To suppress backgrounds, veto detectors will help in identifing final states with associated charged tracks or extra photons. A magnet will deflect charged tracks into veto detectors acceptance avoiding them to hit the calorimeter, at the same time providing a measurement of the momentum of those particles.

The acceptance of annihilation events is determined by the angular coverage of the calorimeter (see Fig. 5.22), which is determined basically by the distance of the calorimeter from the production target and by its lateral dimensions. The target–calorimeter distance D is also the parameter determining the angular resolution for photons, together with the calorimeter granularity a (basically $1/D \cdot a/\sqrt{12}$). The angular resolution for photons is the dominant contribution to the missing mass resolution, that, as described in Chapter 9, drives the bin size for the dark photon mass peak search: a better resolution allows choosing a smaller mass interval, thus reducing the amount of background events per bin, and finally improving the sensitivity.

Of course, the path of photons to the calorimeter, as well of the positron beam, has to be in vacuum, in order to minimize interactions not coming from the target. A vacuum vessel has then to encompass the calorimeter acceptance and the trajectories of positrons from the beam, that in case can loose energy by irradiating Bremsstrahlung photons on the target. The gap of the sweeping/analysing magnet should be finally large enough not to intercept photons inside the calorimeter acceptance.

The basic configuration of the experiment is sketched in Fig. 5.1: in this very schematic drawing the concept of the layout is shown. Of course many details have to be optimized carefully with the help of Monte Carlo simulations (see Chapter 8), also in terms of cost and complexity. For instance, among the main elements driving the final choice of the layout there will be the total number of crystals in the calorimeter and their dimensions, due to the impact on the total cost of the crystals themselves and of the readout electronics, which will fix the calorimeter overall size.

In the following sections, the general layout will be better defined, as the parameters of the

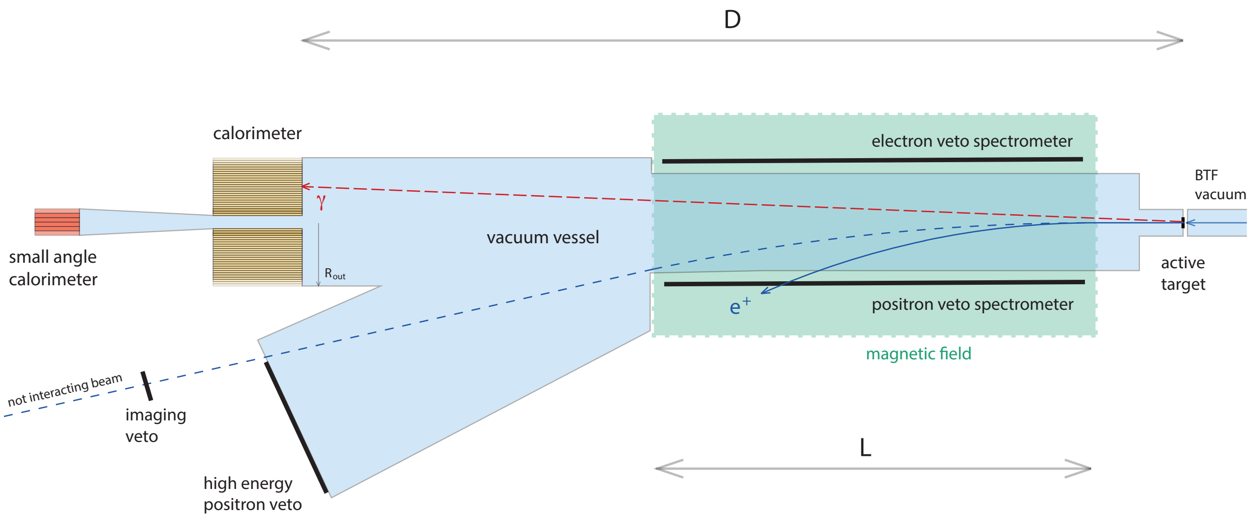

Figure 5.1: Schematic layout of PADME experiment, showing all the baseline elements.

main detectors are optimized, also taking into account the constraints coming from the availability of some elements, from the size of the experimental hall, or from the number of readout channels. For example, as stated before, the size of the magnet gap, together with its maximum field and length (see Sec. 5.3), gives some important constraints on the angular acceptance of the calorimeter downstream. The main elements that will be described in the remainder of this chapter are the following:

- Active diamond target
- Analysing magnet
- Vacuum system
- Electron and positron veto detectors
- Calorimeter
- Small angle calorimenter

The listed detectors should of course be powered, readout by the proper front-end electonics (FEE), and should transmit their data to the data acquisition system (DAQ), whenever requested by the trigger system (Chapter 6). The TDAQ should of course also take care of recording the acquired data. The following steps of permanently storing, reconstructing, filtering and analysing the data will be performed by the Computing system (described in Chapter 7).

5.2 Active Diamond Target

5.2.1 Introduction

The active target of the PADME experiment will act at the same time as the low-Z, thin target for the production of dark photons (while keeping the Bremsstrahlung production at an acceptable level), and as monitor of both the spot posizion and size, and of the intensity of the positron beam.

Taking into account the cross sections on Carbon, we aim at a thickness in the range 50–100 μm. The active surface should match the dimension of the beam spot, taking into account the long experience with 1.5×1.5 cm^2 Silicon pixel detector (FITPIX) at the BTF, a similar area seems to be adequate, even though a 2×2 cm^2 would ensure better coverage also in case of beam long-term fluctuations, without the need of adjusting the beam optics.

The choosen baseline material for the active target is an electronic grade polycrystalline diamond film. Polycrystalline diamond is produced by Chemical Vapour Deposition (CVD) from energized H_2(98%)+CH_4(2%) gas mixtures.

Diamond is a semiconductor with outstanding material properties such as high radiation hardness, high free carrier mobilities, very low leakage current, and very high thermal conductivity. High quality CVD diamond can be used as radiation detector which is in many ways much simpler than Silicon radiation detectors. Indeed:

- diamond is not doped;
- metallic electrodes are simply placed on device surface;
- the signal is collected by a charge sensitive amplifier;
- no leakage current compensation is needed;
- no cooling is required.

These detectors are successfully employed in several scientific and technical fields where the signal is not a concern but radiation tolerance and fast response are mandatory. These applications are mainly heavy ions detection (see GSI experiments at Darmstadt in Germany) and beam or X-ray monitoring (intense synchrotron light, FEL, and inertial fusion sources) [34].

Nevertheless, in the last years large size and free-standing polycrystalline diamond are produced with high quality and good reproducibility, making this material attractive for very demanding applications such as tracking detectors at LHC upgrades and bi-dimensional dosimeters for Intensity Modulated Radiation Therapy (IMRT).

Diamond quality is strongly related to the charge collection distance $\lambda = \lambda_e + \lambda_h$, which is the distance electron-hole pair drift apart, due to the electric field E, before trapping or recombination occurs. For minimum ionizing particle (mip) counting mode, the induced electric pulse (q_{ind}) is given by:

$$q_{ind} = 36\frac{e^-}{\mu m}\lambda[1 - \frac{\lambda}{d}(1 - e^{-\frac{d}{\lambda}})]$$

where d is the distance between biasing electrodes. Since 1995, the CERN RD42 collaboration reached in about 20 years about 9,000 electrons of collected charge signal across a "as grown" 1 mm thick wafer, lapped from the nucleation side down to 500 μm and polished on both sides, corresponding to about 250 μm of CCD.

Single channel devices, readout by a quite traditional electronic chain, are used when position information is not required, such as in monitoring and dosimetry. Electrodes patterning in micro-strips and pixels by lithography are necessary in tracking and vertexing reconstruction, such as

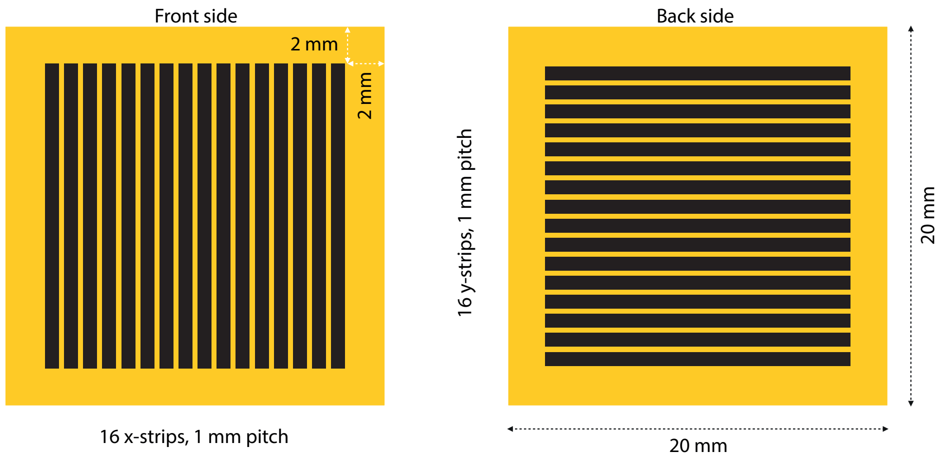

Figure 5.2: Baseline x–y strip segmentation for the diamond active target for the PADME experiment.

in high energy physics. In addition, advanced interconnection techniques between sensors and front-end electronics are required to realize multi-channel hybrid devices.

For the PADME active target we propose to use detector grade polycrystalline sensor, segmented on both sides with orthogonal strips (see Fig. 5.2). The choice of strip geometry with respect to the pixel geometry is related to the unacceptable material introduced in the active area for the latter.

A consequence of strip geometry is that the active target can reconstruct only single coordinates in the transverse plane, namely the x and y profiles separately and not a two dimensional x–y profile, which is possible only with a pixel geometry or by using a out-of-beam imaging device (for example a Cherenkov imaging device). This limitation should not be a problem for our application because the beam shape should be fairly Gaussian, and the main aim of the device is the monitoring of the position and width of the spot (as well as its intensity).

With respect to diamond detector "state of the art" the most challenging aspect of an active diamond target for the PADME experiment is related to the small thickness (50–100 μm) for a quite large area (up to 2×2 cm^2) which makes the sensor fragile. Instead, the quite low signal (CCD $<$ thickness/2) for a mip is likely not a problem for PADME because the bunch of electrons is composed of few thousands of positrons. Nevertheless, response uniformity, gain fluctuations and linearity must be verified.

5.2.2 Diamond procurement

In developing diamond detectors for a real experiment the procurement of the high quality diamond sensors is an important issue. Starting from May 2014 we have acquired large size, thin diamond samples from Applied Diamond Inc. (Delaware, USA), listed in Tab. 5.1, where it can be seen that four of these samples can be used to realize the final active target for PADME and many small diamond devices for testing and optimization. One of the large samples broke in few pieces after gel-pack opening, reminding us that the active target handling and gluing are issues that must be faced carefully.

Applied Diamond Inc. has been working recently to make thin film detector grade diamond material and has had some success. This supplier grows the diamond from a silicon substrate and than remove the silicon by etching from the diamond nucleation layer to obtained a free standing sample (see Fig. 5.3).

#	Size	Cost	Delivery time
2	50 μm $\times$2 cm $\times$2 cm	2000 \$ each	3 months (first batch)
2	50 μm $\times$2 cm $\times$2 cm	2000 \$ each	8 months (after 2 failed batches)
1	100 μm $\times$2 cm $\times$2 cm	2150 \$ each	1 year (after 3 failed batches)
10	50 μm $\times$5 mm $\times$5 mm	175 \$ each	1 week (from failed batch)

Table 5.1: Thin detector grade diamond samples acquired from Applied Diamond Inc. (Delaware, USA).

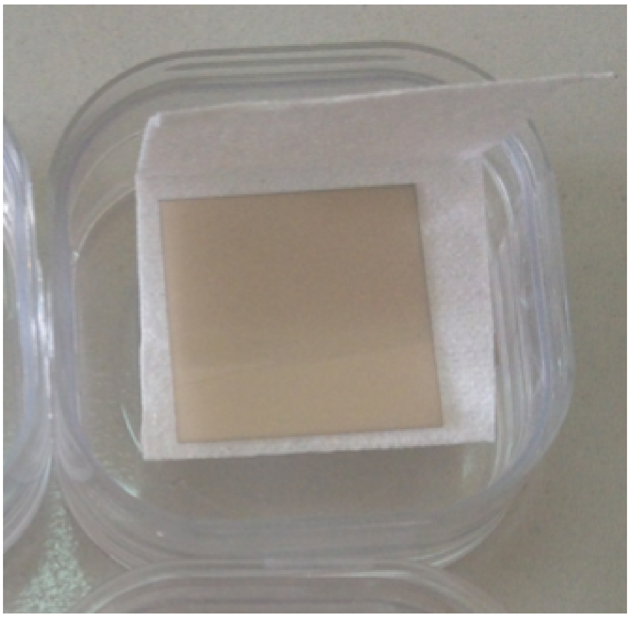

Figure 5.3: One of the polycrystalline diamond sensors provided by Applied Diamond Inc. (Delaware, USA) of size 2×2 cm^2 and thickness 50 μm.

5.2.3 Diamond sensor fabrication

To have an active target is necessary to fabricate on the diamond surface, on both sides, Ohmic electrodes to be readout by an adequate front-end electronics and digitized. In our baseline design we assume 16 strips of 1 mm pitch on both sides with orthogonal orientation, x and y and 2 mm dead space on each boundary.

Traditionally, the Ohmic electrodes on diamond involve three different metals. The first, closest to the diamond, is a Carbide-former such as Titanium, Tungsten or Chromium. These metals make a chemical bond with the diamond to insure adhesion of the metalization. A diffusion-barrier is then applied, typically Palladium or Platinum. Finally the layer required for the process is added. Gold or silver are usually used to prepare the diamond for brazing, eutectic bonding or other attachment techniques. Applied Diamond Inc. has also metalization capability on very thin diamond, depositing Chromium and Gold by evaporation as metal layers (this add to the cost quoted in Tab. 5.1 about 2000 $).

For PADME we intend to purse a full Carbon device, in order to avoid any high-Z material that would introduce and enhancement in the production of Bremsstrahlung with respect to annihilation events. Taking account that the metal layer thickness is of the order of 100 nm and the atomic number of Gold is $Z = 79$, we can have an effective thickness as low as 7.9 μm, to be compared to the target thickness of 50–100 μm.

The full carbon active target could be realized in the L3 laboratory at the Università del Salento, where in collaboration with INFN "Commissione V" (DIAPIX experiment 2011–2013), a system for the realization of nano-graphitic electric contacts on a detector-grade diamond material is available, using a 193 nm UV ArF excimer laser, which is absorbed by diamond ([38], [39]).

The laser emits 20 ns long pulses with an energy of about 160 mJ/pulse at 10 Hz repetition rate, and with a transverse size of about 20×10 mm^2. The laser beam is projected by a optical system on the diamond sample placed on a computer assisted x–y holder with micrometric spatial resolution. After focusing the laser fluence on the sample surface is about 5 J/cm^2, and a nano-graphitic layer is created, which turns out to be mechanically stable and electrically conductive. The laser intensity has been tuned to make the transition diamond-graphite thermodynamically favorite, without ablating the material.

Measurements showed that the pad detector with graphitized contacts is capable to detect ionizing radiation in counting mode. No evidence of polarization (decrease of signal with time) or inefficiency (low counting rate) were seen and speed, noise, stability and radiation damage properties are comparable to other detector with Ohmic contact [40].

In 2015 we improved the optical setup in order to be able to have reproducible and automatic sensor production capability (see Fig. 5.4). With this new setup we can easily fabricate strips of 20 μm and 110 μm width, as shown in Fig. 5.5a) and b), by using a 0.6 mm and a 2 mm diameter pinhole, respectively. Finally, in order to qualify the process for the final detector, three small diamond detectors (see Fig. 5.5a)) were fabricated with a 1 mm pitch strips by overlapping ten strips of 110 μm width.

We plan to fabricate the first real-size active target in October 2015, in order to be tested on the BTF beam in November 2015. The graphitic strips will have a thickness of about 100 nm and an electrical resistivity of about $4{\cdot}10^{-3}$ Ωcm, which corresponds to an overall electrical resistance of 6 KΩ for a 1×15 mm^2 strip.

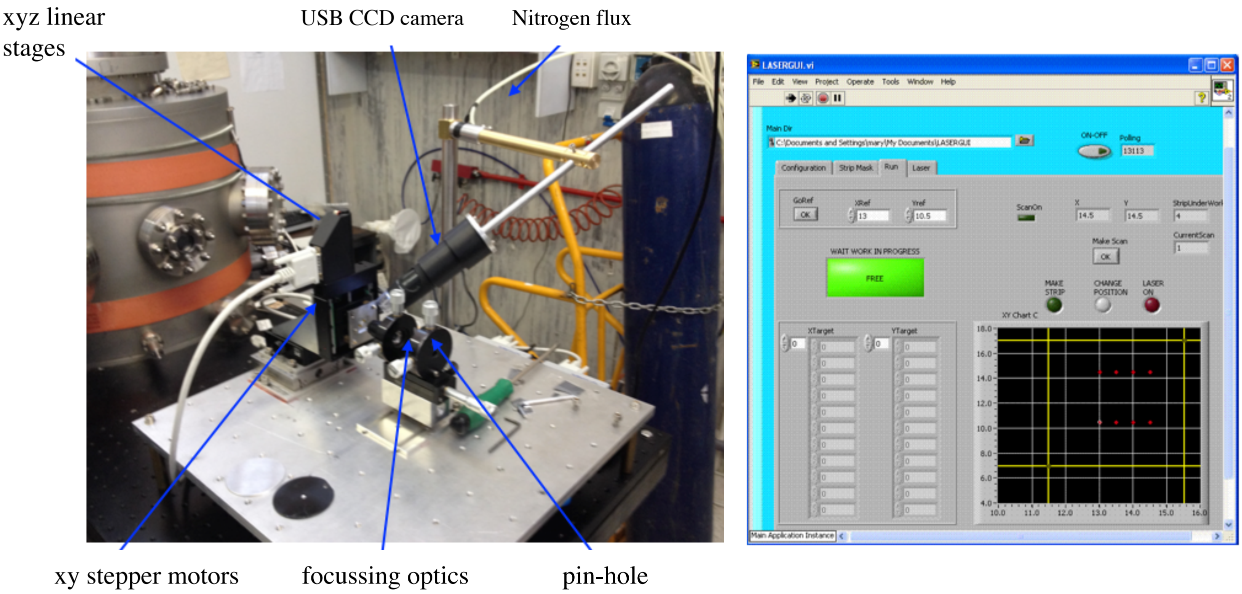

Figure 5.4: The new setup in Lecce to fabricate graphitic contacts on diamond surface with an excimer laser (left) and a snapshot of the Labview Graphical User Interface used to define and control the laser writing seguence.

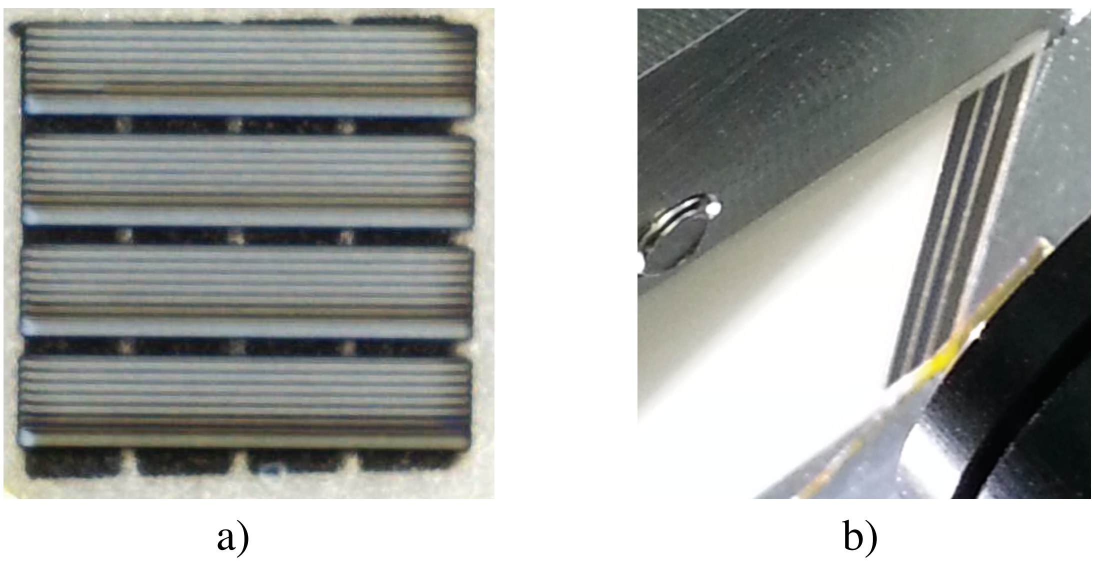

Figure 5.5: a) One of the three small size diamond detector prototypes made in July 2015 to qualify the electrode graphite fabrication process. The sensor size is 5×5 mm^2 and thickness 50 μm and the fabricated graphite strips were four on both sides. b) 1 mm graphitic strips, 18 mm long, during fabrication on the first 20×20 mm^2, 50 μm thick sensor with PADME parameters.

5.2.4 Diamond sensor response, spatial resolution and linearity.

In Fig. 5.6 the charge collection distance measured by Applied Diamond is reported. The measurement is compatible with our results obtained in November 2014 in a testbeam at BTF, with 500 MeV electrons, using a well known diamond detector as reference (see Fig. 5.7).

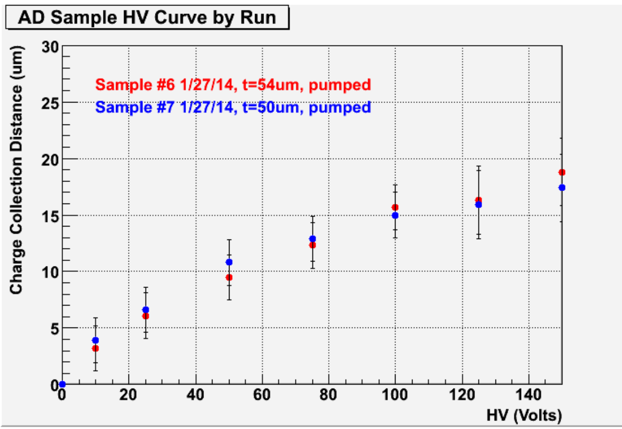

Figure 5.6: Charge collection distance measured by Applied Diamond Inc. (Delaware, USA) on two 50 μm thick, detector grade polycrystalline diamond sensors.

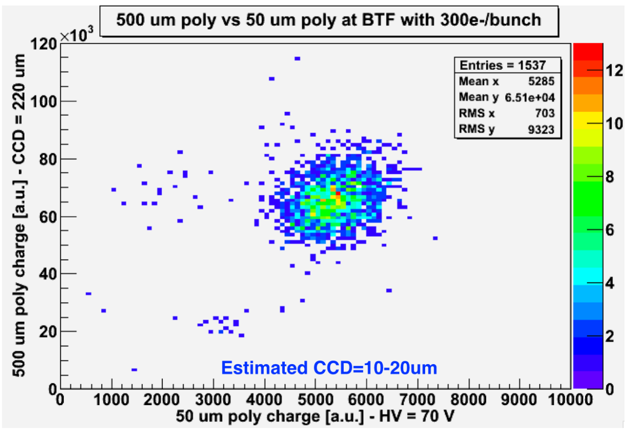

Figure 5.7: Charge correlation between a reference 500 μm thick detector grade polycrystalline diamond detector from Diamond Detector Ltd (UK) and a 50 μm thick polycrystalline diamond film provided by Applied Diamond Inc. (Delaware, USA) measured by us at BTF in Nov. 2014.

Assuming a conservative charge collection distance of about 10 μm, we expect a signal of about 360 electrons/mip. Because the electronic noise from the front-end should not exceed 1,000 electrons, we need about 17 mips get a signal-to-noise ratio of about 6. The number of electrons per bunch in the PADME experiment should be around $N = 2,000$ so that the device should be sensitive to most of the beam profile also if the spot area extends to many strips.

The signal fluctuation are expected to be dominated by the Poissonian statistics of the bunch multiplicity ($1/\sqrt{N}$, i.e. about 4.4% for $N = 500$). The Landau statistics of the ionization by a mip particle in a thin target can give significant fluctuations, as large as 25% for 50 μm thickness and 20% for 100 μm thickness [41]. However Landau fluctuations are suppressed by a factor $1/\sqrt{N}$ because the total signal is the incoherent sum of N electrons. Additional source of signal fluctuation could be related to not uniform charge collection properties of the material along a strip, which cannot be corrected by any calibration.

Furthermore, in the extraction of the average position of the beam profile these sources of fluctuation, even though they certainly weaken the strength of the charge weighting method for a single bunch measurement, have a limited impact when accumulationg more bunches together.

We aspect a linear response of the polycrystalline diamond in a large range of the electron bunch multiplicity, as measured on the BTF beam by the authors of [42]. Anyway, for low electron bunch multiplicity we have verified the linearity (see Fig. 5.8). This opens the possibility of measuring the total beam intensity bunch-by-bunch, by using the active target.

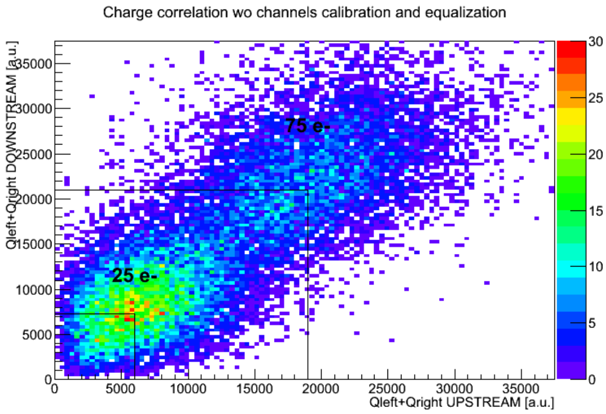

Figure 5.8: Charge correlation between two 500 μm thick detector grade polycrystalline diamond detector from Diamond Detector Ltd (UK) measured at BTF in Oct. 2014. The charge corresponds to the sum of two adjacent strips named left and right and two electron bunches with an average multiplicity of 25 and 75 electrons, showing good linearity.

5.2.5 Front-end electronics

The electric signal induced on the external circuit by the charge carrier drift could be amplified by a Charge Sensitive Amplifier (CSA) or by a Fast Voltage Amplifier (FVA). The CSA is generally followed by a shaper optimized to minimize the noise and to increase the count rate. The FVA is usually realized by a cascade of two RF amplifiers terminated at the input by a 50 Ω resistor.

The charge sensitive amplifier is better with respect to the fast voltage amplifier in terms of signal-to-noise ratio. The drawback of the charge sensitive amplifier is the timing resolution for time-of-flight applications. Finally, broadband amplifiers reproduce the induced signal allowing to studies the internal electric field and charge transport parameters.

The most performing fast CSA and FVA front-end amplifier for diamond detectors are realized by CIVIDEC ([37]). The CIVIDEC CSA has a gain of 8mV/fC, a 100 MHz bandwidth, with a rise-time and a pulse width of 2 ns and 7 ns, respectively, and a equivalent charge noise at the input of 750 electrons. The CIVIDEC FVA has a gain of 100, a 2 GHz bandwidth and 25 μV of electronic noise at the 50 Ω terminated input.

CIVIDEC built for us an instrument having 10 CSA and 10 FVA in a single box which can be used in the test-beam and to validate the final front-end configuration (see Fig. 5.9). With this instrument we can compare directly CSA vs. FVA in a real multichannel setup, similarly to the final experiment. Likely, we are going to use a front-end with CSA preamplifiers because better signal-to-noise ratio compared to FVA, but if space constrain is a problem, and the front-end must

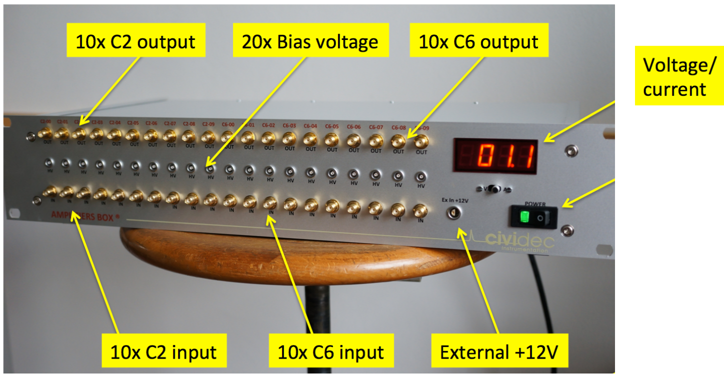

Figure 5.9: Amplifier box prototype of 10 Fast Charge Sensitive Amplifier and 10 Fast Voltage amplifier made by CIVIDEC to readout highly segmented diamond detector.

be placedd more than one meter away from the target, only the FVA solution can work because have the input terminated at low impedance.

The signals amplified by the amplifier box located very near to the detector are going to be digitized by V1742 CAEN digitizer like other detectors of the experiment. The expected cost of the CIVIDEC solution is about 1 K€ per channel, but less expensive solutions are going to be investigated, even though those will need further R&D activity, such as a diamond front-end similar to TOTEM upgrade and a APV25 micro-strip front-end chip.

However, since the uncertainty on the diamond detector response is still large, we take as baseline the most conservative design. In addition, the CIVIDEC amplifier provides the high voltage bias needed for the sensor, so that the printed-circuit (PC) board design is pretty much simplified.

5.2.6 PC board design

The PC board (PCB) must bias the sensor and readout the 32 signals. The bias is provided by the same CIVIDEC amplifiers which readout the signals. The PCB has also to hold very rigidly the diamond sensor to avoid mechanical torsions that could break it. In addition, the PCB routes the signal lines from the sensor assembly to the off-detector data readout, taking care of the vacuum/air interface.

The baseline solution is to use a rectangular vacuum flange on both sides, with the PCB vacuum sealed and providing the necessary feed-throgh for the signals without further intermediate connectors. In Fig. 5.10 a very preliminary sketch of the PCB is shown.

The PCB carriers has two square holes, one on the right and one on the left side. The sensor is going to be attached above one of the holes by low-outgassing epoxy below the sensor, using the dead area edge which is of about 2.5 mm.. In working conditions the PCB will be moved horizontally in order to center the sensor on the beam. Instead, while not in operation, the PCB will be moved horizontally about 1 cm to leave the beam to go through the hole, without hitting the diamond target. It will be extremely useful for monitoring and calibration purpose the possibility of removing the target remotely from the beam, without breaking the vacuum.

The signal strips are going to be electrically connected to the PCB by wire bonding with gold wires. We made in CNR-Nano-NNL laboratory in Lecce few successful tests of wire bonding on diamond graphitic structures (see Fig. 5.11). The wire bonding must be executed on both sides

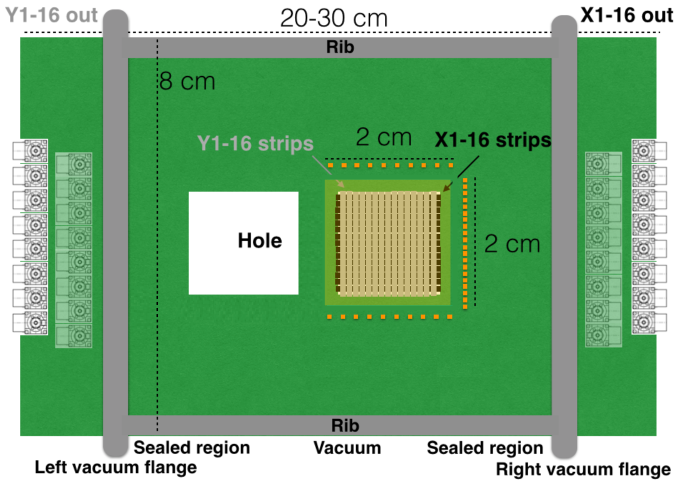

Figure 5.10: A preliminary sketch of the printed circuit board to readout and hold the active target in the vacuum chamber.

Figure 5.11: Wire bonding test on diamond graphitic structures made in CNR-Nano-NNL laboratory in Lecce.

and a careful procedure with appropriate fixture and handling must be worked out. A fall-back solution is to glue a comb of wire using the microscope. The latter is probably more robust and less risky for the sensor integrity.

16 SMA connectors will be soldered on the PCBleft and right sides in air, after the vacuum flange. The 16 SMA connectors are didived in two groups of 8, one group soldered on the front and the other group on the back side, in order to reduce the vertical size of the board.

The PCB is going to be realized with four metal layers: top and the bottom layers for low impedance ground, and the two intermediate layersused for x and y signals, respectively.

5.2.7 Mechanical structure design

A very preliminary scheme for the active target mechanical structure is shown in Fig. 5.12. The main idea is to use the PCB as vacuum electrical feed-through in order to avoid many connectors and changes of electrical impedance of the signal lines between bench-top tests and the real experiment.

In addition, in order to allow to move remotely the target in and out of the beam, two lateral vacuum bellows connect the two rigid cross circular flanges, not glued to the PCB, and two movable circular flanges sealed to the PC board. The two movable circular flanges seat rigidly on a movable horizontal table where the box amplifiers are also positioned.

5.2.8 Scheduled beam-tests

We have scheduled in November 2015 a beam-test at BTF with 50 μm thick diamond detector prototype which should be built in October 2015 in Lecce. The front-end electronics is going to be the CIVIDEC amplifier box prototype with the output signals stored by V1742 CAEN digitizer available for the PADME testbeam in VME crates.

The primary goal of the test is to measure the electron bunch profile along x and y and compare with the one obtained by a FITPIX hybrid silicon pixel detector having a active area of 1.41×1.41 cm^2 and 256×256 pixel matrix (pixel area of 55×55 μm^2)

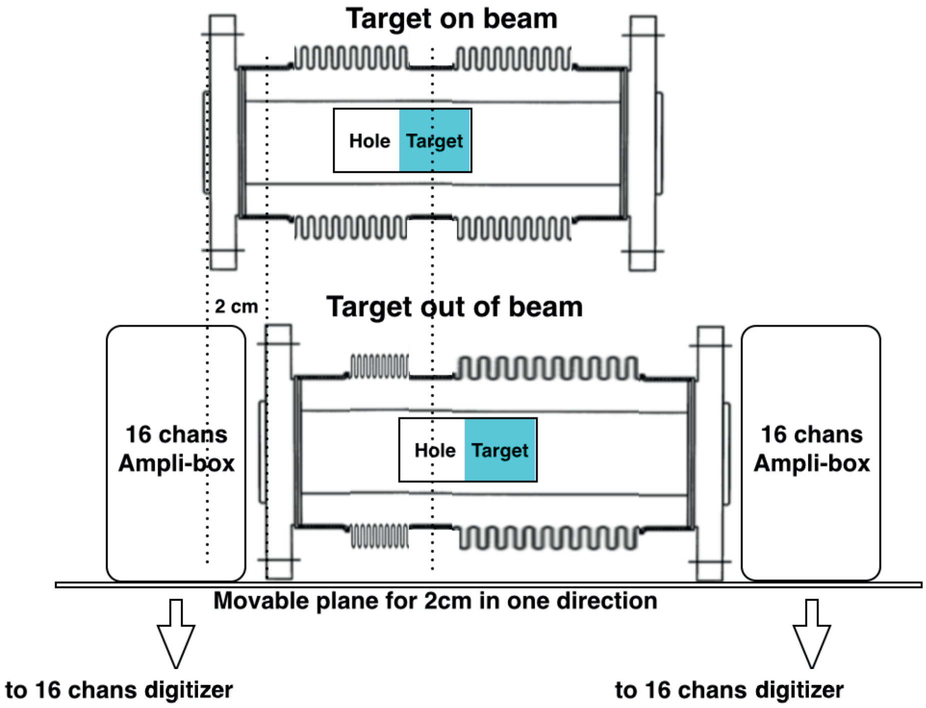

Figure 5.12: Preliminary sketch of the mechanical support and setup of the active target.

In Fig. 5.13 the 2D beam profile measured at the BTF during a test in October 2014 is shown, with 25 electrons per bunch, as imaged by a FITPIX detector:

- The top plots a) and b) show the transverse position of electrons in a single bunch for two different bunches.
- The left bottom c) plot shows the 2D scatter plots of the electrons for many bunches, representing a typical BTF beam profile. The beam profile had a horizontal and vertical spread of about 1.1 mm in both directions.
- The right bottom plot d) shows the 2D scatter plots of the average x and y electron position, accumulated for about 2,200 bunches.

This very preliminary test demonstrate that only averaging over many bunches it is possible to extract a profile for the beam, at low intensity, but such a test at low intensity does not fully reproduce the case of a 10^4 electrons/bunch. Indeed the fluctuation of the average of the beam center for many, low intensity bunches, are small (≈ 5 times less the beam profile size, in this case, i.e. 250 μm) but not negligible, so that for a realistic test of bunch-by-bunch monitoring of the PADME beam should be performed with a realistic $\sim 10^4$ particles/bunch configuration.

5.2.9 Costs

In Tab. 5.2 the core cost of the active target is divided in the main components and we believe it comprises already a fair contingency. The target cost includes VAT, and 2 K€ for diamond sensor prototypes spent in 2015.

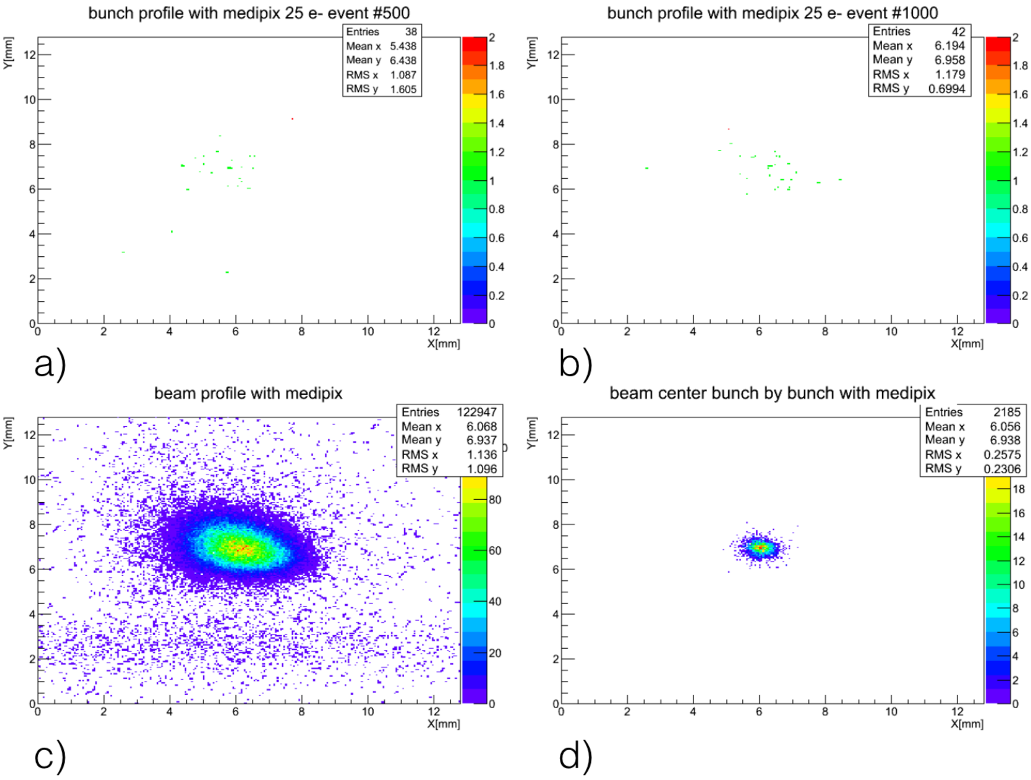

Figure 5.13: beam spot.

Item	Cost (K€)
Diamond target with CrAu metalization	2+5
HV power supplies	10
Detector Control System	5
Mechanics	5
1D remote movement	5
Front-end electronics	40
Total	**72**

Table 5.2: Active diamond target core cost.

5.3 The magnet

5.3.1 PADME magnet requirements

The positron beam of $10^3/10^4$ particles/pulse (depending mainly from the pile-up probability, and in turn from the pulse duration) will interact with the very thin PADME target, passing through almost undisturbed. We have designed a calorimeter with a central hole in order to reduce the photon rate from the dominant Bremsstrahlung process, but we also need to drive away from the calorimeter acceptance the primary positrons. For this purpose we need a magnetic field of a minimum strength given by the angular deviation that in turn is fixed by the lateral dimension of the calorimeter.

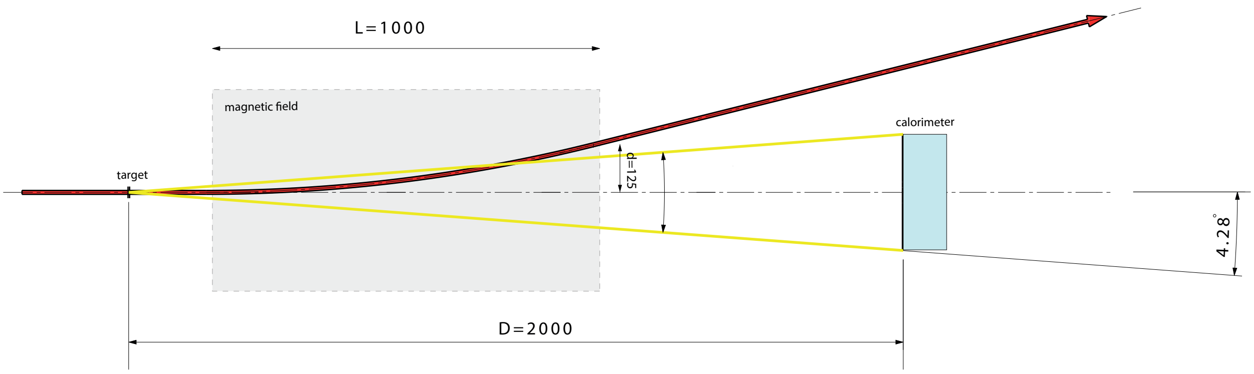

Figure 5.14: Schematic of PADME calorimeter acceptance: in the baseline layout, the calorimeter front face is at a distance of 2 m from the active target.

In the baseline configuration of PADME, shown in Fig. 5.14, the angular acceptance of the calorimeter is fixed at $4.3° = 75$ mrad. (see 5.4), so that this is the minimum deflection angle for non-interacting primary positrons, i.e. of energy $E_0 = 650$ MeV. In designing the magnet we also took into account the possibility of a future upgrade of the linac, bringing the maximum positron energy in the range of ≈ 1 GeV. In order to have some headroom and taking into account the space needed for the vacuum pipe, we fix a deflection of at least $d = 125$ mm at 1 m distance, or $\Delta\phi > 125$ mrad. The known relation: $\Delta\phi/2 = \arcsin L/2\rho$, where L is the length and ρ the curvature radius, can be used in the small angle approximation $\Delta\phi \simeq \frac{L}{\rho}$, so that we can find the minimum integrated magnetic field BL_{min}:

$$(BL)_{min}\,[\mathrm{Tm}] \simeq \Delta\phi \cdot (B\rho) = 0.125 \cdot 3.3356\, p\,[\mathrm{GeV}]/c$$

i.e. $(BL)_{min} \approx 0.42$ Tm for $p = 1$ GeV/c.

The other parameter fixed by the acceptance of the calorimeter is ratio between the transverse aperture (both horizontal and vertical) of the magnet and the distance to calorimeter face. Taking into account the PADME layout, this requirements translates in a ± 10 cm gap over a magnet lenght of 1 m. The minimum bending then requires a moderate magnetic field of 0.42 T.

In addition to the sweeping of the primary beam, by equipping the sides of the magnetic field region with segmented detectors, the magnet can also allow measuring the momentum of the positrons that have lost some energy passing through the target, thus helping in the rejection of Bremsstrahlung background. For this purpose, the magnetic field should be as uniform as possible to allow a reasonably good determination of the momentum, by measuring the hit position along the magnetic field region.

Putting together these two functions, the basic requirements for the PADME magnet are listed in the following Tab. 5.3, adding the costraints on weight and maximum power, coming from the BTF crane maximum load (30 ton) and the availability of spare power supplies in Frascati.

Parameter	Value
B field	> 0.42 T
Length	1 m
Vertical gap	20 cm
Horizontal gap	> 40 cm
Weight	< 30 ton
Power	< 100 KW

Table 5.3: Main requirements for the PADME sweeping/analysing magnet.

In designing the PADME experiment, and in particular defining the main parameters for the magnet, we have established a contact with the TE-MSC-MNC group of the CERN engineering department, responsible for the design, costruction, operation and maintenance of the normal-conducting magnets of the CERN accelerators and facilities.

A preliminary sketch for the PADME magnet has been prepared, according to the requirements of Tab. 5.3, in the option of a custom new electromagnet, and is shown in Fig. 5.15. An informal very preliminary cost estimate for such a magnet can be placed in the order of magnitude of 150 kEur (including the power supply).

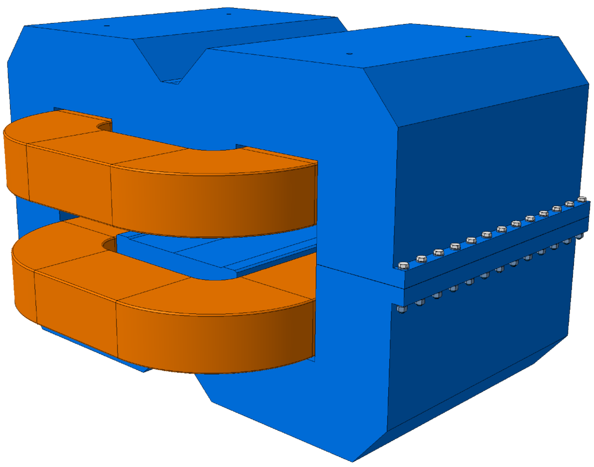

Figure 5.15: Preliminary sketch of a possible electromagnet according to the PADME requirement by CERN TE-MSC-MNC section (courtesy Davide Tommasini).

5.3.2 CERN MBP magnet for PADME

During these preliminary studies, the possibility of re-using an existing spare magnet from the CERN accelerators was raised. Thanks to the collaboration with CERN, a candidate magnet type has been identified in the MBP dipoles of the SPS transfer lines. In particular, these H-shaped bending electromagnets were produced in two versions: "short" (MBP-S), 1 m length, and "long" (MBP-L), 2 m length, with equal cross section, with poles of 52 cm length in the horizontal dimension and variable vertical gap, from 11 to 20 cm. Two variants are available, one with straight, rectangular poles, one with tapered poles, shown in Fig. 5.16. The maximum field at the maximum gap of 20 cm is ~ 1.4 T, when powering the magnet at the maximum operational current of 675 A, corresponding to a power of 95 KW. The total weight is 15 ton.

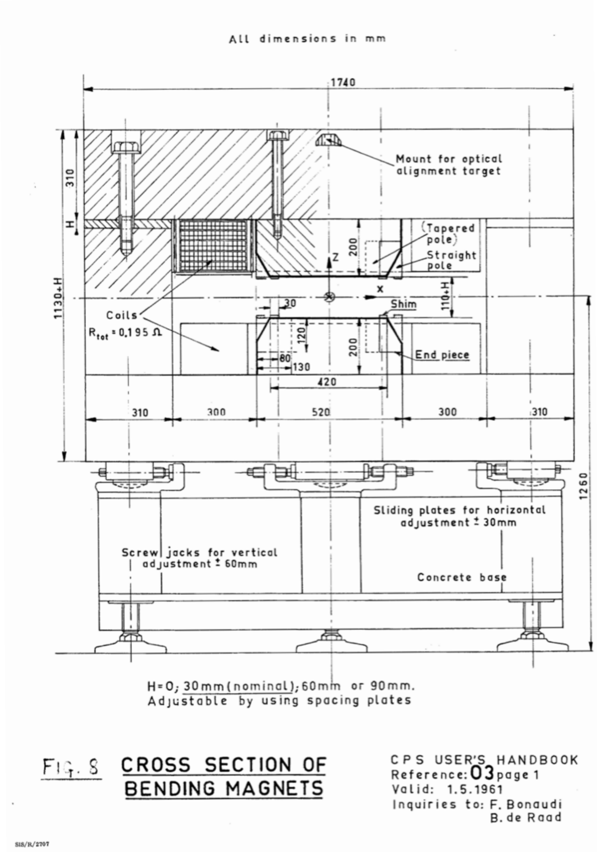

Figure 5.16: Drawing of CERN dipole magnet, type MBP (from [32]).

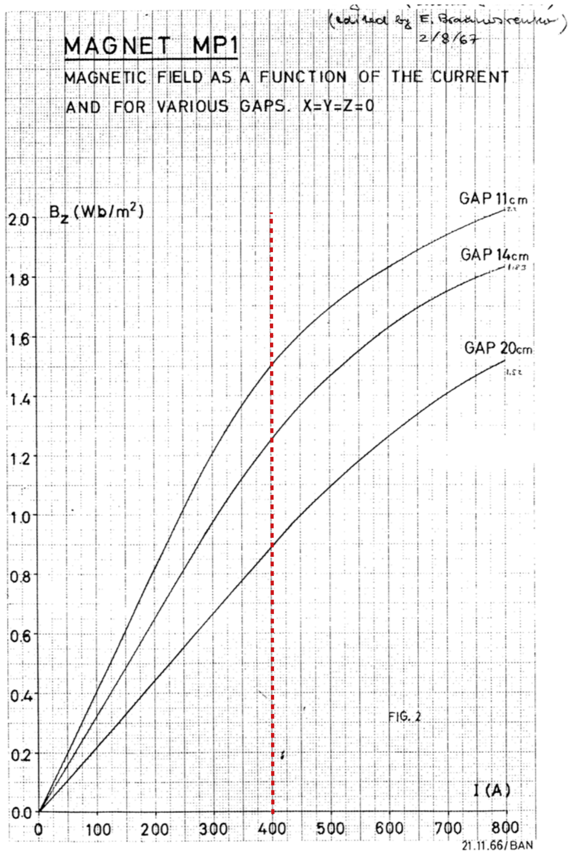

Figure 5.17: Maximum B field as a function of the excitation current for MBP dipoles (from [32]).

A preliminary investigation in the LNF accelerator division allowed us to identify a power supply of almost the required specifications, capable of reaching 80 V/400 A, located in the main DAΦNE power supply building. In Fig 5.17 the measured maximum magnetic field of MBP-S magnets, showing also the value that can be reached with the LNF power supply (≈ 0.9 T for a gap of 20 cm), is shown.

Suitable cables will be needed from the power supplies hall to the BTF experimental area, as well as a proper cooling circuit for the magnet. The existing manifolds existing in the BTF hall should be sufficient for the need of the MBP-S magnet.

Once the magnet will be shipped to Frascati, a field mapping campaign will be performed, using the measuring probe mounted on the motorized stages available in the Magnetic Measurement Laboratory of the Accelerator Division (see Fig. 5.19), with a span (especially in the longitudanl dimension) that should be sufficient for getting an accurate map.

The weight of the magnet, 15 ton, is well within the specifications of the crane in BTF hall.

Figure 5.18: MBP-S spare dipole, id. M112 (in the CERN TE-MSC-MNC laboratory), during refurbishing (September 2015).

Figure 5.19: The B field measuring machine in the magnetic measurement laboratory of the LNF accelerator division.

Another important point from the infrastructure point of view is the magnet support, that shoul allow positioning and adjusting the magnet on the beam line with a good accuracy. Unfortunately, no spare support for the MBP type magnets was available at CERN.

A number of iron insets are available at CERN for adjusting the magnet gap between 11 and 20 cm, in particular 3 and 6 cm high pieces are available. We plan to set the gap at 23 cm, by using two 6 cm insets, in order to have a better handle in adjusting the distance of the calorimeter without shadowing its top and bottom edges (see Fig. 5.20). Of course, the quality and the value of the magnetic field with this larger gap has to be carefully measured.

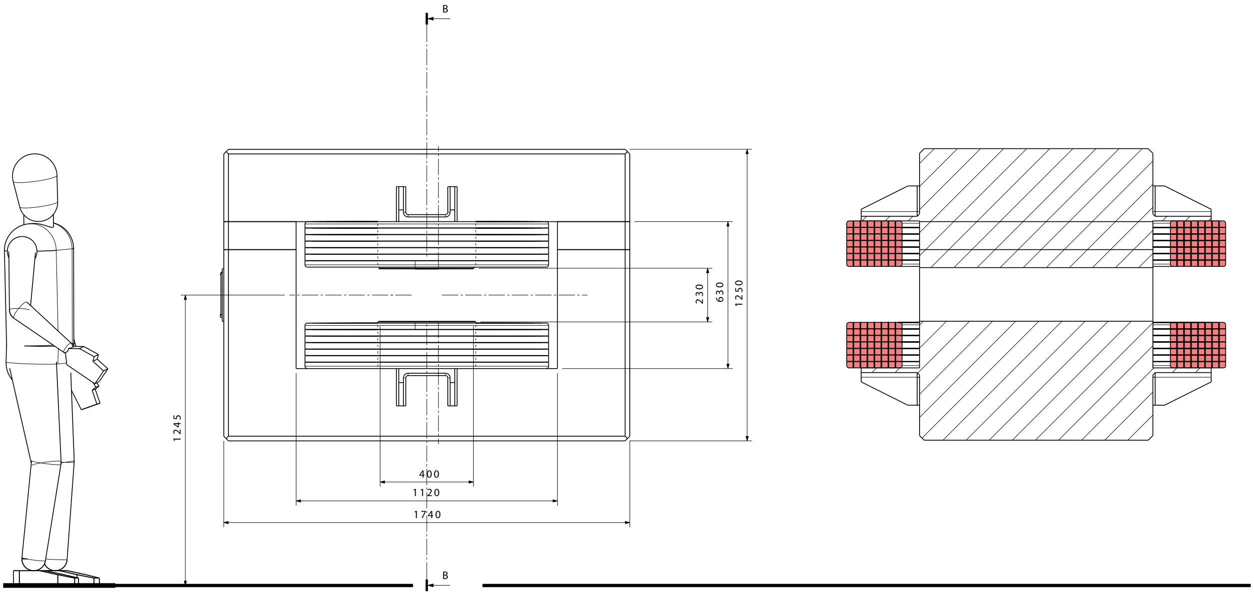

Figure 5.20: Overall dimensions of the MBP-S magnet adapted for PADME, with a vertical gap of 23 cm.

Another relevant point concerning the B map, is the residual magnetic field at the position and around the active target, due to the effect on the positron beam trajectory. In the present layout the diamond target is placed at 20 cm from the end of iron pole of the magnet, but still inside the coils, at a longitudinal distance (along the z coordinate) from the center of 70 cm. According to the existing measurements of the MBP-type magnets, for a gap of 11 cm at 400 A current the field at $z = \pm 70$ is of the order of 10–15% of the maximum value (see Fig. 5.21). For the final, larger gap (23 cm), we expect a rounder shape of the field, with a shorter flat top and a more gentle slope for the fringe, so that the B value at the position of the target could be even lower, in addition, the maximum magnetic field will be significantly lower. Since we plan to run at B_{max} =0.4–0.5 T, we can estimate a residual field of the order of 400-500 Gauss.

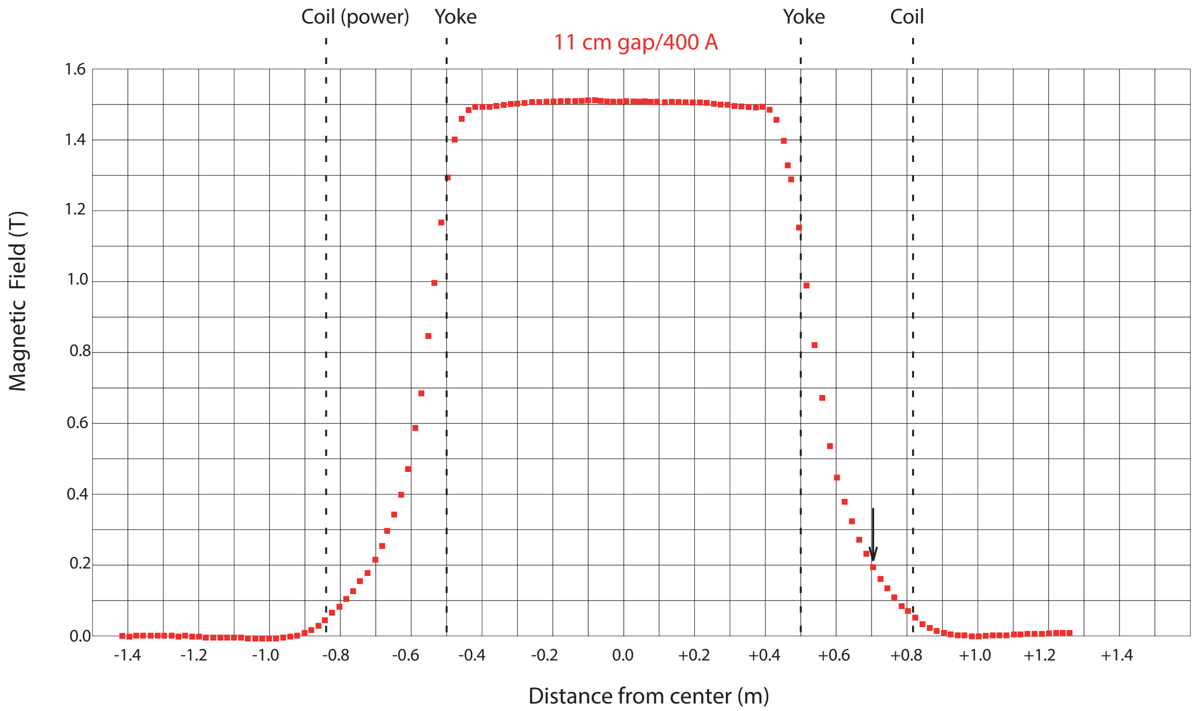

Figure 5.21: B field as a function of the longitudinal coordinate z (at the center $x = y = 0$), for a gap of 11 cm and excitation current of 400 A (adapted from [32]).

5.4 The calorimeter

The most important part of the PADME experiment will be the calorimeter. The detector should provide high precision measurement of photon energy, direction and time at the calorimeter surface in a very compact and cost-effective way.

To avoid pile up due to the high number of primaries in each single bunch, the calorimeter will have a central hole in order not to accept most of Bremsstrahlung photons produced by the target. The detector section will be approximately circular with an optimized inner and outer radius depending on its distance form the target. The detector dimensions are fixed by the size of the BTF hall imposing a limit to the target–calorimeter distance. In the present configuration of the BTF experimental hall (shown with a sketch of the PADME setup in Fig. 4.14), the maximum distance target–calorimeter is ≈ 5 m. Some space, of the order of 1.5 m, can be recuperated by re-designing the transfer line, e.g. moving the quadrupole doublet outside the experimental hall.

The requirement of the PADME calorimeter are the following:

- Energy resolution: 1–2 $\%\sqrt(E)$ in GeV
- Time resolution: ~ 0.5 ns
- Angular resolution: ~ 1 mrad
- Very small size

5.4.1 Defining calorimeter geometry and materials

The recoil photon angular distribution defines the acceptance of the calorimeter for dark photon searches. For this reason the angular acceptance has been defined by looking ad the angle between the photon and the incoming positron beam in the dark photon generator in Fig. 5.22. This angle turned out to be independent of the dark photon mass.

The choice of the angular acceptance in our case is not arbitrary, since we have a maximum vertical gap of our MBP-S magnet of ± 115 mm (see Sec. 5.3), which, together with the longitudinal position of the active target, fixes the maximum angle seen by the calorimeter. By choosing a maximum angle of 4.3° and fixing the hole at 1°, we will collect $\sim 66\%$ of the angular distribution of recoil photons, for a 650 MeV positron beam (see Fig. 5.22) .

The lateral dimension of the calorimeter R_{out} will be finally fixed by the distance D from the target, as shown in Fig. 5.23. In the present design with a calorimeter to target distance of 2 m, with the target slightly inside the coils of the magnet (10 cm from the coils edge, and 20 cm from the front face of the magnet pole), translating in an inner radius of 4 cm and a outer radius of 15 cm. The behaviour of the photon acceptance also shows that there will be a relatively low gain in extending the size of the calorimeter in order to cover higher angles, while in the lower angles region a limitation at $\sim 1^\circ$ comes from Bremsstrahlung background and crystals size. .

Given the calorimeter dimensions and the beam energy, the choice of the materials is rather limited. Fig. 5.24 shows the main characteristics of the most widely used crystals in the electromagnetic calorimetry in high energy physics [43].

The simultaneous requirement of high density, small radiation length X_0 and Moliére radius R_M (due to the calorimeter small dimensions), and high light output (due to the low energy range), practically leaves only two possible solutions: LYSO and BGO. Due to shorter decay time the LYSO would be the best choice even if it is rather expensive. In fact operating the beam with a long bunch duration (> 100 ns) more than one calorimeter cluster could be identified and separately measured in the same bunch using a digitiser based readout.

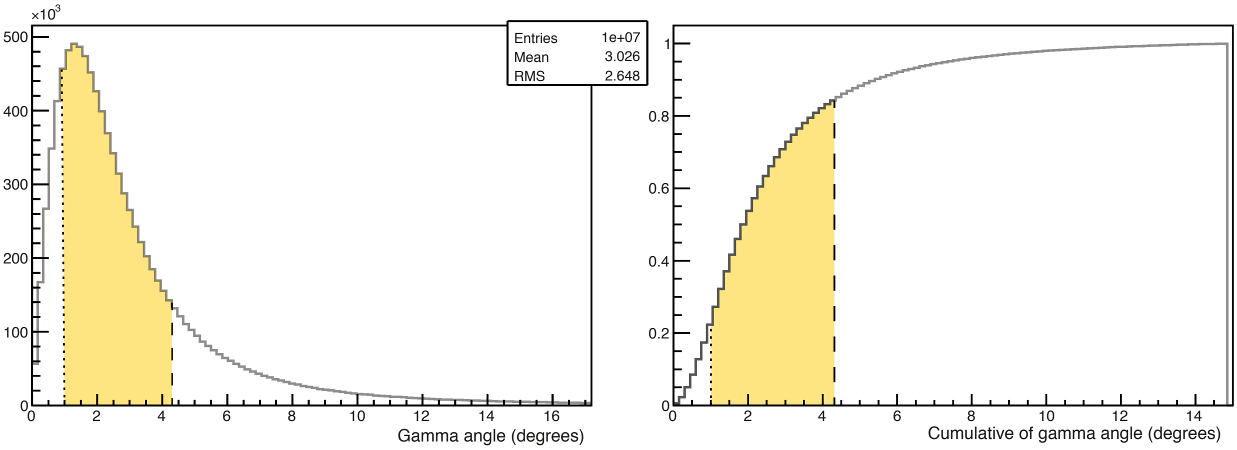

Figure 5.22: Distribution of the associated photon angle with respect to incident beam direction (left) and its cumulative, i.e. the acceptance vs. angular cut (right). The selected angular region, in the range 1°–4.3° is shown as a shaded area.

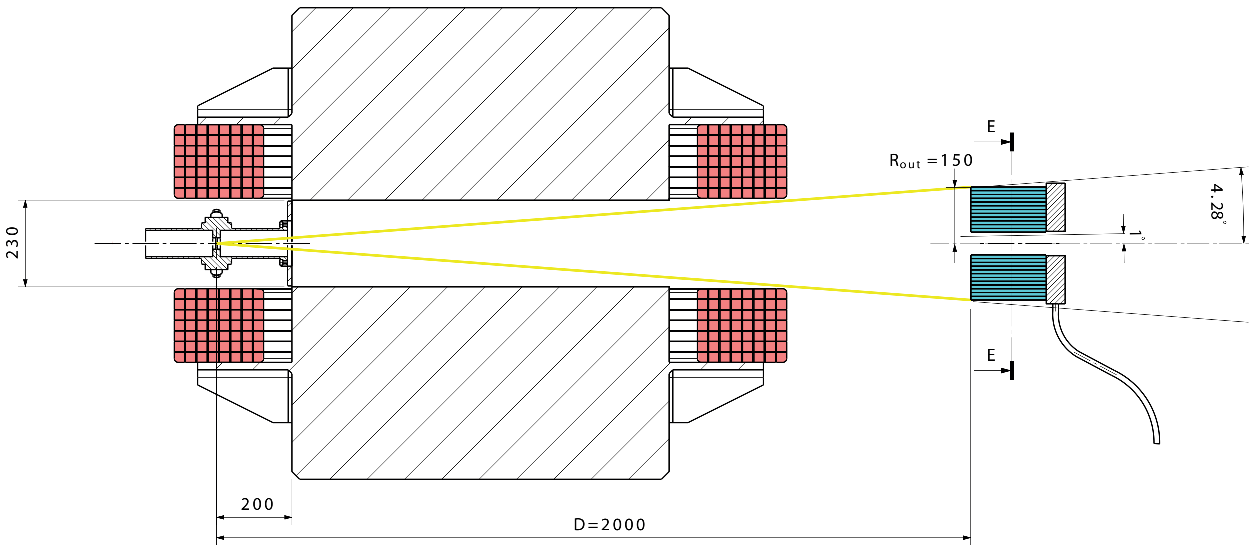

Figure 5.23: Lateral view of the MBP-S magnet for PADME, showing the angular acceptance when the active target is placed ≈ 10 cm inside the magnet coils, i.e. at 20 cm from the magnet pole front face.

Parameter:	ρ	MP	X_0^*	R_M^*	dE^*/dx	λ_I^*	$\tau_{\rm decay}$	$\lambda_{\rm max}$	$n^\natural$	Relative output†	Hygro-scopic?	d(LY)/dT
Units:	g/cm^3	°C	cm	cm	MeV/cm	cm	ns	nm				%/°C‡
NaI(Tl)	3.67	651	2.59	4.13	4.8	42.9	245	410	1.85	100	yes	-0.2
BGO	7.13	1050	1.12	2.23	9.0	22.8	300	480	2.15	21	no	-0.9
BaF_2	4.89	1280	2.03	3.10	6.5	30.7	650^s	300^s	1.50	36^s	no	-1.9^s
							0.9^f	220^f		4.1^f		0.1^f
CsI(Tl)	4.51	621	1.86	3.57	5.6	39.3	1220	550	1.79	165	slight	0.4
CsI(pure)	4.51	621	1.86	3.57	5.6	39.3	30^s	420^s	1.95	3.6^s	slight	-1.4
							6^f	310^f		1.1^f		
$PbWO_4$	8.3	1123	0.89	2.00	10.1	20.7	30^s	425^s	2.20	0.3^s	no	-2.5
							10^f	420^f		0.077^f		
LSO(Ce)	7.40	2050	1.14	2.07	9.6	20.9	40	402	1.82	85	no	-0.2
$LaBr_3$(Ce)	5.29	788	1.88	2.85	6.9	30.4	20	356	1.9	130	yes	0.2

* Numerical values calculated using formulae in this review.
$^\natural$ Refractive index at the wavelength of the emission maximum.
† Relative light output measured for samples of 1.5 X_0 cube with a Tyvek paper wrapping and a full end face coupled to a photodetector. The quantum efficiencies of the photodetector are taken out.
‡ Variation of light yield with temperature evaluated at the room temperature.
f = fast component, s = slow component

Figure 5.24: Properties of several inorganic crystal scintillators[43].

We recently discovered the possibility of collecting part of the dismissed L3 electromagnetic calorimeter, which was composed of $\sim$ 11,000 BGO crystals. Few hundreds of the original crystals may come for free, allowing the assembly of the PADME calorimeter at the costs of just cutting the crystals in the required shape. The drawback of BGO as material for the PADME calorimeter is related to the long decay time. With $\sim 1\mu$s long BGO signals, the PADME calorimeter can only be used in the regime of single cluster per beam-pulse, thus limiting the maximum number of primary positrons. We are collecting all available crystals (currently we have 150 of them), part of which were purchased by the INFN Roma unit, with the aim of realizing the entire calorimeter for PADME.

Several studies were performed for the PADME calorimeter before changing the basic material choice from LYSO to the BGO. Due to almost identical properties of the two material they remain valid if BGO is used instead.

The segmentation of the PADME calorimeter front face plays a crucial role determining the detector angular resolution, which is a key ingredient in the missing mass resolution of the entire experiment. For practical reasons – like the size of the photo-sensors, mechanical stability of the crystals, and dead spaces – the minimum size of the crystals front face is limited to $\sim 10 \times 10$ mm^2, thus providing a spatial resolution of the order of few mm in the transverse (x-y) plane.

Our baseline solution is thus 10×10 mm^2 front face dimensions, which allows us to realize a quite compact calorimeter. In order to have the required angular resolution of $\sim$ 1 mrad, a distance from the target of 2 m has to be chosen. The total number of crystals, with a central hole of 4 cm radius, is then 656, arranged in the layout shown in Fig. 5.25.

The longitudinal dimension of the crystal has been studied by using a GEANT4 Montecarlo simulation. A monochromatic beam of photons has been shoot on the front face of the calorimeter in a central fixed position and the reconstructed energy studied for different longitudinal dimensions of the crystals (15–20 cm). Fig. 5.26 shows that a shorter than 20 cm calorimeter is unable to properly

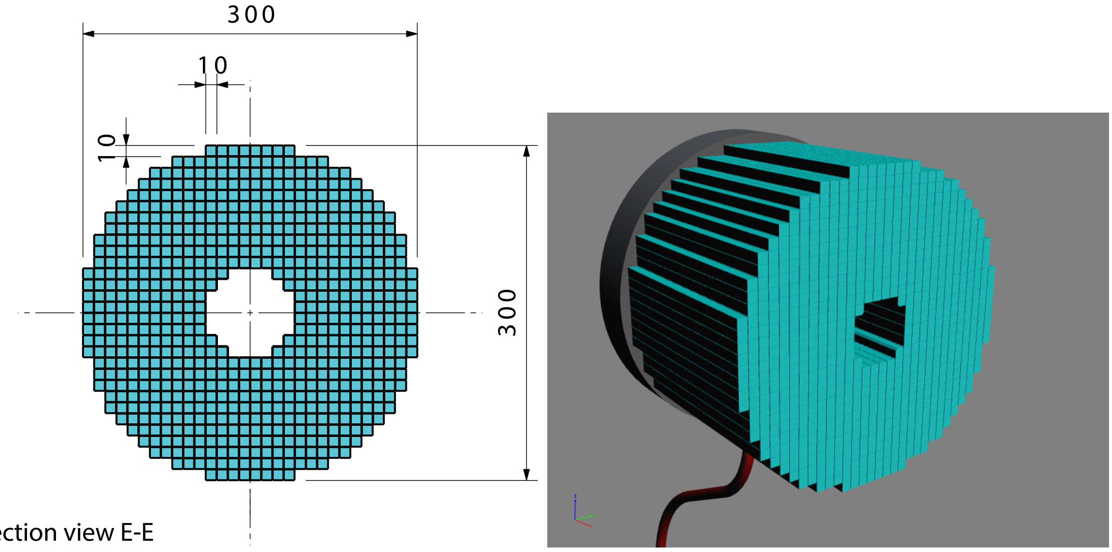

Figure 5.25: Layout of the 656 crystals, with front face of 1×1 cm^2, arranged in order to have an internal hole of radius 4 cm and a outer radius of 15 cm, and corresponding 3D model.

contain the photons electromagnetic showers or to provide a proper energy resolution scaling. The green line, just placed to guide the eye, shows the resolutions ($\sigma_E/E = \frac{1.1\%}{\sqrt{E}} \oplus \frac{0.4\%}{E} \oplus 1.2\%$) obtained in the R&D for the calorimeter of the SuperB project in tests with LYSO crystals at the BTF [44] .

The BGO crystals used by the L3 experiment were 23 cm long allowing to obtain a 22 cm long sample after cutting and polishing the crystals again.

The BGO energy resolution has been extensively studied during the L3 experiment R&D. In particular some low energy test were performed with electrons down to 180 MeV, which are more interesting for the operation of the BGO in the PADME environment [45]. As shown in Fig. 5.27 a) resolution as good as $\sigma_E/E = \frac{1.57\%}{\sqrt{E}} \oplus 0.35\%$, very similar to that obtained with LYSO in a similar energy range at the BTF, Fig. 5.27 b) was obtained.

Concerning the required energy resolution for the PADME calorimeter, toy Monte Carlo studies of the missing mass vs. calorimeter energy resolution, shows that both LYSO and BGO are able to provide the required resolution (see Fig. 5.27 c)). Energy resolution is indeed crucial to obtain a good missing mass resolution as demonstrated by the slope in figure.

For this reason we decided to perform a beam-test campaign to validate the choice of the BGO as material for the calorimeter. In parallel, contacts with L3 collaboration have been started to understand the amount of crystals which can be reused from the dismounted L3 calorimeter.

Summarising, in the present basic experiment design the calorimeter will be an approximate cylinder with a diameter of 300 mm and depth of 220 mm, filled with $10 \times 10 \times 220$ mm^3 BGO crystals, with an approximately round central hole of 40 mm radius. The active volume will be 9840 cm^3 for a total of 656 crystals, obtained by cutting BGO crystals from the dismantled L3 calorimeter. The calorimeter will be placed at 2 m form the diamond target, thus covering the angular region from 1.1° to 4.3°, and providing an energy resolution in ther range 1–2%$\sqrt(E)$.

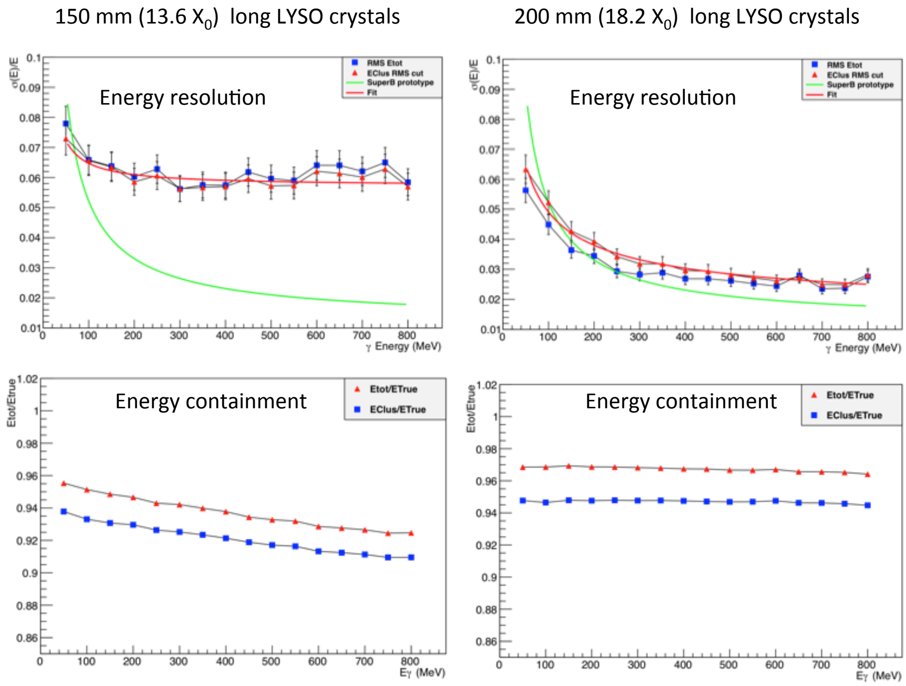

Figure 5.26: Energy resolution (top) and shower containment (bottom) for two different crystal lengths.

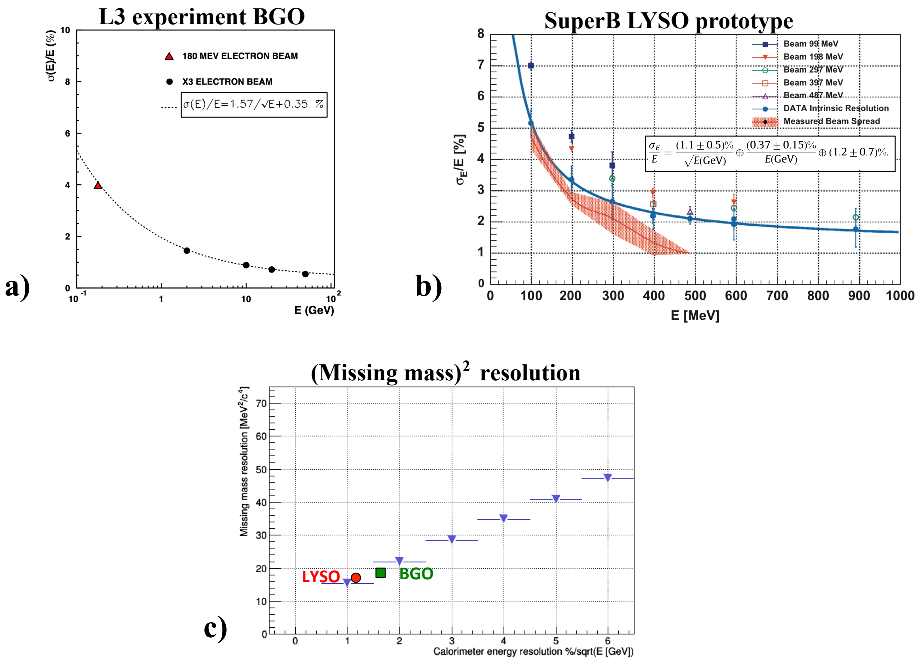

Figure 5.27: a) Energy resolution of L3 BGO calorimeter. b) Energy resolution of SuperB LYSO calorimeter prototype. c) Missing mass resolution of the PADME experiment as function of the calorimeter energy resolution.

5.4.2 First beam-test results

Studying the possibility of reusing the BGO from the L3 calorimeter, we have performed a first test with beam at the BTF, with a 3×3 matrix, made of original crystals of trapezoidal prism shape, 240 mm long, approximately 22×22 mm^2 front face and 30×30 mm^2 back face. The nine crystals still have their original Teflon reflective painting, we have wrapped them in white paper just for mechanical protection. We have removed the original photodiodes, reading each crystal with a 1" Hamamatsu bialkali photomultiplier tube, see Fig. 5.28.

The analog signals from the photomultipliers were digitized by a CAEN V1742 flash-ADC board (32 channels), at 1 GS/s, providing 1024 12-bit resolution samples, corresponding to a total waveform length of 1 μs (shown in Fig. 5.29). The waveforms have been stored by a dedicated DAQ system to disk for each trigger, provided by the DAΦNE linac timing signal for each beam bunch sent to the BTF line, at a variable repetition rate (depending on the operation of the DAΦNE collider) from 2 Hz (during injections) up to 50 Hz (actually, only 49 out of 50 bunches per second were delivered to the BTF line, as explained in Sec. 4.3).

The same trigger signal was fed to one of the two trigger inputs of the V1742 board, in order to provide a precise time reference (otherwise the start of digitization has an intrinsic jitter of 25 ns due to the digitizer clock). The trigger signal was adjusted (by means of the BTF digital delay) in order to have beam particles ≈ 100 ns after the start of digitization, thus giving about 100 samples for the baseline evaluation. The beam intensity was tuned to a Poissonian with average between 1 an 2 electrons/bunch, with selected energy of 450 MeV.

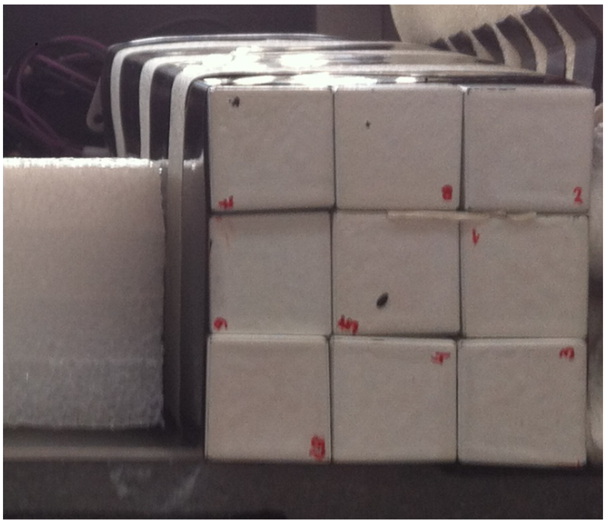

Figure 5.28: The 3×3 BGO crystals matrix inside the dark-box, ready for the first beam-test at BTF.

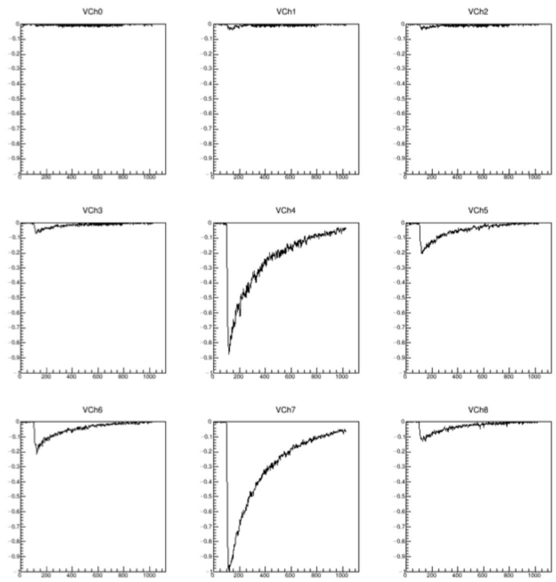

Figure 5.29: An example of the 3×3 BGO crystals matrix analog signals, for 450 MeV electrons at BTF, digitized by a CAEN V1742 board.

With the acquired waveforms from each of the nine crystals the charge can be computed, by simply summing up the signal current for each of the 1024 samples and subtracting the baseline value. Being the maximum value of the sampled voltage 1 V, the digitized signals were often clipped, so that the computed charge without any correction clearly shows a saturation effect when more than one 450 MeV electron leaves energy in the same crystal, as shown in Fig. 5.30 and in the total charge spectrum in Fig. 5.31. This effect can be taken into account and clipped signals can be treated by fitting with a suitable function the waveform, thus recovering the saturation. Moreover, this effect is due to the typically high gain of the photomultipliers and should be less important when reading the crystals with APDs.

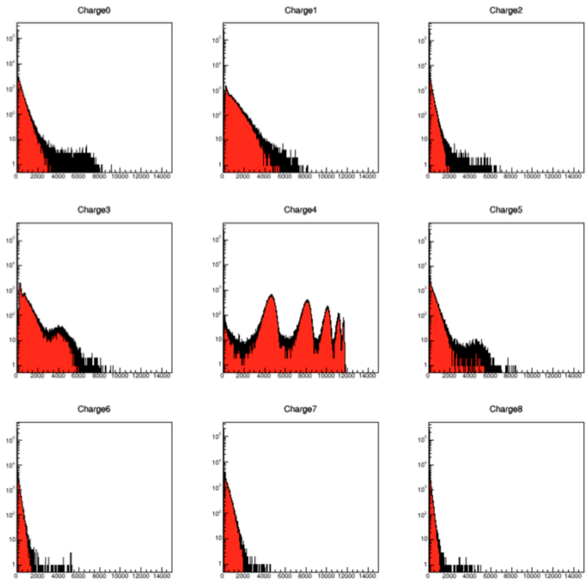

Figure 5.30: Reconstructed charge from the digitized signals of the 3×3 BGO crystals matrix, for 450 MeV electrons at BTF.

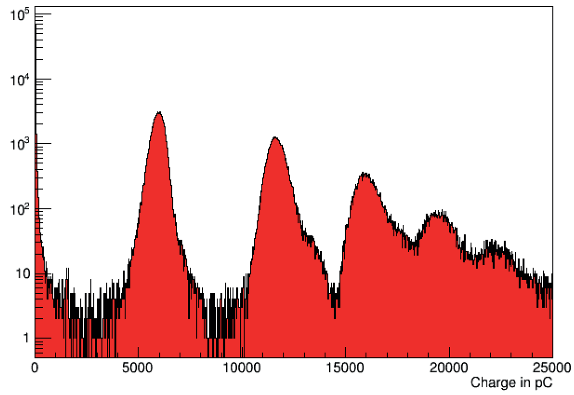

Figure 5.31: The 3×3 BGO crystals matrix: total charge for 450 MeV electrons.

An example of best fit to the waveform for signals without or with saturation is shown in Fig. 5.32: the fit function is the convolution of a Landau with two exponential (one for the fast and one for the slow decay time of the light). By using the fit value for the maximum amplitude of the signal, the linearity of the calorimeter is recovered, as shown in Fig. 5.33.

By charge-weighting the x and y values of the hit crystals, the baricenter of the energy deposit can be evaluated. Of course border effects will spoil the evaluation of the baricenter with such a small number of crystals: with a 3×3 matrix, border effects show up already when the cluster is not centered in the central cell, as shown in Fig. 5.34. However, these very preliminary results already show the potential of reconstructing the cluster position with a resolution of the order of 6 mm for 2×2 cm^2 crystals (3 mm with 1×1 cm^2 granularity), since the BTF beam spot is much smaller.

5.4.3 Calorimeter photo-sensors

Due to the very small size of the calorimeter crystals of 10×10 mm^2 the choice of the photo-sensors is rather limited. Excluding photomultipliers tubes, too big to be contained in such a small surface, our investigations have been concentrated on solid state photo-sensors.

We explored two possibilities: Avalanche Photo Diodes (APD) and Silicon Photo Multipliers (SiPM). The first solution offers good linearity in a wide range of charges, very high quantum efficiency at the price of a low gain and higher cost with respect to SiPM. On the other hand SiPM are known to have a non linear behaviour, as soon as the number of photons impinging on them exceeds approximately half of the total number of available cells, and high dark current.

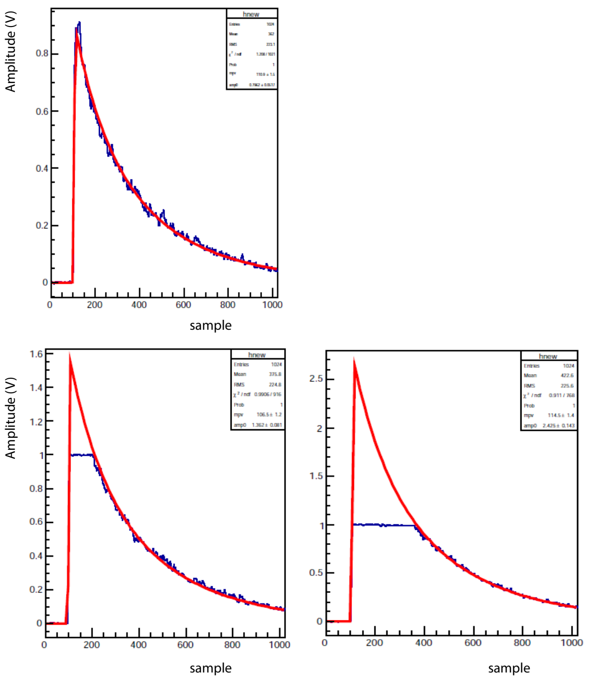

Figure 5.32: Digitized waveform of a BGO crystal (the one with most of the deposit from the 450 MeV electron beam of BTF), with superimposed the fit to the Landau + two exponentials function (see text).

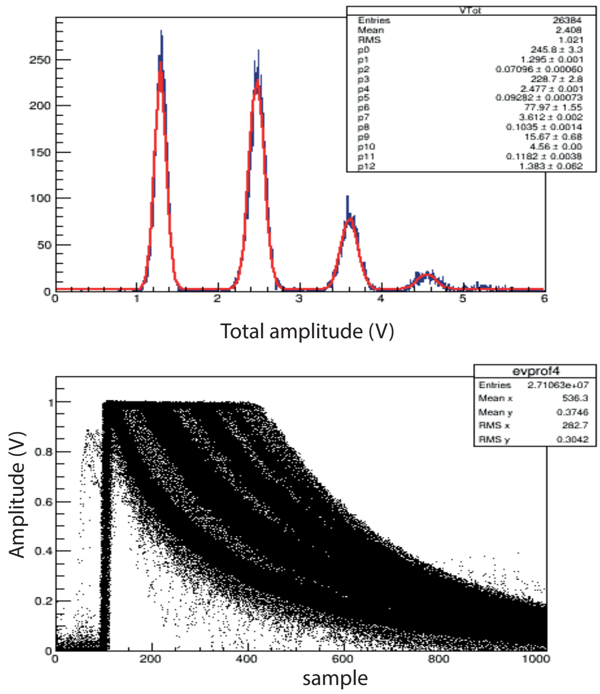

Figure 5.33: Spectrum of the maximum amplitude as extracted from the fit function, showing a good linearity. The quantization due to the deposit of 1, 2, 3 or 4 electrons of 450 MeV energy is also visible in the original waveforms, with a worse separation due to the saturation at 1 V from the digitizer chip.

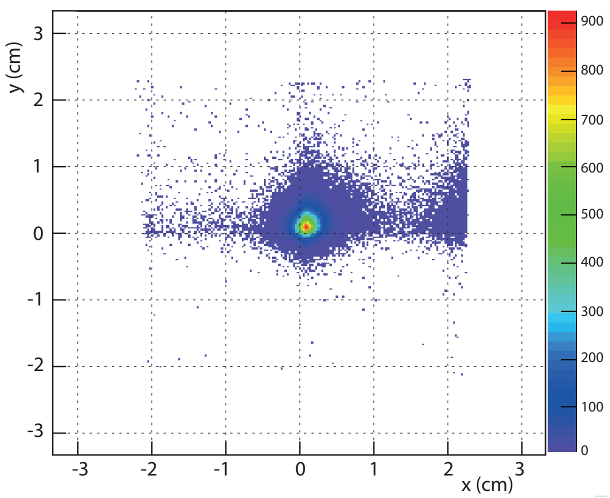

Figure 5.34: Baricenter of the reconstructed charges from the digitized signals of the 3×3 BGO crystals matrix, for 450 MeV electrons at BTF.

Recent development by Hamamatsu led to SiPM sensors with up to 90,000 cells on a 3×3 mm^2 surface, see Fig. 5.35. For this reason they are considered as a possible option for the calorimeter readout. Test beam are required to test their linearity up to energy of impinging photons of ~ 600 MeV, with 10×10 mm^2 BGO crystals.

Two photo-sensors have been identified to possibly match the PADME calorimeter mechanical design and readout needs, which are presented in Fig. 5.35.

MPPC 3x3 mm^2 S12572

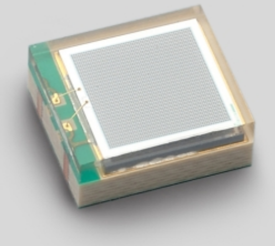

Parameter	-010C	-010P	Unit
Effective photosensitive area	3 × 3		mm
Pixel pitch	10		µm
Number of pixels	90000		-
Geometrical fill factor	33		%
Package	Ceramic	Surface mount type	-
Window	Epoxy resin		-
Window refractive index	1.59	1.55	-

APD 5x5mm S8664-55

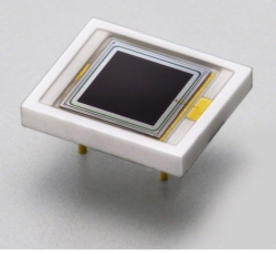

Type No.	Spectral response range λ (nm)	Peak *3 sensitivity wavelength λp (nm)	Photo sensitivity S M=1 λ=420 nm (A/W)	Quantum efficiency QE M=1 λ=420 nm (%)	Breakdown voltage VBR ID=100 µA Typ. (V)	Max. (V)	Temperature coefficient of VBR (V/°C)	Dark *3 current ID Typ. (nA)	Max. (nA)	Cut-off frequency fc (MHz)	Terminal *3 capacitance Ct (pF)	Excess *3 Noise index λ=420 nm	Gain M λ=420 nm
S8664-02K	320 to 1000	600	0.24	70	400	500	0.78	0.1	1	700	0.8	0.2	50
S8664-05K								0.2	1.5	680	1.6		
S8664-10K								0.3	3	530	4		
S8664-20K								0.6	6	280	11		
S8664-30K								1	15	140	22		
S8664-50K								3	35	60	55		
S8664-55								5	50	40	80		
S8664-1010								10	100	11	270		

*1: K: Borosilicate glass E: Epoxy resin
*2: Area in which a typical gain can be obtained.
*3: Values measured at a gain listed in the characteristics table.

Figure 5.35: Possible Hamamatsu photo-sensors for the crystal calorimeter readout.

The baseline solution will be to use a single 5×5 mm^2 APD S8664-55 on each of the PADME calorimeter crystals. These devices are almost identical to the one used in the CMS electromagnetic calorimeter so that the technology is well consolidated and ancillary system requirements such as bias voltage and temperature monitors are already well known. The solution will offer a 25% surface coverage and a very good matching in between photocathode sensitivity and BGO emission with a quantum efficiency exceeding 80% (see Fig. 5.36) The price of the sensor has been quoted from Hamamatsu to be ~ 122 €/piece for large productions. In the SiPM case the solution will be to use four 3×3 mm^2 S12572-10P offering a 36% surface coverage, but smaller global quantum efficiency (order 10%) due to the very small fill factor of the 10 μm. In alternative to Hamamatsu SiPMs, in the market several other solutions are available; we have considered so far FBK, Advansid, SensL, as described in more detail in Sec. 5.6.1.

5.4.4 Calorimeter front-end electronics

5.4.5 Calorimeter readout electronics

To get the best energy resolution and a large charge integration dynamic a readout solution based on digitisers has been chosen for the calorimeter. Due to the small amount of channels in the experiment (~ 700) the calorimeter readout electronics will be based on commercial fast digitisers solution to reduce development costs, time, and man power.

The adopted solution for the electromagnetic calorimeter will be extended to the small angle

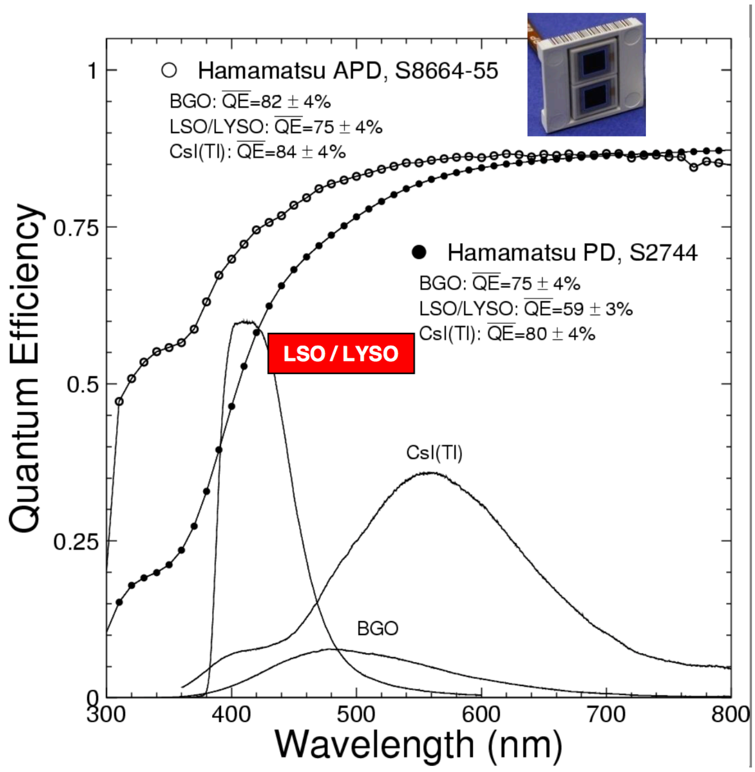

Figure 5.36: Matching of quantum efficiency and emission spectrum for BGO with Hamamatsu S8664 APD.

calorimeter and to the target as well. The requirement are derived from the shape of the signal produced by the BGO crystals. Digtization window of at least $1\mu s$ is required to sample the entire BGO signal. Due to the wide dynamic range of energy deposit in the calorimeter crystals, from few MeV up to 400 MeV, a 12 bit digitizer is desirable, while to assure a good timing resolution a digitization frequency $\sim$ 1 GS/s is foreseen. Finally, the system has to be cheap enough to digitize $\sim$ 700 channels at a reasonable cost.

Recently different Flash ADC boards were developed based on a digitiser chip called DRS-4 (Domino Ring Sampler) chip, developed ad Paul Scherrer Institut [46]. In particular CAEN has developed a VME 6U board called V1742 which we are considering as baseline solution for the PADME calorimeter.

The V1742 is a VME Switched Capacitor Digitizer board housing 32+2 Channels (12 bit, up to 5 GS/s) based on DRS-4 (Domino Ring Sampler) chip, with 1 Vpp input dynamic range on single ended MCX coaxial connectors. The analog input signals are continuously sampled into the DRS-4s in a circular analog memory buffer (1024 cells); default sampling frequency is 5 GS/s but 2.5 GS/s and 1 GS/s frequencies can be also programmed.

As a trigger signal arrives, all analog memory buffers are frozen and subsequently digitized with a 12 bit resolution into a digital memory buffer. The digital memory (128 events deep for each channel, where 1 event = 1024×12 bit) allows to store subsequent events, even if the readout is not yet started. Two special fast analog trigger inputs TR0 and TR1 (TTL/NIM levels compatible), can be sampled into the DRS-4s analog memory buffers for applications where high resolution timing and time analysis with a common reference signal (like a trigger or system clock) is required.

Additional techinical specification can be found in Fig. 5.37. The board houses a daisy chainable Optical Link able to transfer data at 80 MB/s, thus it is possible to connect up to eight ADC boards (256+16 ADC channels) to a single Optical Link Controller. The board cost is $\sim$ 8 K€ + V.A.T. which leads to a price per channel of 300 €.

Package	1-unit wide VME module
Analog Input	32 channels (MCX 50 Ohm); Single-ended; Input range: 1 Vpp Bandwidth: >500MHz; Programmable DAC for Offset Adjust x ch. adjustment range: ±1V
Sampling frequency	Programmable: 5, 2.5 or 1GS/s
TR0, TR1 Input	MCX 50 Ohm, NIM/TTL; fast local trigger (TR0 for ch0..15, TR1 for ch16..31) and high resolution timing reference
Switched Capacitor array	Based on DRS4 chip Switched capacitor ADC 1024 storage cells per channels simultaneously sampled at 5 - 2,5 - 1GS/s (selectable) on all channels After trigger analog samples are digitized by external ADC.
Digital Resolution	12 bit
Dead Time	110µs Analog inputs only; 181µs Analog inputs + TR0, TR1 inputs
ADC Sampling Clock generation	sampling clock generation supports two operating modes: PLL mode - internal reference (50 MHz local oscillator) PLL mode - external reference on CLK_IN (Jitter<100ppm, Freq. 50 MHz).
Digital I/O	CLK_IN (AMP Modu II): AC coupled differential input clock LVDS, ECL, PECL, LVPECL, CML (single ended NIM/TTL available on request) Jitter<100ppm TRG_IN (LEMO 50 Ohm, NIM/TTL) S_IN (LEMO 50 Ohm, NIM/TTL)
ADC & Memory control FPGA	1 Altera Cyclone EP3C16 for 16+1 channels
Memory Buffer	128 event/ch, (1024 samples per event); Multi Event Buffer with independent read and write access.
Trigger	Common Trigger TRG_IN (External signal) Software (from VME or Optical Link) Fast local trigger Fast local trigger TR0 and TR1 with individual programmable analog threshold
Optical Link	CAEN proprietary protocol, up to 80 MB/s transfer rate, Daisy chainable: it is possible to connect up to 8/32 ADC modules to a single Optical Link Controller (Mod. A2818/A3818)
Multi Modules Synchronization	Allows data alignment and consistency across multiple V1742 modules: CLK_IN allows the synchronization to a common clock source S_IN ensures start acquisition times alignment
Upgrade	Firmware can be upgraded via VME/Optical Link
VME interface	VME64X compliant D32, BLT32, MBLT64, CBLT32/64, 2eVME, 2eSST, Multi Cast CyclesTransfer rate: 60MB/s (MBLT64), 100MB/s (2eVME), 160MB/s (2eSST). Sequential and random access to the data of the Multi Event Buffer. The Chained readout allows to read one event from all the boards in a VME crate with a BLT access.
Software	Libraries (C and LabView), Demos and Software tools for Windows and Linux

Figure 5.37: Technical specifications of the CAEN V1742 board.

Being a switching capacitor board, V1742 offers a relatively cheap cost per channel at the price of not being a real time digitiser board. In fact once the analog memory buffers are frozen to store a signal the boards is unable to receive a new signal before the digitiziation process is terminated in all the channels. For this reason the boards has a dead time of 110μs analog inputs only and 181μs analog inputs + TR0, TR1 inputs. This limitation is not severe in the case of PADME because the interval in between two different beam bunches is 20 ms. Nevertheless the limitation of 1024 samples stored in the analog memory forces to operate the board in the 1 GS/s sampling rate to allow 1 μs digitization time window. In case of very high signals from BGO crystals, their duration can exceed 1μs limiting the capability of the board to collect the full charge.

The PADME calorimeter readout will make use of 22 V1742 boards, divided into two groups of 11, digitizing the two calorimeter sectors (left and right). The sectors will have their own VME crate housing the V1742 boards and – in case – small angle calorimeter and target digitizers.

Each of the two sectors will be connected via optical link to a dedicated server HP Proliant DL560 server, with a total of 32 cores, housing the CAEN optical receiver board CAEN A3818. The A3818 boards has four optical connectors each able to control eight V1742 boards and to manage a transfer rate up to 80 MB/s. The number of available link will be enough to collect also data coming from SAC and target digitizers boards. The total amount of boards presently foreseen is 24 (22 from calorimeter, plus one for the active target and one for the small angle calorimeter): they will be equally divided among six of the available eight links, i.e. four boards per link. The remaing links will be used a spare.

The trigger will be dispatched in NIM standard from the Trigger Distribution system to all the V1742 boards at the same time. Upon receiving the trigger all the boards will digitize the 1024 samples and send them to the servers through optical links. The total amount of data load produced can be estimated. On each of the link there will be four digitizers sending 1024 samples of 12 bits per each channel leading to $4\times(32+4)\times1024\times12$ bits$\times50 = 88.5$ Mbits/s including trigger signals. Comparing with the optical link speed we have a safety factor of ~ 8 in the data throughput. The total amount of data received from each of the servers will be 3×88.5 Mbits/s= 265.5 Mbits/s very far from PCIExpress-x8 transfer speed specifications.

Basic building blocks of the readout system, namely V1742 board, A3818 optical receiver and HP Proliant DL560 server, are already been tested during the first PADME test beam.

5.4.6 Possible alternative for DAQ electronic boards

As an alternative to the proposed DAQ readout based on 32 channels CAEN V1742 modules, we are also evaluating modules in development by Sitael for the CTA experiment and by S. Ritt (PSI-Zurich) for the MEG-II experiment.

Sitael for CTA-INFN

Sitael is the largest Italian privately-owned Company operating in the Aerospace Sector and has been already working with INFN in several electronics related projects, like CTA, AMS and others.

Sitael is now developing a full readout module for the CTA experiment (design developed together with INFN-BA) to be used in conjunction with FBK SiPMs. Fig. 5.38 shows the general scheme for the board electronics being developed. The prototype development is quite well advanced and some test modules could be available by the last quarter of 2015 for testing.

The main characteristics of the electronics are :

1. 16 (maybe 32) channels input;
2. SiPM amplifiers circuitry built in;
3. zero-pole filters for SiPM signals built in;
4. HV controls built in for FBK SiPMs;
5. FPGA for background control/trigger built in;
6. already foreseen exit on Gigabit Ethernet;
7. very compact board;

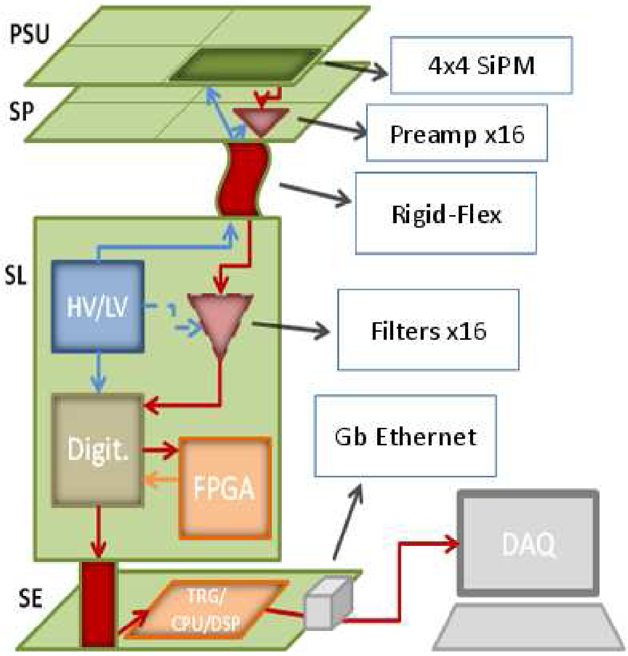

Figure 5.38: Scheme of the Sitael electronics.

8. capable of high DAQ rates and good timing.

The presence of a zero-pole filter circuitry can be useful in conjunction with the usage of fast crystals (lyke LYSO or BaF_2) but is probably not useful for crystals with long signals, like BGO. Further studies will be needed in order to tailor the present design to the PADME requirements.

The usage in the final stage of an embedded FPGA can allow use to make locally the signal zero suppression and the triggering of the event in a very efficient way.

WaveDream for MEG-II

Very recently [51] we have become aware of a very interesting prototype of digitizer electronics based on the DRS4 chip being developed for the MEG II upgrade by the author of the chip Prof. S. Ritt at PSI-Zurich.

The WaveDream board (see scheme in Fig. 5.39) has very advanced and interesting characteristics and could be available since 2016, which would fit nicely our time schedule.
Its main characteristics are :

1. 16 channels input;
2. SiPM amplifiers circuitry built in;
3. HV controls built in (for Hamamatsu SiPM);
4. temperature sensor possibly built in;
5. FPGA for background control/trigger;
6. high bandwidth and low latency;

7. precise timing (Goal: < 5 ps clock jitter at system level);
8. data output on Gigabit Ethernet;
9. power over Ethernet evolution possible.

The usage of an embedded FPGA can allow use to make locally the signal zero suppression and the triggering of the event in a very efficient way.

However there are also less favorable features, like the need for dedicated DAQ VME-like crates, as well as the fact that the project is still in the development phase, and the final MEG-II board will be probably ready in 2016.

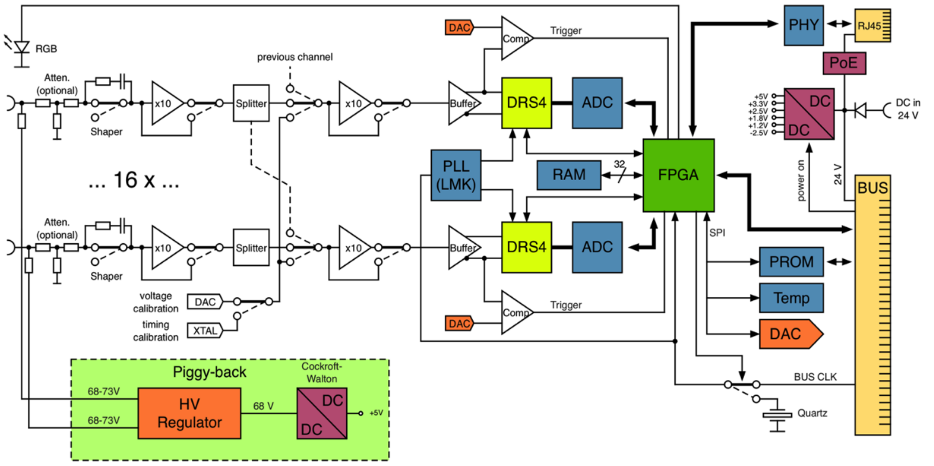

Figure 5.39: Scheme of the WaveDream module.

Figure 5.40: An image of the WaveDream module prototypes being tested at PSI.

5.4.7 Calorimeter reconstruction

Clustering Algorithm

An electromagnetic shower in a crystal calorimeter usually appears as a local maximum in a localized array of crystal energy deposits, spread over an area whose size is related to the Moliére radius of the crystal. A precise reconstruction of the shower energy requires the collection of the largest possible fraction of the deposited energy, while avoiding the collection of energy from nearby particles or noisy crystals.

The problem is then usually reduced to a pattern finding algorithm (clustering algorithm) which, starting from crystals with a local energy maximum, called "seeds", collects energy from nearby crystals and creates energy clusters, in principle associated with individual electromagnetic showers.

Noise-related fluctuations in the reconstructed energy content of a crystal together with the application of energy thresholds, either implicit (as that coming from the DAQ zero suppression algorithm) or explicit, can induce limits on the final energy resolution of each clustering algorithm due to two main effects: bump splitting, where a single electromagnetic shower is seen as two contiguous clusters due to an energy fluctuation, and energy loss at the cluster edge due to noise suppression or noise fluctuations.

Depending on the energy collection strategy, each clustering algorithm will be more or less affected by these two effects. The final choice of the algorithm will then depend on the context in which the algorithm will be used (energy scale, crystal and readout properties, etc.) and on the final optimization requirements coming from the physics goals of the experiment (energy resolution, spacial resolution, adjacent showers separation, etc.).

For PADME we are currently testing two clustering algorithms which present substantially different energy collection strategies.

The Box Clustering Algorithm The PADME Box clustering algorithm is based on the identification of a set of crystals centered on the cluster seed and whose centers are contained within a given radius from the center of the seed.

In detail, the PADME algorithm starts from the list of all crystals in the event which pass the L0 zero-suppression criteria. This list is sorted by decreasing energy content (highest energy first) and all crystal are initially tagged as "not in use".

The first crystal of the list, i.e. the one with the highest energy, is chosen as the seed for a new cluster: the cluster is created, the seed is attached to it, and the corresponding crystal is tagged as "in use".

From the center of the seed, a circle of given radius is drawn and all crystals whose center falls within the circle are examined: if the crystal has some energy deposit and is not "in use", i.e. it was not previously attached to another cluster, it is attached to the current cluster and tagged as "in use". When the loop over all crystals within the circle ends, the cluster is complete.

The list of crystals is then scanned for the first "not in use" crystal: this will be the seed for a new cluster and the whole algorithm is repeated. Besides the circle radius, the only other tuning parameter for the algorithm is the seed threshold energy, i.e. the minimal raw energy required for a crystal to be used as seed: the algorithm terminates when no crystals can be found that are "not in use" and have an energy above this threshold.

Fig. 5.41 shows an example of how the Box algorithm works: starting from the seed crystal (in red), all crystal within the blue circle are used to form the cluster delimited by the thick outline.

The Island Clustering Algorithm The PADME Island clustering algorithm started from the Island algorithm in use for the CMS electromagnetic calorimeter [62] and modified it in order to remove the directional asymmetry between the η and ϕ axes (corresponding to our x and y axes) specific to that method and to simplify the crystal collection algorithm through a recursive search method.

In detail, the PADME algorithm starts from the list of all crystals in the event which pass the

L0 zero-suppression criteria. This list is sorted by decreasing energy content (highest energy first) and all crystal are initially tagged as “not in use”.

The first crystal of the list, i.e. the one with the highest energy, is chosen as the seed for a new cluster: the cluster is created, the seed is attached to it, and the corresponding crystal is tagged as “in use”.

A recursive “cluster expansion” algorithm is then applied to the seed: its four adjacent crystals are checked and if they are “not in use” and have an energy which is inferior to that of seed, they are in turn attached to the cluster, tagged as “in use”, and the “cluster expansion” algorithm is applied to them. When the initial instance of the “cluster expansion” recursive algorithm terminates, the cluster is complete.

The list of crystals is then scanned for the first “not in use” crystal: this will be the seed for a new cluster and the whole algorithm is repeated. The only tuning parameter for the algorithm is the seed threshold energy, i.e. the minimal raw energy required for a crystal to be used as seed: the algorithm terminates when no crystals can be found that are “not in use” and have an energy above this threshold.

Fig. 5.42 shows an example of how the Island algorithm works: starting from the seed crystal (in red), adjacent crystals are collected in the order shown by the numerated arrows to obtain the cluster delimited by the thick outline.

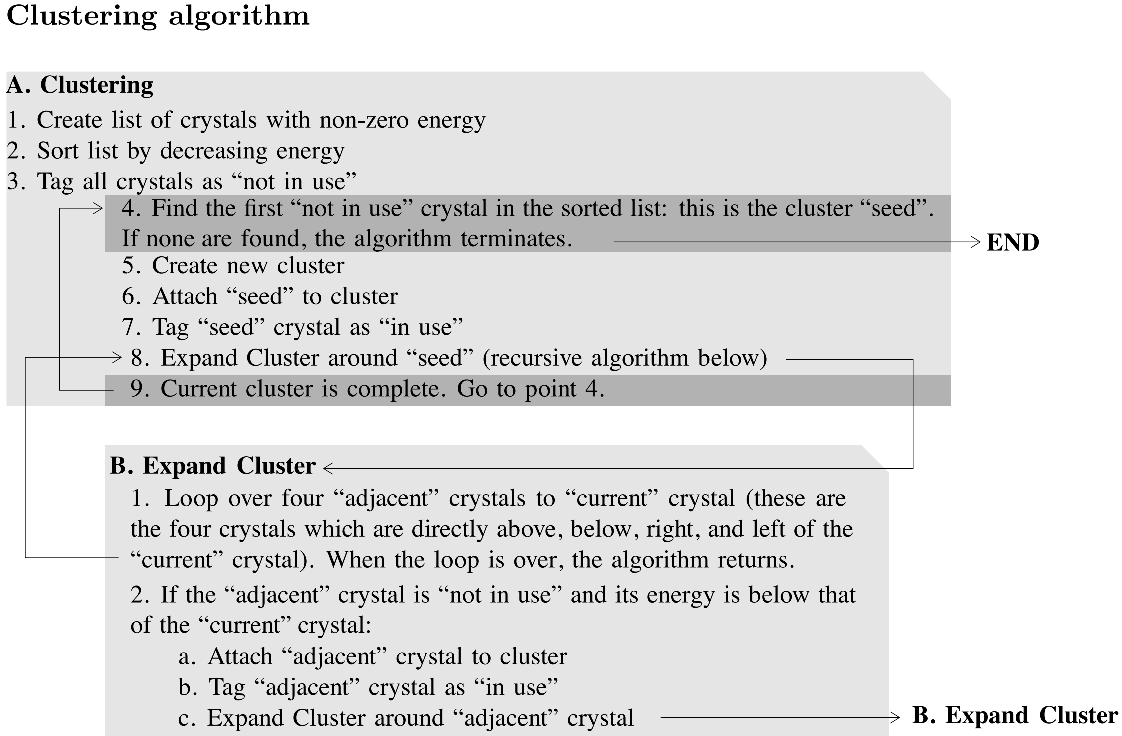

5.4.8 Calorimeter optimisation studies

In the hypothesis of collecting the necessary BGO crystals from L3 dismounted electromagnetic calorimeter, the PADME calorimeter size will not impact seriously on the experiment total cost if the number of readout channels is not substantially increased. To maintain the same number of readout channels and the same angular resolution it is sufficient to build a calorimeter with a larger radius placed at a greater distance from the target. The constraints imposed from the BTF hall suggest that the limit target to calorimeter distance will be ~ 4 m.

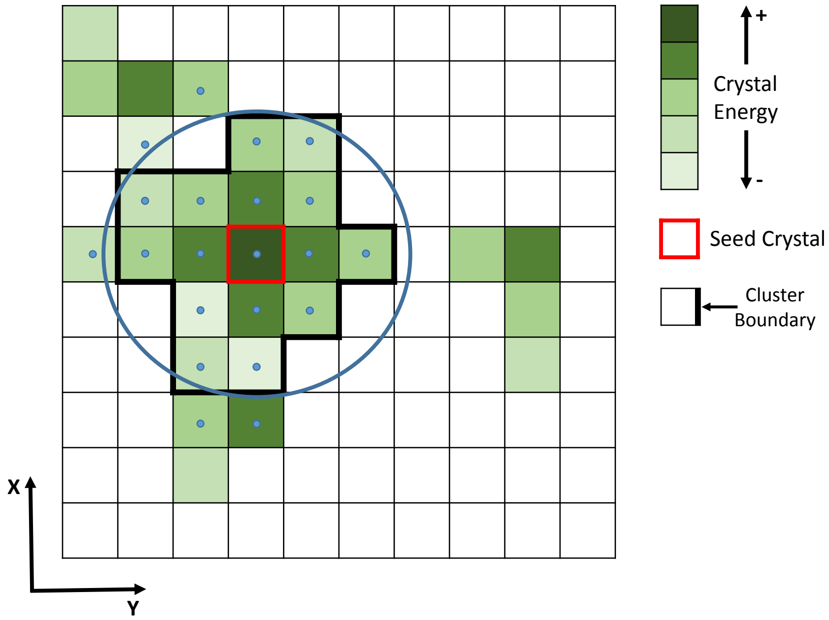

Figure 5.41: Graphical scheme of the PADME Box clustering algorithm (see text).

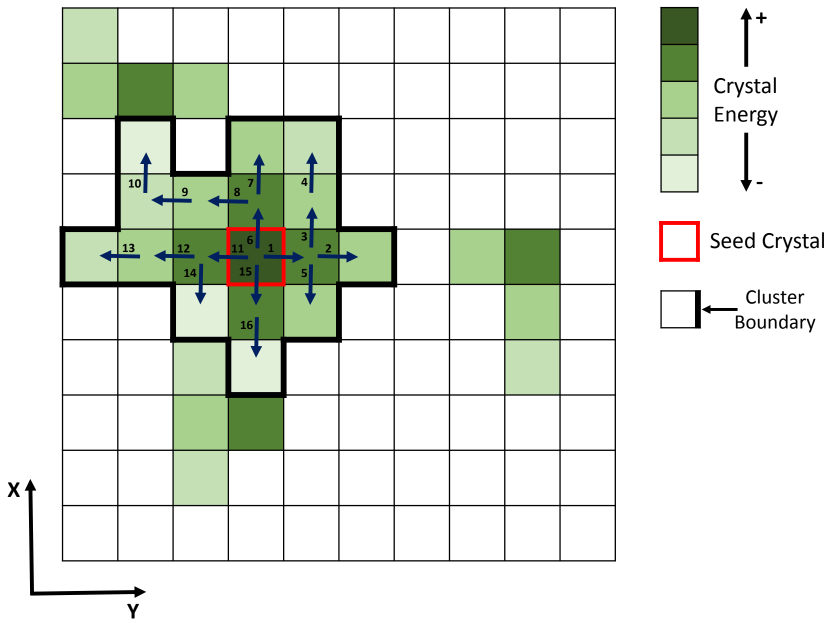

Figure 5.42: Graphical scheme of the PADME Island clustering algorithm (see text).

Having a larger and more distant calorimeter offers several advantages and no drawback, apart from the impact on the experiment costs. We use as a benchmark scenario a calorimeter with 656 crystals of $20 \times 20 \times 220\text{mm}^3$, placed at 4 m distance from the diamond target. The new calorimeter will have a radius of 300 mm with an internal hole of 80 mm radius. The advantages of such a solution can be easily summarized in the following paragraphs.

Larger crystals Having larger crystals offers more opportunities for photo-sensor choice, for example opening the possibility of using small photo-multipliers, otherwise impossible for the 10×10 mm^2 solution. Larger crystals also mean a factor four lower occupancy in the calorimeter for each photon shower, thus reducing the pile-up problem and allowing multi-cluster events to be treated properly. A lower number of crystals per single cluster also reduces calibration problems, thus improving single cluster resolution. It also implies a reduction in the data size. Moreover, this option greatly simplify the cutting and polishing of the original L3 BGO crystals, which is reduced to just modify the crystal shape from pyramidal to squared prisms, certainly reducing the risk of breaking or scratching the BGO, and maybe also reducing the cost. Another important point is that larger dimensions imply better mechanical properties and allow a more compact calorimeter, reducing dead spaces due to wrapping or paintings. Finally, the large backside area allows more available space for front-end electronics, simplifying its design, production and probably also the overall cost.

Larger calorimeter A larger calorimeter improves the (lateral) shower containment, thus improving the energy resolution on a wide range of angles, finally yielding a better missing mass determination. It also allow to gain acceptance at angles lower than 1°, by reducing the central calorimeter hole.

Larger distance A larger target-to-calorimeter distance improves the angular resolution even scaling the cell dimension accordingly. In fact we have observed in Monte Carlo simulations that the spatial resolution obtained with the 2 cm side version is better than what can be naively expected by scaling just by a factor two the resolution obtained with 1 cm side crystals. A larger distance also relaxes the requirement on the magnet bending strength, reduces the probability of showers from electron or positrons in the magnet iron (dangerous due to the possible energy leak in the calorimeter). Larger distance finally also improves the momentum separation of tracks after the dipole, thus improving the rejection of events with low-energy Bremsstrahlung photons.

Spatial resolution studies To assess the spatial resolution in the two configurations, we used the Monte Carlo to simulate a 500 MeV photon directed perpendicular to the front face of the calorimeter. In order to avoid energy leaks, the photon was pointed to a crystal located far from the edges of the calorimetr, i.e. with the center at $x = 0.5$ cm, $y = 9.5$ cm for 1 cm crystals and at $x = 1$ cm, $y = 19$ cm for 2 cm crystals. The cluster corresponding to the photon was reconstructed using the Box clustering algorithm, described in Sec. 5.4.7, with a radius of 4.5 cm and its center of mass was evaluated using the energy deposited in each crystal of the cluster. The distribution of the distance between the real impact point, i.e. the center of the crystal, and the position of the reconstructed center of mass was in both cases centered at $\sim$0 cm with a RMS of $\sim$0.2 cm.

The impact point of the photon was then moved along the X and Y directions in steps of 1 mm for 1 cm crystals and of 2 mm for 2 cm crystals. The mean and RMS of the reconstructed impact point for the different shifts are shown in Tab. 5.4. In both cases the effect of the shift is symmetrical between the two axes and its effect along an axis is independent from the shift along the other. The RMS tends to increase with the distance of the impact point from the center of the crystal and has a maximum when the photon impacts on the border between two crystals. Due to the higher energy deposit in the central crystal, the reconstructed position is not centered on the real impact point but is pulled towards the center of the crystal. This effect is particularly relevant for 2 cm crystals, where the portion of energy deposited in the central crystal is much larger than that in the neighbors.

1 cm crystals			**2 cm crystals**		
d	$\langle d_{exp} - d \rangle$	**RMS**	**d**	$\langle d_{exp} - d \rangle$	**RMS**
0.0	0.01	0.20	0.0	0.00	0.18
-0.1	0.05	0.21	-0.2	0.13	0.18
-0.2	0.09	0.21	-0.4	0.24	0.20
-0.3	0.11	0.22	-0.6	0.33	0.24
-0.4	0.12	0.24	-0.8	0.33	0.29
-0.5	0.06	0.27	-1.0	0.10	0.40

Table 5.4: Mean and RMS of the reconstructed impact point for a 500 MeV photon directed ortogonally to a crystal at different distances from the crystal center. All quantities are in cm.

Larger small angle calorimeter Also the small angle calorimeter, detecting photons in the hole of the main calorimeter, should be scaled according to its larger radius. The larger SAC dimensions will increase its rate capabilities due to lower crystals occupancy.

The impact of this new design on the PADME experiment total cost is under investigation. The three main item affected will be: calorimeter photo-sensors, total volume of SAC BaF2 crystals, experiment mechanics and vacuum. Concerning the calorimeter photo-sensors the modification will be to exchange the present choice the Hamamatsu S8664-55 APD with the model S8664-1010. The difference in price has been quoted by hamamatsu to be ∼150 €/channel. The difference in the SAC total amount of BaF_2 material will account for a 10 K€ cost difference. The cost increase due to the different mechanics and vacuum system is more difficult to evaluate; dedicated studies are ongoing.

The improvement in term of experiment sensitivity can be evaluated by checking the missing mass resolution of the system. In fact being the angular coverage of the new design identical and the longer decay region evacuated, we don't expect the background condition to change significantly. Therefore a better missing mass resolution will translate in a direct gain in term of background suppression. In Fig. 5.43 a scan in the missing mass resolution for different values of the target–calorimeter distance is presented for the two options: 10×10 mm^2 and 20×20 mm^2 crystals.

Using the same number of channels (656) the missing mass resolution is reduced from 24 MeV/c^2 at 2 m distance to 15 MeV/c^2 at 4 m, which could lead to a significant improvement in background rejection. This result has been obtained with a dark photon mass of 15 MeV/c^2, in order to understand if this improvement can effectively give a better sensitivity, we have evaluated the missing mass resolution on the entire range of dark photon masses, in the two hypotheses. As can be seen from Fig. 5.44, the difference in resolution gets smaller as the dark photon mass increases, since the recoiling photon will have less energy, and thus will be emitted at larger angles.

The PADME Monte Carlo has been upgraded to include the new layout, and a Monte Carlo production is ongoing to assess the new sensitivity with the full analysis.

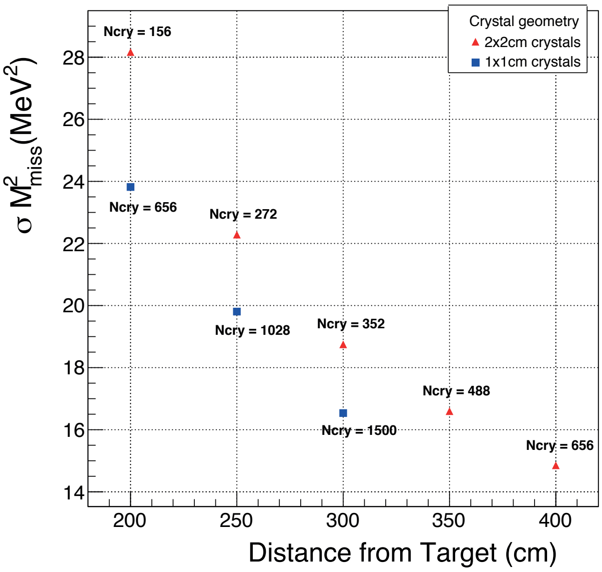

Figure 5.43: Missing mass resolution vs. calorimeter to target distance for different crystal size. Numbers indicate the total amount of crystal needed to keep constant acceptance.

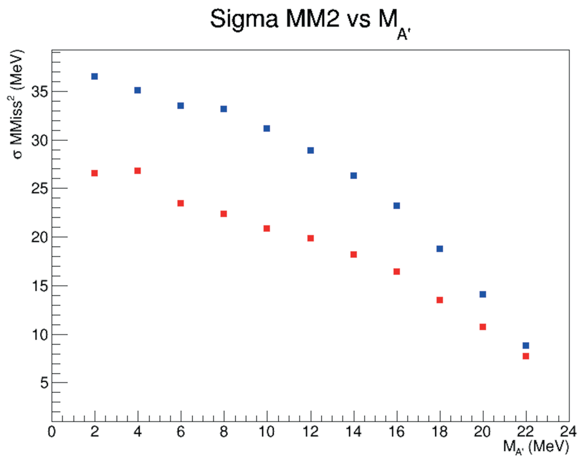

Figure 5.44: Missing mass resolution vs. dark photon mass for the two options of calorimeter to target distance (200 cm and 400 cm). The crystal size is consequently 10×10 mm^2 and 20×20 mm^2 to keep constant acceptance with the same number of channels.

Item	**Number**	**Unit cost (€)**	**Total cost (K€)**
Crystal cutting	170	300	**51**
Crystal wrapping	700	30	**21**
Mechanics			**50**
Photo-sensors	700	150	**100**
FEE and power supply	700	180	**128**
Total			**350**

Table 5.5: Summary table of the costs of PADME calorimeter by using the BGO crystals from the L3 experiment (VAT included).

5.4.9 Costs

In Tab. 5.5 we summarize the cost for the calorimeter up to the FEE electronics, VAT included.

The costs of the readout system, namely 22 V1742 boards, two A3818 optical receiver and two HP Proliant DL560 server, plus the needed MCX 8-channels coaxial cables kits, are listed in Tab. 5.6

Item	Number	Unit cost (K€)	Total cost (K€)
VME 6U Crate	2	6	**12**
V1742 Digitizer	22	10	**220**
A654 8-channels MCX cables	95	0.3	**29**
A3818C Optical receiver	2	3	**6**
HP Proliant DL560 custom	2	5.5	**11**
Total Readout			**278**

Table 5.6: Calorimeter DAQ cost estimate 22% V.A.T. included

5.5 Small angle calorimeter

The small angle calorimeter is a compact and fast inorganic crystal calorimeter covering the region of the PADME calorimeter inner hole. The aim of this detector is to veto photons at small angles: $\theta < 1°$. This is very important to reject backgrounds with multiple photons in the final state, namely $e^+e^- \rightarrow \gamma\gamma$ and $e^+e^- \rightarrow \gamma\gamma\gamma$. The layout of the small angle calorimeter is shown in Fig. 5.45, placed 50 cm downstream of the main calorimeter, as described in the previous sections (15 cm outer radius, 4 cm inner hole, 2 m distance from the target).

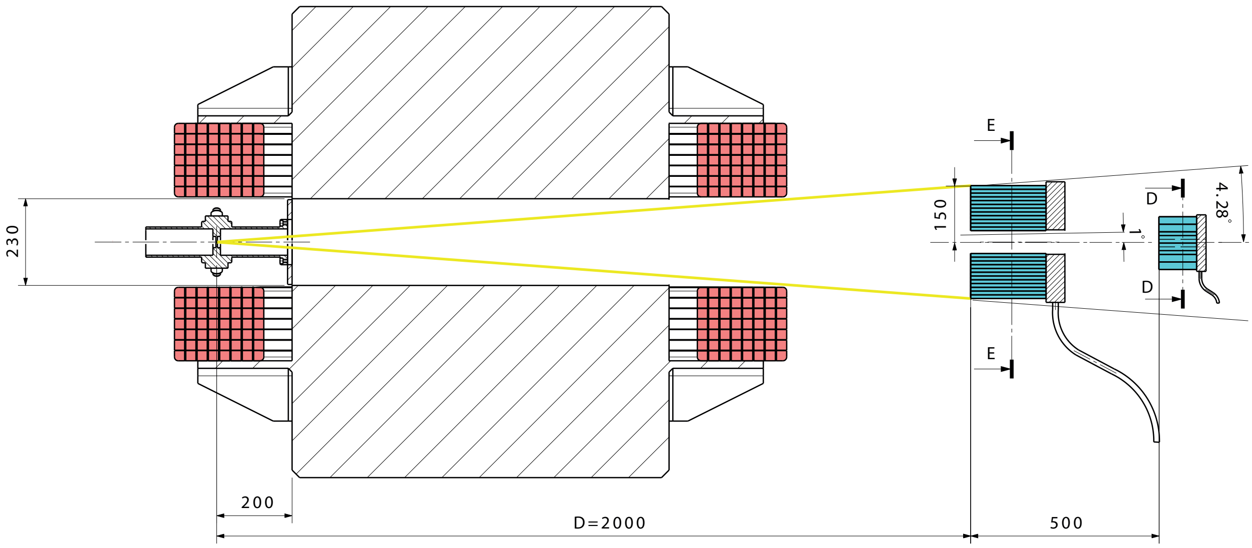

Figure 5.45: Layout of the small angle calorimeter, covering the main calorimeter hole acceptance.

Considering a granularity of 2×2 cm^2 (see below) and requiring at least an additional row of cells beyond the acceptance of the main calorimeter hole, the lateral dimensions of the small angle calorimeter is fixed to a 10×10 cm^2, plus two more crystals for each of the four sides. With this configuration, in the hyphotesis of removing or not reading out the innermost crystal, due to the very high Bremsstrahlung rate, this gives a practical modularity of 32 channels.

Due to the very long decay time of the BGO scintillation signal, the calorimeter cannot sustain the rate of Bremsstrahlung photons with a beam intensity of $5 \cdot 10^3$ positrons/bunch. For this reason the small angle calorimeter is designed for sustaining up to 10 clusters per bunch of 40 ns. Thus a crystal yielding an extremely short decay time signal is necessary, coupled to a fast photo-sensor. The current baseline solution is BaF_2. As shown in Fig. 5.24, the fast component decay time of scintillation from Barium Flouuride is as short as 1 ns. The slow component will not be a problem since the fast digitizers readout will allow distinguishing the fast component peaks at reconstruction level.

The optimal choice for the photo-sensors is the photo-multipier tube, since the response time of solid-state devices, like APD and SiPM, is way too slow. A possible solution is the Hamamatsu R9880-110 photo-multiplier: this extremely small, 10-dynodes PMT has only 16 mm diameter and a rise time of just 0.6 ns, allowing to fully exploit the good timing characteristics of the BaF_2. The size of the PMT impose the size of the crystals to be at least 20×20 mm^2.

Operating the readout board CAEN V1742 in the 5 GS/s mode, a very good timing and double pulse discrimination is possible. The 32 channels can be easily accomated in one readout board (or two, in case of 16-channels modularity).

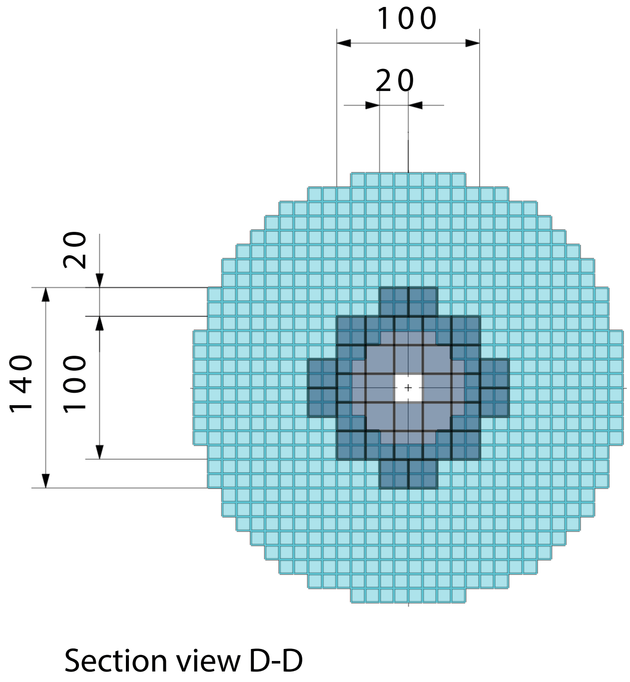

Figure 5.46: Layout of the small angle calorimeter crystals. The lighter shaded area represents the main calorimeter layout.

The present cost estimate is summarised in Tab. 5.7.

Item	Number	Unit cost	Total cost (K€)
BaF_2 crystals	32	12$/cm^3	**14**
PMT R9880-110	32	700 €/pc	**22**
High Voltage		5,000 €	**5**
Detector cost			**41**
V1742 Digitizer	1	10,000 €	**10**
A654 8-channels MCX cables	4	305 €	**1.2**
Total Readout			**11**
Total			**52**

Table 5.7: Preliminary SAC cost estimates.

5.6 Charged particles veto detectors

The main backgrounds, as described in the Monte Carlo and Sensitivity chapters, are the three photons process and the positron Bremsstrahlung. Whenever a positron of the beam interacts with the target radiating a photon (with an energy distribution $1/E_\gamma$), it will loose an energy E_γ, thus being more deflected inside the magnetic field region with respect to the nominal $E = E_0$ trajectory.

One handle for reducing this background is the hole in the calorimeter, removing from the acceptance a large fraction of those photons, due to the very peaked distribution of the Bremsstrahlung, and the use of the fast small angle calorimeter. However, detecting the positrons that have lost a significant amount of energy would allow more stringent cuts and further background suppression. Depending on the energy of the photon, the positron can be inside the magnet acceptance or, for softer photons, stay closer to the E_0 trajectory and go in the region outside.

In order to cover both regions, we foresee detectors both inside and outside the magnetic field:

- The first one will be placed along the side of the gap of the PADME magnet. By suitably segmenting this detector, we can have a rough measurement of the momentum of the positron from the position of the hit: we then call this device "positron spectrometer veto". Since a photon can also produce a e^+e^- pair, we will also instrument the magnet gap lateral surface on the side opposite with respect to the positron curvature. This symmetric detector will be the "electron spectrometer veto".

- For the higher energy positrons, escaping the acceptance of the spectrometer veto, we place an additional detector outside the magnet, covering smaller curvature radii (i.e. larger deflection angles).

We are planning to realize all these three detector elements with extruded scintillator bars with SiPM readout. We need approximately 250 cm of detector elements to cover the ≈ 1 m lenght sides of the magnet, plus the forward part for the higher energy positrons.

The detailed layout of the veto detectors will determine the detailed design of the vacuum vessel, in particular in the section inside the magnet gap. Trying to optimize the path for the positrons, avoiding grazing incidence angles on the walls of the vacuum pipe or in the transition regions, we are presently considering the layout shown in Fig. 5.47.

Electron and positron spectrometer veto On both sides of the beam line and of the vacuum vessel, two sets of scintillator bars, $10 \times 10 \times 180$ mm^3, will cover the length of the dipole, with the long side aligned to the magnetic field, in the vertical direction. The length is of course determined by the magnet gap: taking into account the readout (SiPM) and the cables, we need at least a couple of cm headroom. As described above, thanks to the magnetic field, the hit bars cluster will also provide information on the momentum (in addition to the charge sign) of the particles, thus allowing cuts on the estimated photon energy for Bremsstrahlung events.

In order to have a completely free flight-path for positrons of energy high enough (or close) for escaping the region inside the magnet poles, the vacuum vessel is shaped according to the curved path inside the magnetic field. The lower energy positrons will, instead, hit the first part of the veto scintillators inside the magnet gap, that will thus result shorter than the pole length (66 cm, as shown in the drawing). This is not necessary on the electron side, where the bars will cover the full length of 1 m.

High energy positron veto On the "positron" side of the setup, downstream of the magnet and on the side of the calorimeter, we plan to have an additional segmented detector, for those

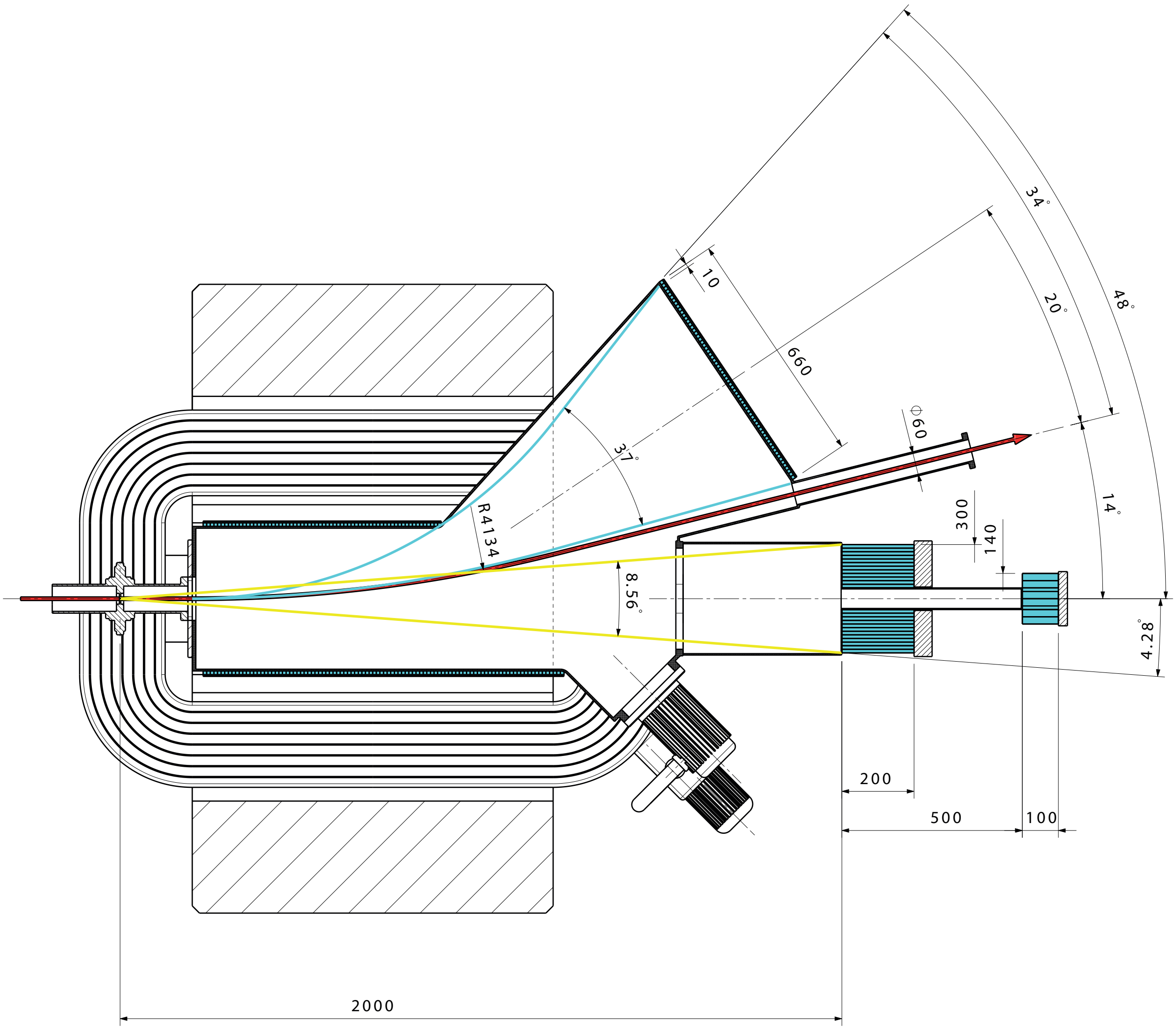

Figure 5.47: Positron veto detectors layout and vacuum vessel.

positrons that, emitting soft photons, escape the acceptance of the spectrometer veto detectors inside the magnet.

In order to cover a good momentum range, the instrumented region should arrive as close as possible to the beam, keeping at the same time the rate within a safe margin. The overall length will be determined by the distance of the instrumented plane. In the present configuration we plan to equip a lengh of about 70 cm, essentially ortogonal to the direction of the beam. For sake of simplicity, the long side of the scintillator bars can be realized of the same dimension as the ones of the spectrometer veto, always aligned vertically. This should be sufficient ($\approx$ 18 cm) since the vertical dimension of the beam will be millimetric and we expect dispersion due to the dipole only in the horizontal plane. This choice also simplifies the overall design of the mechanics supporting the scintillators and holding it close to the vacuum vessel.

In the baseline layout the scintillating bars and the relative readout is placed on the external lateral surface of the vacuum chamber. Due to the dimensions of the vacuum region, we expect the vessel to be at least 1 cm of Aluminum. With the chosen granulatity, we expect a point resolution of the order of 1 cm/$\sqrt{12}$, so that the contribution of multiple scattering will be small, even though not completely negligible. However, the most worrying aspect of placing those detectors outside the vacuum vessel is the probability of initiating a shower for the positrons in the range of energy from $E_0 = 650$ MeV down to few tens of MeV.

One alternative option to detectors placed outside the vessel, as shown in Fig. 5.48, is to arrange the scintillator bars inside the vacuum, on one side relaxing the requirement on the thickness of the vacuum chamber, on the other strongly reducing the probability of initiating an electromagnetic cascade. In Fig. 5.49 a first sketch of a "drawer" system for the precise insertion of the scintillating bars inside the vessel with the interface flange, is shown.

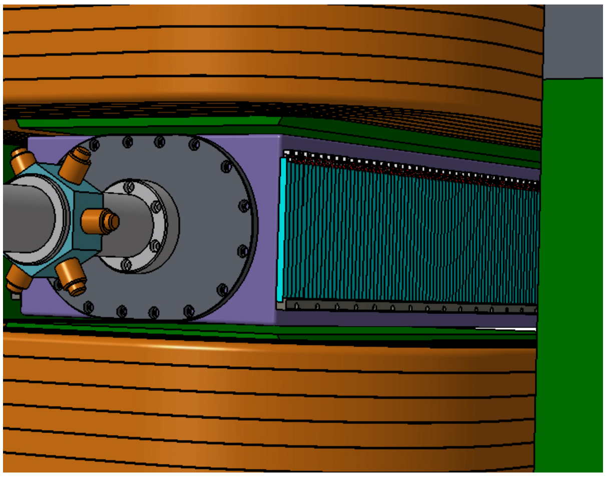

Figure 5.48: Sketch of the scintillating veto detectors placed on the external lateral surface of the vacuum vessel.

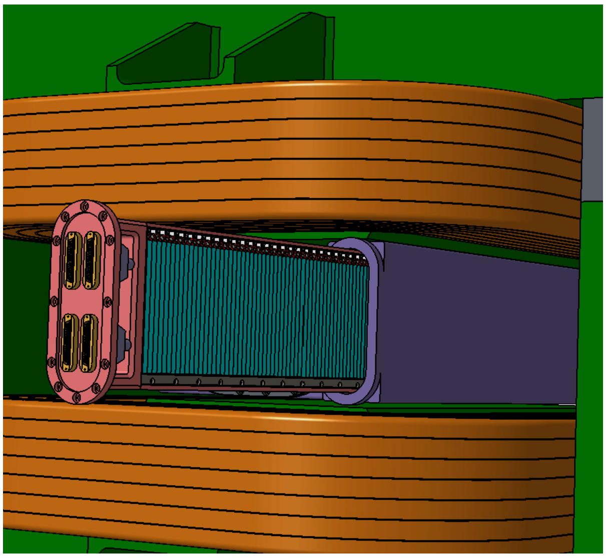

Figure 5.49: Sketch of the scintillating veto detectors integrated inside the vacuum vessel.

5.6.1 Photo-sensors

For the calorimeters we have considered Hamamatsu SiPMs (as described in Sec. 5.4.3), even though the baseline solution for the main calorimeter is now Hamamastsu S8664 APD, and small calorimeter small and fast photo-multiplier tubes. Instead, due to the short length of the bars (20 cm) and the small section (1×1 cm^2), a 3×3 mm^2 SiPM should be the optimal choice, both from the point of view of performance and cost.

As alternative to the Hamamatsu (in particular the S12572 shown in Fig. 5.35, we are now also evaluating several alternative on the market, with comparable characteristics, in order to make an optimal choice from the point of view of cost and performance, in particular in the following paragraphs we briefly describe sensors form FBK, Advansid, and SensL.

FBK

INFN has a long-established collaboration with the Bruno Kessler Foundation (FBK) at Trento for the development of advanced SiPMs, so that we may profit of all the studies performed by other INFN groups and collaborations. FBK has been developing in these years very interesting 3×3 and 6×6 mm^2 SiPM modules, both in the visible (RGB) and in the near ultraviolet (NUV) band, from 40 down to 20–15 μm (high density, HD) cell pitches, with fill factors (FF) $> 60\%$. Those devices can be operated up to ~ 10 V overvoltage (OV) over the typical breakdown.

The new NUV-HD SiPM by FBK [47] in particular offer very interesting performances for our goals : they combine the benefits of the HD technology (high FF and Photon Detection Efficiency (PDE), low correlated noise and high cell density) with the advantages of p-on-n approach for detection at short wavelength.

The small size of the cells used in the HD gives reduced gain, afterpulsing and cross talk; trenches between cells offer optical and electrical cell isolation; the new dead border reduction (< 2 μm) increase the FF.

The lower gain by the smaller cell size offer us also a larger dynamic range, a faster recharge time ($\sim$ 20–25 ns recharge time constant for 15 μm cell) and reduced pile-up, useful both coupling them to slow scintillators (BGO, CsI), as well as to fast ones (BaF_2), and plastic scintillators.

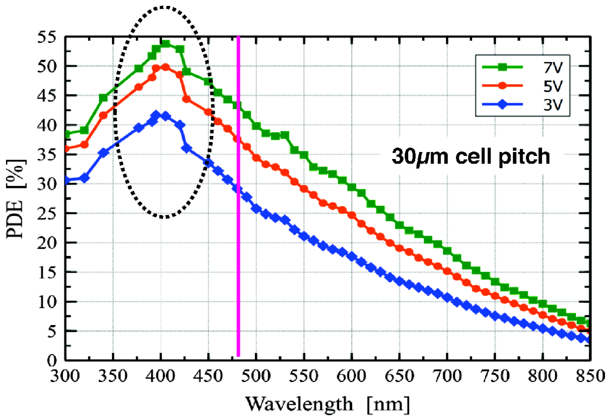

Figure 5.50: FBK NUV-HD efficiency vs. wavelength at different overvoltages (OV).

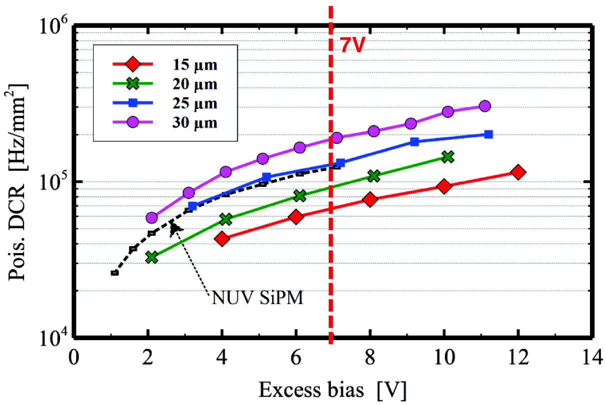

Figure 5.51: FBK NUV-HD dark count rate vs. overvoltage for different cell sizes.

Summarizing, the main characteristics of the new HD FBK modules are :

1. larger dynamic range and faster recharge time;
2. lower breakdown and operating voltage than Hamamatsu : $\sim$ 29 V at 2 V OV;
3. high PDE in the wavelength range of our interest: $\sim 30\%$, for cell size 20 μm and $\sim 40\%$ for 30 μm, at 5 V OV, as shown in Fig. 5.50 ;
4. very low dark count rate ($\sim$ 60 kHz/mm^2 at 5 V OV, temperature 20 °C, for 20 μm cell (see Fig. 5.51);
5. quite low temperature dependence of the breakdown voltage (typically $\sim$ 20–24 mV/°C) and of the gain;
6. signals shorter (O(50 ns)) than typical Hamamatsu SiPMs.

The high (naked chip) PDE also at short wavelength ($\sim$ 300 nm) is also interesting for the BaF_2 crystals that we are considering for the small angle calorimeter (see 5.5). For this application, specific studies for the development of a epoxy layer with sufficiently high trasmittance in the 300–320 nm band will be needed.

Advansid

Advansid (a spinoff company of FBK) has already commercially available two sensors that could be interesting for PADME: ASD-NUV3S-P (3×3 mm^2 and ASD-NUV4s-P (4×4 mm^2), both in SMD packages with protective epoxy layer already embedded and good performance [48].

The main characteristics of Advansid modules are :

1. lower breakdown and operating voltage than Hamamatsu : $\sim$ 29 V at 2 V overvoltage (OV);
2. PDE $>$ 30% at 480 nm, see fig 5.52 ;
3. very low dark count rate ($\sim$ 40 kHz/mm^2 at 2 V OV/20°C), see Fig. 5.53;
4. quite low temperature dependence of the breakdown voltage (26 mV/°C);
5. signals shorter (O(50 ns)) than typical Hamamatsu SiPMs.

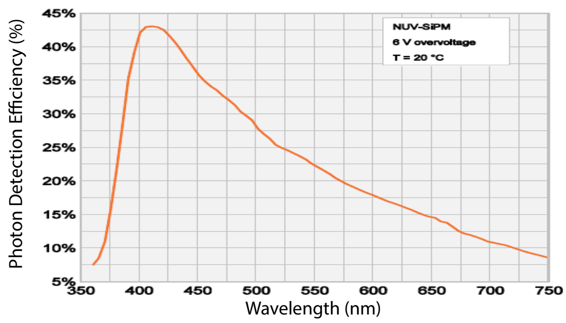

Figure 5.52: Advansid NUV efficiency vs. wavelength. SiPM chip already "dressed" with an epoxy resin layer, thus cutting the efficiency at the UV wavelength.

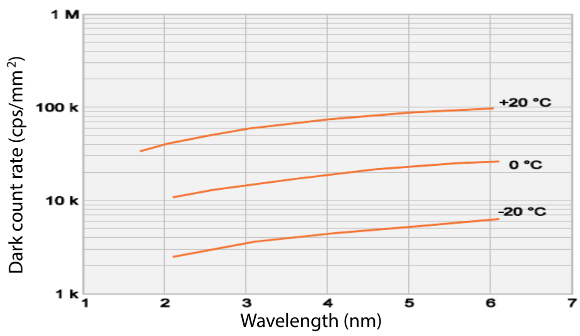

Figure 5.53: Advansid dark count rate vs. overvoltage.

Also in this case, dedicated development of high transmittance epoxy layer should improve the performance in the UV region.

SensL

SensL has recently developed two series of SiPMs available in SMD packages with protective expoxy layer already embedded: the Micro-C [50] and Micro-M series [50]. Both series have available 3×3 and 6×6 mm^2 modules in the near ultraviolet (NUV) range suitable for our goals.

The main characteristics of SensL modules are:

1. lower breakdown and operating voltage than Hamamatsu: $\sim$ 30 V at 2 V overvoltage (OV);
2. PDE $>$ 20% at 480 nm (see Figg. 5.54 and 5.55);
3. very low dark count rate ($\sim$ 20 kHz/mm^2 at 2 V OV and 20°C);
4. low temperature dependence of gain (-0.8%/°C) and breakdown voltage (21.5 mV at °C);
5. signals shorter than typical Hamamatsu SiPMs : O(100 ns).

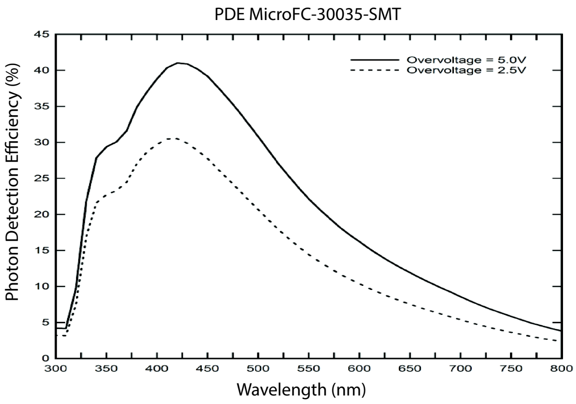

Figure 5.54: SensL-C NUV efficiency vs. wavelength.

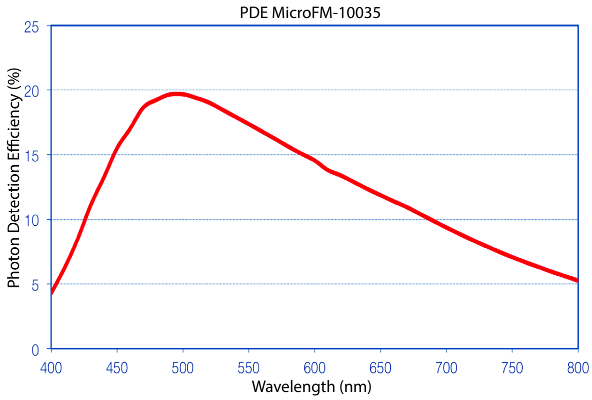

Figure 5.55: SensL-M NUV efficiency vs. wavelength.

A special characteristics of SensL modules is the possibilty to use the so-called "fast output" (a supplementary anode output separated from the standard one), giving a very short signal (~ 5 ns duration), in time with the standard signal output.

This characteristic is not necessarily useful for BGO crystals, which have a much longer response time, but may be very efficiently used with much faster crystals like LYSO or BaF_2 and with plastic scintillators. The PDE efficiency shown in fig 5.54 is calculated with the "dressed" detector after the epoxy layer deposition, which cuts its efficiency in the UV range, but still shows a $\sim 10\%$ efficiency at 320 nm

5.6.2 Front end electronics

5.6.3 Charged particle veto DAQ

Charged particle veto detectors will be readout with a common system simpler with respect to the V1742 digitizer boards, used in the calorimeters and for the active target, since they will just be used as veto detectors and we are not interested in a precise determination of the deposited energy. We will use commercial TDC boards in the VME bus standard, like the CAEN V1190A (128 channels). The board is based on the CERN HPTDC chip having a 100 ps least significant bit in the timing measurements. The boards will be operated in trigger matching mode so that, upon receiving a trigger from the trigger distribution system, all hits in a programmable time windows will be recorded and sent to the DAQ servers. The communication between the controller and the TDCs will make use of the VME bus, whose bandwidth is more than enough due to the 50Hz trigger rate provided by the BTF. The system will be housed in a 6U VME controlled by a CAEN V2718 optical crate controller, together with the SiPM power supply boards. The V2718 bridge is equipped with an optical link, with 80 MByte/s data transfer capability, which will be connected to one of the A3818 optical receiver in the DAQ Servers.

Considering the overall cost of the system, a possible option is to use exactly the same digitizing system as for the other main detectors (calorimeters, diamond target), thus avoiding discriminator boards, TDC and the VME-bus system. For the ~ 250 channels of the veto system, considering the baseline CAEN V1742 digitizing boards, we will need eight additional boards, for a cost of the same order of magnitude of the discriminators+TDC+VME sytem.

Item	Number	Cost (K€)
Scintillator	$250\times(1 \times 1 \times 18$ cm$^3)$	8
SiPM	250 + spares	6
FEE	250 channels	40
Discriminators	250 channels	50
TDC	3×128	18
VME controller	1	5
VME 6U crate	1	6
Total		**133**

Table 5.8: Summary table of the costs of PADME charged particle veto detectors, scintillator based.

5.6.4 Costs

In Tab. 5.8 the costs for the basic elements of these detector are, which amount to 83 K€ in total, but as for the other detectors in the following, in the final summary table we are splitting the "detector" costs – i.e. the materials, detector elements, structure, cables, high-voltages when required, up to the front-end electronics (included) – from the "TDAQ" costs, i.e. from the DAQ board to the acquisition computers, while the costs for event reconstruction and storage will be under "Computing". The reason for these subdivision is that we will try as much as possible to have a common acquisition and data handling infrastructure. Even in the case of the charged particles veto, that will be read differently from the main detectors (the calorimeters and the diamond target), the acquisition server will be one of the two devoted to the readout of the DRS4 digitizing boards, as well as the trigger distribution system. As already mentioned, an alternative option is to digitize also the analog signals from the veto system, thus replacing the cost of the discriminators, TDC, VME crate and controller, with eight additional CAEN V1742 boards, with approximately the same cost (80 K€).

5.7 Vacuum system

The PADME vacuum system is designed to keep the positron beam and all the secondary particles produced in the target in an evacuated region until the calorimeter region is reached. The vacuum vessel needs to be integrated with the magnet gap and with the positron and electron vetoes. The presence of the magnetic field coupled to the positron beam introduces a strong left right asymmetry in the distribution of tracks after the target. This reflects in an asymmetric design of the vacuum chamber which follows as much as possible the positron path in the magnetic field see Fig. 5.56.

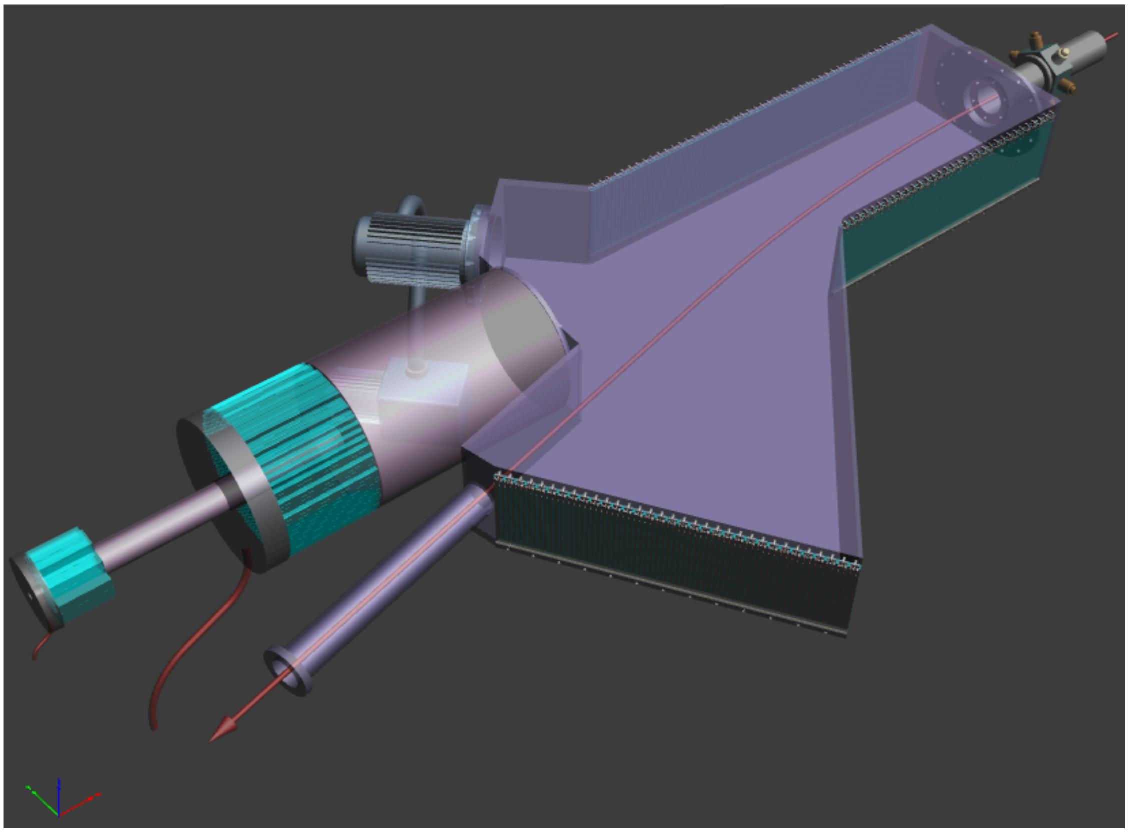

Figure 5.56: Preliminary layout of the PADME vacuum system magnet region.

5.7.1 The vacuum vessel

The PADME vacuum is divided in 3 logical regions:

- Target region: upstream of the PADME magnet
- Magnet region: from the beginning of the magnet up to the calorimeter region
- Dump region: downstream of the calorimeter where the exhausted beam is dumped.

The target region is integrated with the BTF beam line vacuum and has been already described. In the following, we concentrate out attention on the magnet region. The design of dump region is still not defined but is not expected to be problematic. The main chamber, in violet in Fig. 5.56, is a flat surface aluminum chamber of 200 mm height with a fan shape. It has one entrance flange connected to the target region and three exit flanges. The one to the right (beam view) is used to install the pumping system being on the electron side where no particles are expected.

In the middle section, a second flange is connected with the calorimeter vacuum tube having a diameter of 300 mm. A smaller pipe continues inside the ECal inner hole up to the small angle calorimeter front face. Both the pipes are closed with a thin window just in front of the calorimeters surface.

In the left side the third flange is connected to the pipe which brings the exhausted beam to the beam dump region. On the chamber walls the charged veto system is positioned. In this layout all the veto are outside the vacuum system but most probably it will be necessary to put part of them inside the vacuum vessel. The pressure inside the chamber will be of the order of 10^{-6} mbar therefore a 300 l/s turbo-molecular vacuum pump is expected to be enough to evacuate such a small vacuum region. Due to the higher pressure in the PADME vacuum region a decoupling with respect to the LINAC/BTF vacuum will be provided. Preliminary studies of the deformation of the chamber indicate that 1 mm Aluminum should be enough to sustain the atmospheric pressure.

5.7.2 Integration with the BTF vacuum system

The BTF line is operated at the LINAC transfer lines vacuum, namely down to 10^{-10} mbar. The vacuum breaks at the level of a 500 μm-thick Beryllium window, and the overall BTF vacuum is provided by 60–120 l/s ionic pumps. This configuration is mainly movitivated by the necessity of minimising multiple scattering and, at the same time, protecting the LINAC transfer line by possible failures in the BTF area. In order to reduce vacuum restoring time in a failure event, a fast and gate vacuum interlocking valve system is present. The vacuum gauge measuring system, the fast and the gating valves are controlled by the DAΦNE supervisor system.

The PADME experimental vacuum will be joined at the end of the pipe, with internal gating valves equipped with pre-vacuum service. The section end is equipped with a KF flange for pre-vacuum operations, an independent pressure gauge and a ionic pump.

5.8 Overall layout and mechanics

5.8.1 Baseline layout

The overall design of the PADME experiment is driven by the optimization of a number of parameters of the main detectors, with some strong contraint coming from practical arguments: the availability of the bending magnet, the number of available L3 BGO crystals, the maximum size that can be accomodated inside the BTF hall, etc.

Once having fixed some of the main parameters, such as the acceptance of the calorimeter, the distance from the target, the length of the magnetic field region, the strenght of the B field, we have optimized, as decribed in the previous sections, the other elements and detectors (dimensions, granularity, position, etc.). The resulting baseline layout of the experiment is shown in Figg. 5.57 and 5.58.

5.8.2 Alternative layout: larger calorimeter

As alternative to the basic layout, with a 30 cm diameter cylindrical calorimeter realized by 1×1 cm^2 BGO crystals and placed at $\sim$ 200 cm from the active target (see Sec. 5.8.1), we have discussed in Sec. 5.4.8 the option of having a calorimeter placed at a larger distance, with a larger diameter in order to cover the same acceptance.

The most practical solution is to go from 1 cm side to 2 cm side crystals, reshaping the trapezoidal prism L3 blocks to a square section. Having a doubled side allows to place the calorimeter at twice the distance, i.e. 400 cm, keeping the same acceptance and angular resolution, at the first order. Indeed, since the photon do not incide at 90° and the electromagnetic shower is shared differently among crystals (the Moliére radius is of course the same) the clustering, angular resolution and in turn the missing mass resolution do not scale linearly. In addition, the angular divergence of the beam will affect differently the resolution and the vetoing power in the two configurations.

Full simulations are needed in order to assess the final sensitivity for the different hypotheses of the dark photon mass in the two cases, and are currently under way. However, the possibility of changing the distance of the calorimeter, in case a larger number of L3 crystal will be available, seems to be useful, so that we are considering the possibility of changing the setup in the simplest and most efficient way. In Fig. 5.59 a preliminary design is shown, based on the concept that the vacuum vessel inside the magnet, the magnet and target assembly and the positron veto systems are not changed, while the calorimeter section of the vessel (and of course the calorimeter itself) are replaced with the larger ones.

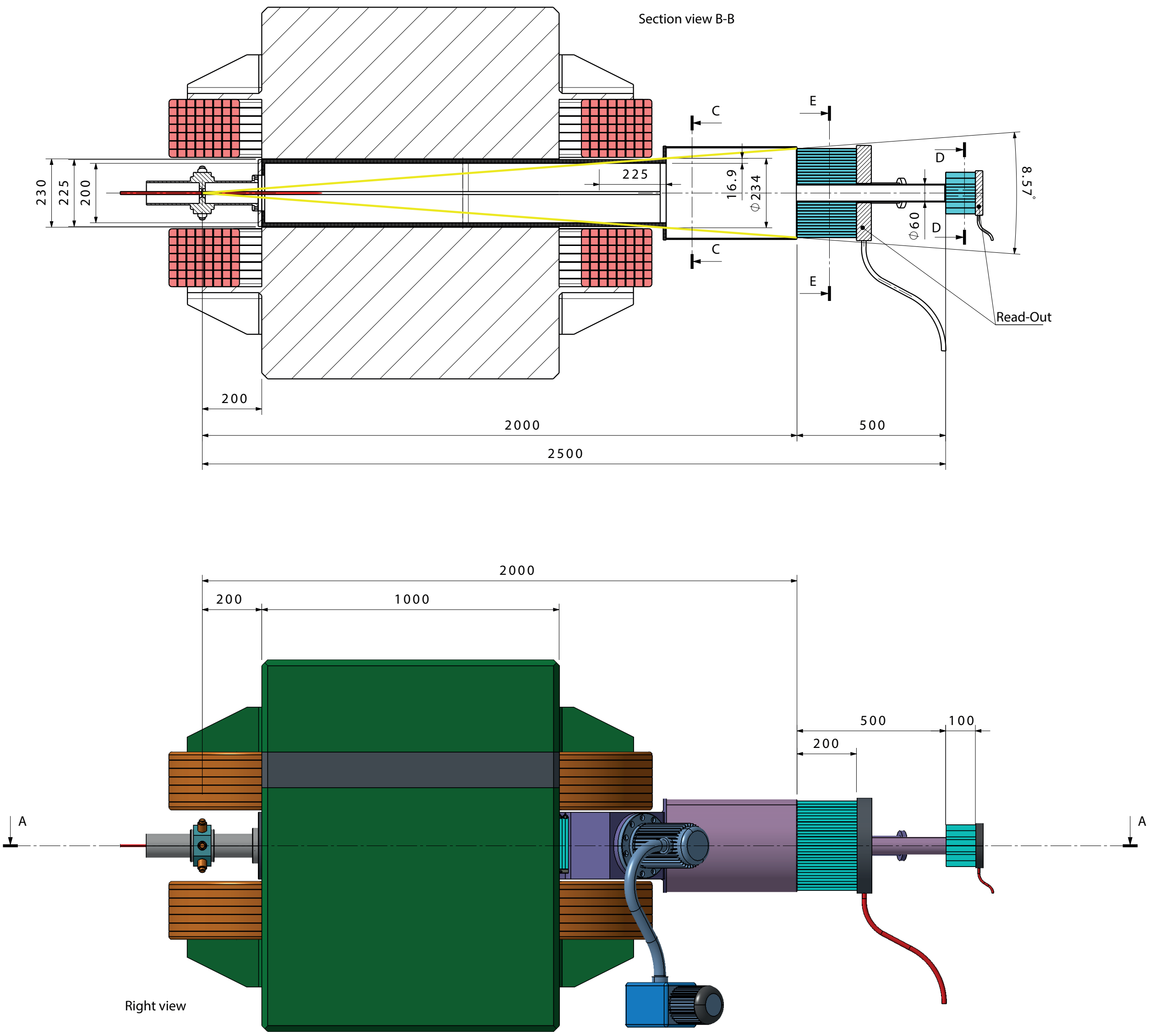

Figure 5.57: Preliminary baseline layout of the PADME experiment, including all the main elements (side view and rendering).

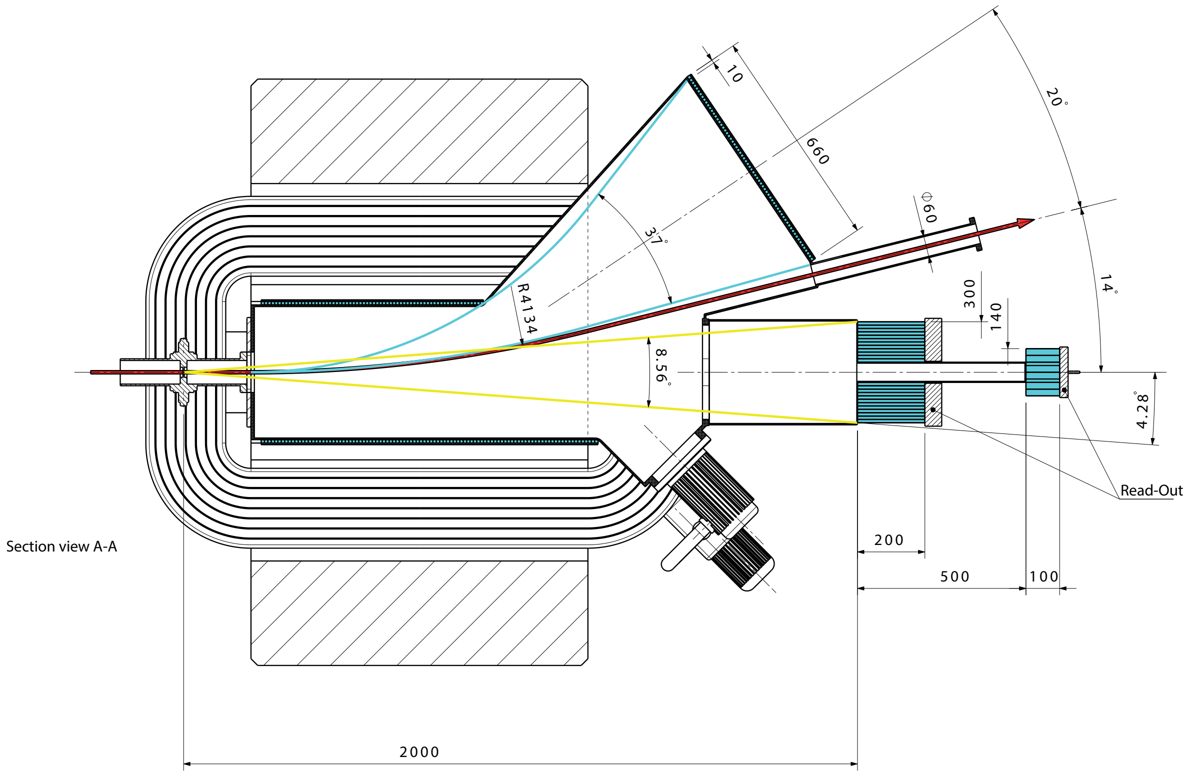

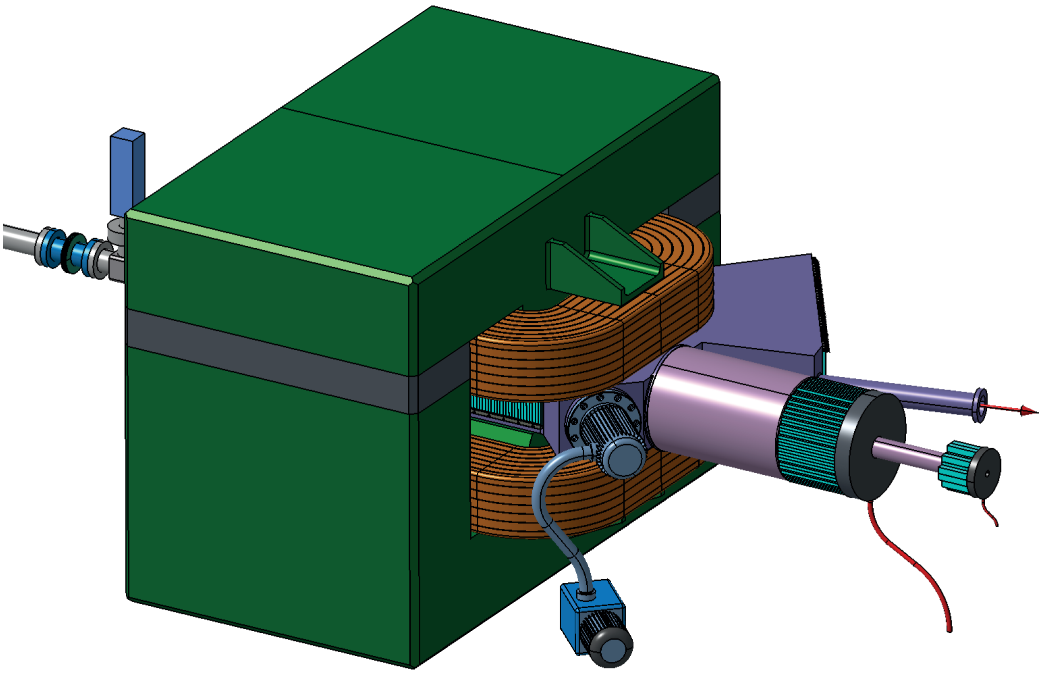

Figure 5.58: Preliminary baseline layout of the PADME experiment, including all the main elements (top view and 3D rendering).

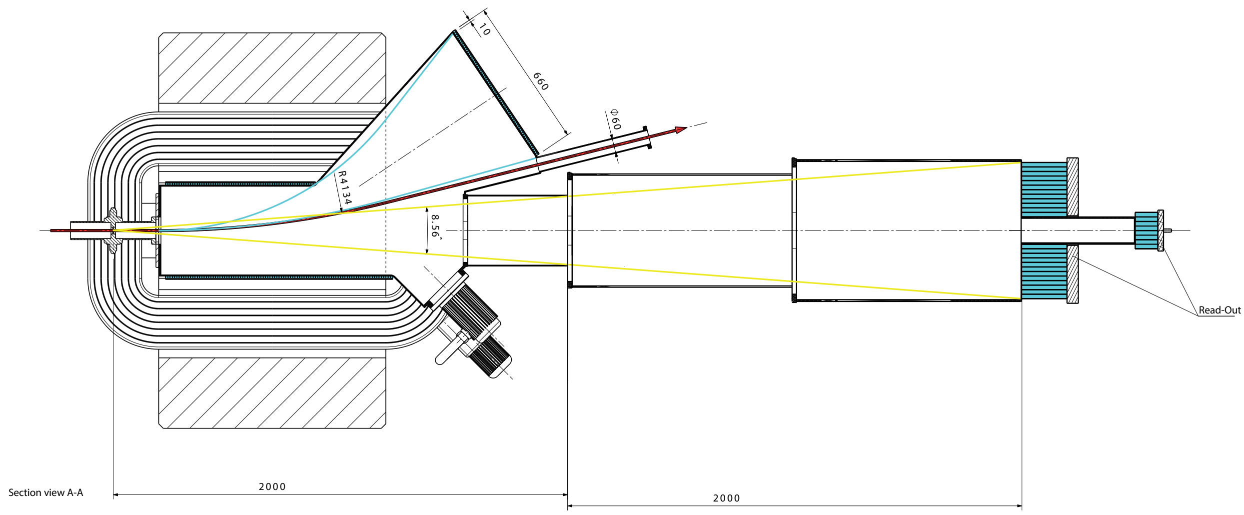

Figure 5.59: Alternative layout of the PADME experiment, with larger calorimeter (2×2 cm^2 granularity), 4 m distance from target (top view).

Chapter 6

The PADME trigger and data acquisition system

The trigger and DAQ of the PADME experiment is relatively simple due to the moderate amount of channels and the relatively low trigger rate (maximum 50 Hz) given by the beam bunches. Nonetheless, the $\sim$ 700 flash analogue to digital converter (FADC) channels used in the PADME readout require some early data reduction to avoid writing huge amount of useless FADC samples. Due to the extremely thin target just in 10% of the cases a calorimeter cluster is observed, and even in this case just a few crystals ($\sim$ 20) will have a significant energy deposit. PADME trigger system has to perform channels zero suppression and event selection at different levels to reduce the raw data size by a factor of $\sim$50 or higher.

Two different types of data will be managed: FADC data coming from V1742 boards installed on the active target and calorimeters readout, and the time to digital converter (TDC) data coming from digitized signals of the veto systems. The present description is based on the data formats of the V1742 boards and the readout test performed in the laboratory with already purchased cards.

The trigger system of the PADME experiment is based on a triggerless decision at level 0. After receiving the 50 Hz NIM digital trigger signal from the DAΦNE linac (LINAC-SYS), which is related with the time of arrival of particles in the BTF line (with an adjustable delay or even advance, see next section), all the FADC readout boards start to digitize 1μs of signals and to send their data to the front end PC's through direct optical links. TDC boards on the veto detectors will match triggers in the internal buffers to the L0 PC's via VME links. The timing of the distributed trigger signal is crucial to allow better than 0.2 ns synchronisation of all readout boards providing the necessary timing to the veto detectors.

6.1 BTF beam trigger

The linac gun pulser electronics drives the square waveform supplied to the gun for the emission of primary electrons (see Sec. 4), and also generates the master clock of the DAΦNE accelerator complex, to which the RF system and all timing references of the DAΦNE accelerator are locked. A reference signal is provided to the BTF through a digital delay generator, that allows proving a trigger signal of adjustable width and standard (TTL or NIM) with an arbitrary delay with respect of the arrival of electrons in the BTF hall in steps of 1 ns, from $\approx -14\mu$s (in advance with respect to the particles) on. The jitter of the digital delay generators used in the system is of 50 ps, so that a very precise and stable reference is provided with respect to the time of arrival of electrons.

6.2 L0 trigger

The level 0 trigger is constituted by two parts: the L0 Trigger Distribution boards and the software L0 trigger algorithm. The L0 Trigger Distributor board receives the trigger signals from the beam and from the calibration systems, then performs the logical OR and produces several synchronous copies in output. Given the number of expected readout boards (23 FACD + 3 TDCs) $\sim$ 50 channels of synchronised triggers are necessary. These trigger lines are distributed to FADCs and TDCs through equal length LEMO-00 coaxial cables.

When a trigger is received from the L0 Trigger Distribution system, the L0 DAQ system will read all available information stored in the DAQ boards internal buffers. The L0 DAQ system software will consists in several independent processes, one per readout board, running on the front-end servers and coordinated by a Central DAQ Manager.

Data from the CAEN V1742 ADC boards will be processed by the L0 DAQ system. The system will apply the correction procedures provided by the manufacturer, followed by a zero-suppression algorithm. At this stage further data reduction algorithms (delta compression, Huffmann, etc.) can be applied if required and if compatible with the time constraints. Data from each individual board will then be written to a temporary disk buffer as independent files.

6.2.1 L0 trigger zero suppression algorithm

The L0 zero suppression algorithm aims at reducing the event data size by suppressing any digitized stream from the calorimeter not containing real energy deposits. Indeed, independently from the presence of any energy deposit, each of the calorimeter crystals will generate 1024 samples of 12 bits on each L0 trigger received from the beam. This data will be sent to the L0 servers, for a total of $\sim$ 1 MByte per event.

This is the dominant contribution to the event size, being $\sim$ six times larger with respect to the sum of the rest of the detectors. Yet, even in presence of a cluster in the calorimeter, only $\sim$ 25 of the 656 crystals have a significant energy deposit and therefore their signals contain useful information. For this reason a data size reduction factor > 20 can be obtained without any information loss.

Thus a zero suppression algorithm has been developed and tested on data for the PADME L0 trigger. The basic idea comes from the shape of the calorimeter signal. Being the rise time of the BGO signal slow (10 ns) compared with the digitization frequency (1 GHz) for a physics signal many adjacent points over the noise threshold are expected. The L0 trigger algorithm works as follows:

- For each signal (1024 samples) the first 80 samples are used to compute the noise RMS value after applying vendor calibration and corrections. This is a safe choice because the trigger is configured to arrive 100 ns earlier than the signal itself.

- After computing the noise RMS (σ_N, which is $\sim$ 1 mV for the original BGO crystals read by small photo-multipliers with $\approx 10^6$ gain), the algorithm scans the 1024 points counting the number of consecutive points with a value greater than n times σ_N. The result of the analysis of random triggered crystals exposed to cosmic rays is shown in Fig. 6.1 left.

- Asking for 4 consecutive points with an amplitude $> 3\sigma_N$ produces a rejection factor on noise-only spectra of 15000 (only the 0.01% of the noise passes the zero suppression). In addition, among the L0 triggered noise events there are pulses produced by cosmic rays, hence real pulses, as suggested by the presence of events with 7 samples over $5\sigma_N$.

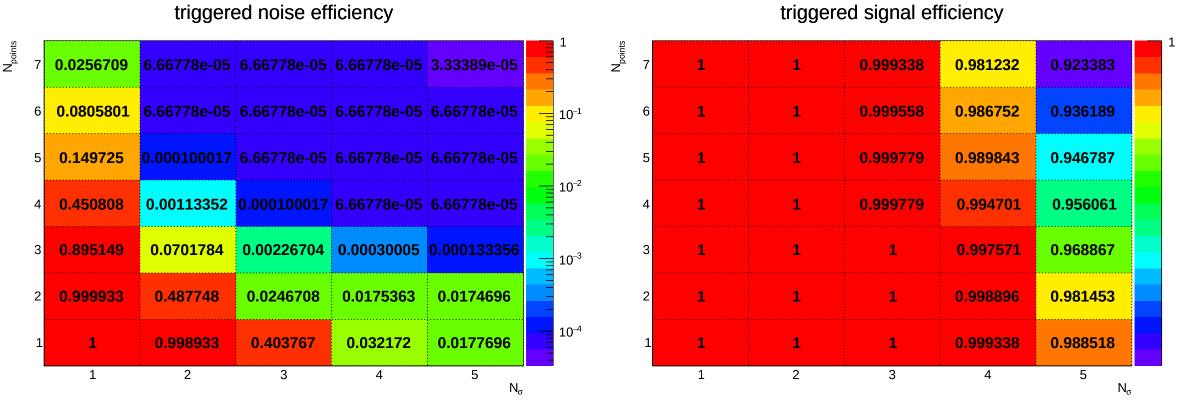

Figure 6.1: L0 trigger efficiency on noise (left) and on signal (right). The choice of four samples over $3\sigma_N$ presents a very good signal efficiency together with a very low noise acceptance. The plateau value in the noise graph is probably due to the presence of real pulses produced by cosmic rays.

Studies on electromagnetic showers from the first beam-test at BTF show an efficiency for the signal $> 99.9\%$ as shown in Fig. 6.1 right. Anyway it is important to underline that the efficiency depends also on the events energy: higher the energy, higher the efficiency.

The L0 trigger algorithm has already been implemented into the PADME DAQ system and tested during data taking. The CPU time required by the algorithm has been found to be sub-dominant with respect to vendor calibrations and corrections. If the L0 trigger decision is negative, no samples for that channels are written to the temporary files. If in an event all the channels of a single board are suppressed, only the event header, described in Fig. 7.1, will be written to the output file. If any number of channels survives the L0 zero suppression, all the samples of the corresponding trigger channels are also saved. For monitoring purposes and to allow for efficiency studies, $\mathcal{O}(1\%)$ of the data will be stored without L0 zero suppression (auto-pass events).

6.3 L1 trigger

The PADME L1 trigger is entirely implemented in software and runs on the same machines used for the L0 software part. The aim of the L1 trigger is to perform further data reduction and an event-based selection.

A set of L1 processes will read data from the files corresponding to the same set of events, and will perform the event building, as well as an initial reconstruction and filtering of the events.

After the zero suppression an important fraction (10% to 50%) of the calorimeter data will come from the digitized trigger signal. To further reduce the data size, the L1 will fit the trigger signal to extract a 32 bit trigger fine time, to be used in the board-to-board synchronisation process.

An initial (coarse) reconstruction will then be performed on the full event and a set of physics-oriented filters will be applied to the data. Currently two filters are foreseen: one dedicated to the invisible decays, characterized by the presence of one or more ECAL clusters, and one to the visible decays, characterized by two or more tracks in the spectrometer veto system.

At the end of the L1 stage, the event will be written to file in RAW format. This data format will consist of all the ADC and TDC samples read from the online electronics and will include and will include the results of the filters and information about the trigger source (beam or calibration).

In the initial phase of the exeperiment, the L1 trigger will function in flagging mode and all events will be written to the output files, irrespective of the result of the physics-oriented filters. In a second phase, if data storage considerations require it, L1 can be switched to rejection mode so that only events passing one or more of the filters will be written to the output files.

Fig. 6.2 shows the DAQ data processing model scheme.

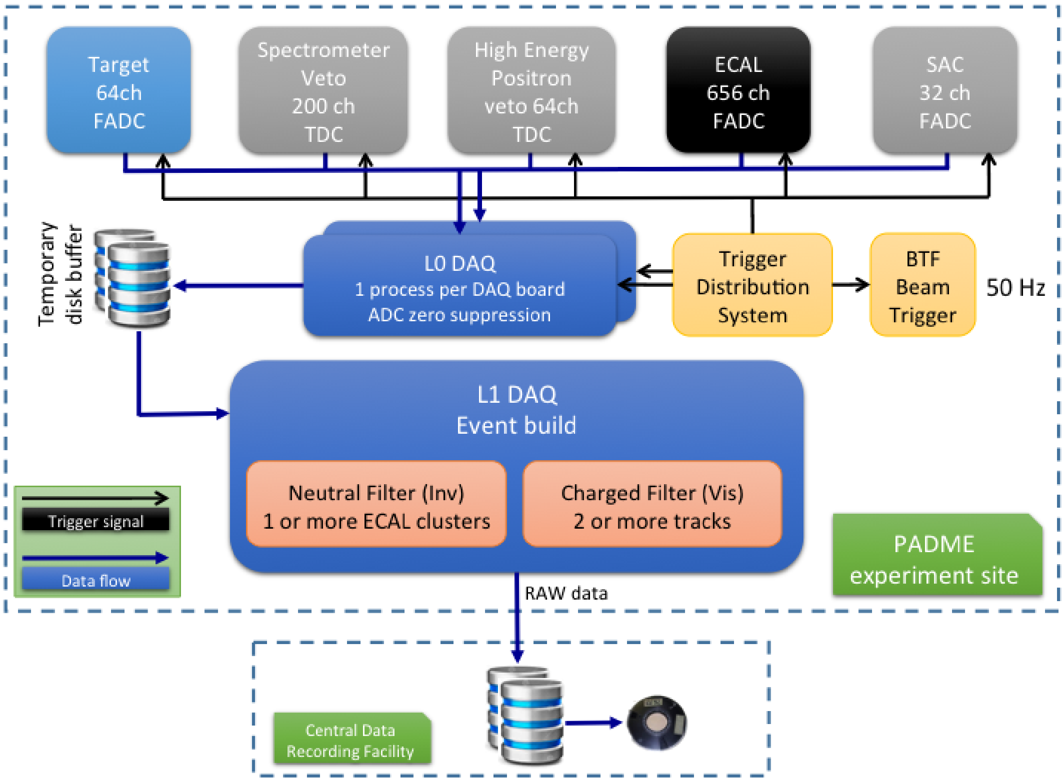

Figure 6.2: Graphical representation of the PADME DAQ model.

Chapter 7

PADME computing model

7.1 Data Processing model

The data processing model is strongly connected with the DAQ structure described in the previous sections. The flow of data within the online DAQ system can be summarized as follows: readout boards will send their data to the L0 readout PC which will write the data in temporary files after applying corrections and zero suppression. L1 processes will collect the data from single files and build the event producing the RAW data stream, which still includes all samples from the digitizers. L1 will also apply event filters and tag each event for acceptance or rejection, as described in section 6.3. RAW events written by L1 will be fully reconstructed and the obtained quantities written to disk using the RECO format.

7.2 Event Data model

The Event Data model defines the data formats used by the experiment. At the present stage, 4 data formats are foreseen: RAW, RECO, SIMU, and THIN.

7.2.1 The RAW data format

The RAW data format will be written during the L1 step after the event build and will include all information directly read from the ADC boards after the application of the zero-suppression algorithm and all information from the TDC boards. A preliminary file format, shown in Fig. 7.1, is already defined and is being used for the calorimeter DAQ of the ongoing test beams.

At this point, the size of the ADC sample is 16 bits instead of the V1742 native 12 bits due to the effect of the sample correction algorithm applied by the CAEN libraries. The final RAW file data structure will be an evolution of the structure currently used for the events acquired during the test beam, possibly inserted into a ROOT file.

7.2.2 The RECO data format

The RECO data format will include information about each channel passing the zero-suppression algorithm and all information related to high level physics entities, such as tracks and clusters. The channel related information will not include the full set of ADC/TDC samples but only reconstructed quantities, including (but not limited to) total charge collected, raw and calibrated energies, and timing information.

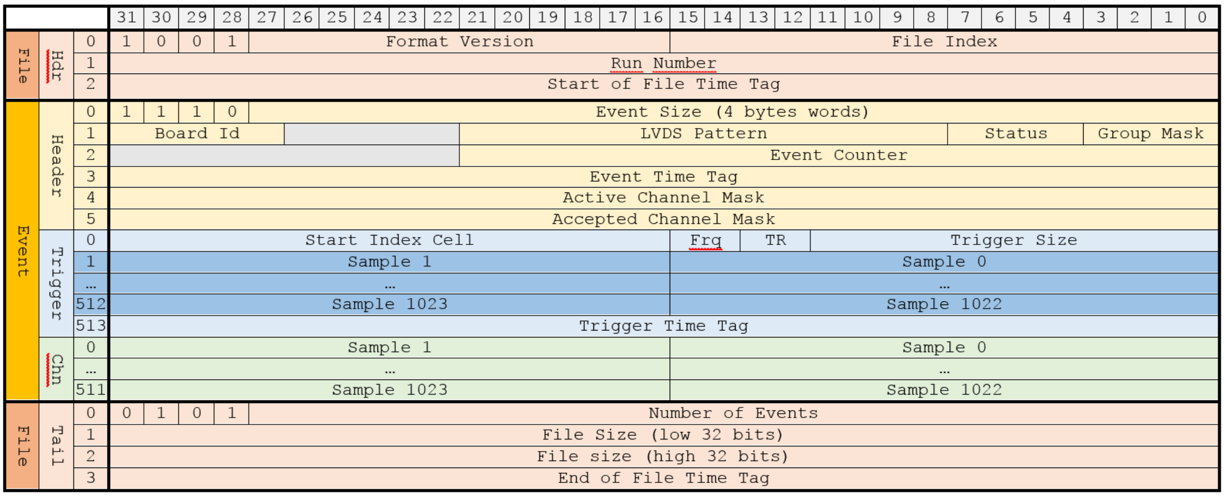

Figure 7.1: RAW event data structure

File Header
- Initial pattern: 1001 (0x9)
- Format Version: progressive number which identifies the version of the data structure in the file
- File Index: progressive index of the file within the run (start at 0, max 65535)
- Run Number: progressive index of run (unsigned int)
- Start of File Time Tag: time in seconds from the epoch when the file was opened

File Tail
- Initial pattern: 0101 (0x5)
- Number of Events: total number of events written to file (unsigned int)
- File Size (low+high): total size of file in bytes (unsigned long)
- End of File Time Tag: time in seconds from the epoch when the file was closed

Event Structure (repeated for each event in file)

Event Header
- Initial pattern: 1110 (0xE)
- Event Size: total size of current event data structure in words of 4 bytes each
- Board Id: identifier of the CAEN digitizer board (0-31)
- LVDS Pattern: bit pattern latched on the V1742 LVDS I/O when trigger arrives
- Status: event status (0: accepted, 1: rejected,)
- Group Mask: 4 bit mask with map of active groups
- Event Counter: progressive number of event (number of triggers) within the run
- Event Time Tag: time of event since last reset (counter incremented at each sampling clock hit)
- Active Channel Mask: 32 bit mask with map of active channels
- Accepted Channel Mask: 32 bit mask with map of accepted channels

Event Trigger (repeated for each active group in Group Mask)
- Start Index Cell: reference cell for data correction
- Frq: frequency at which data was sampled (00: 5GHz, 01: 2.5GHz, 10: 1GHz, 11: not used)
- TR: trigger signal was (01) or was not (00) sampled and written to readout
- Trigger Size: size of current trigger structure in words of 4 bytes each
- Sample n: value of sample n of current trigger (short). Present only if TR=01
- Trigger Time Tag: trigger arrival time since last reset (counter incremented every 8.5ns)

Event Channel (repeated for each channel in Accepted Channel Mask)
- Sample n: value of sample n of current channel (short)

This format will be written to file using the ROOT package and will be used for most data analysis.

7.2.3 The SIMU data format

The SIMU data format will include all information produced by the GEANT4-based Monte Carlo simulation of the experiment. SIMU files will be written using the ROOT package.

7.2.4 The THIN data format

The THIN format will be mostly used for analysis on personal computers and will only include information about high level physics entities such as clusters and tracks. THIN files will be written using the ROOT package.

7.2.5 Other data formats

In addition to the main data formats used for reconstruction and analysis, we can envisage a whole set of data formats used for specific tasks. Some examples can be:

- Calibration: special files, possibly using an extension of the RAW data format, used for detector-specific calibration tasks.
- Condition: data related to conditions of the detector during the run as acquired by the Detector Control System (DCS).
- Configuration: information related to the configuration of each run, including beam conditions, detector configuration, etc.
- Constants: sets of calibration constants obtained trough a detector calibration process and used in the reconstruction.

Given the specific nature and use pattern of the Condition, Configuration, and Constants data, storing these formats into a database will simplify the access to the information and optimize the retrieval time.

7.3 The Event Reconstruction model

The PADME Event Reconstruction process will follow the standard HEP model and is represented in Fig. 7.2

Data collected from the experiment by the TDAQ process will be written to disk in RAW format and then reconstructed. The reconstruction process will write the RECO and THIN selected streams, which will then be available for analysis.

The TDAQ process will also:

- create the Calibration data files which will be used by the Calibration process to produce the detector calibration constants: these will be written to the central DB and used in the Reconstruction process.
- record the Run Configuration data in the central DB for future use in the Reconstruction process.

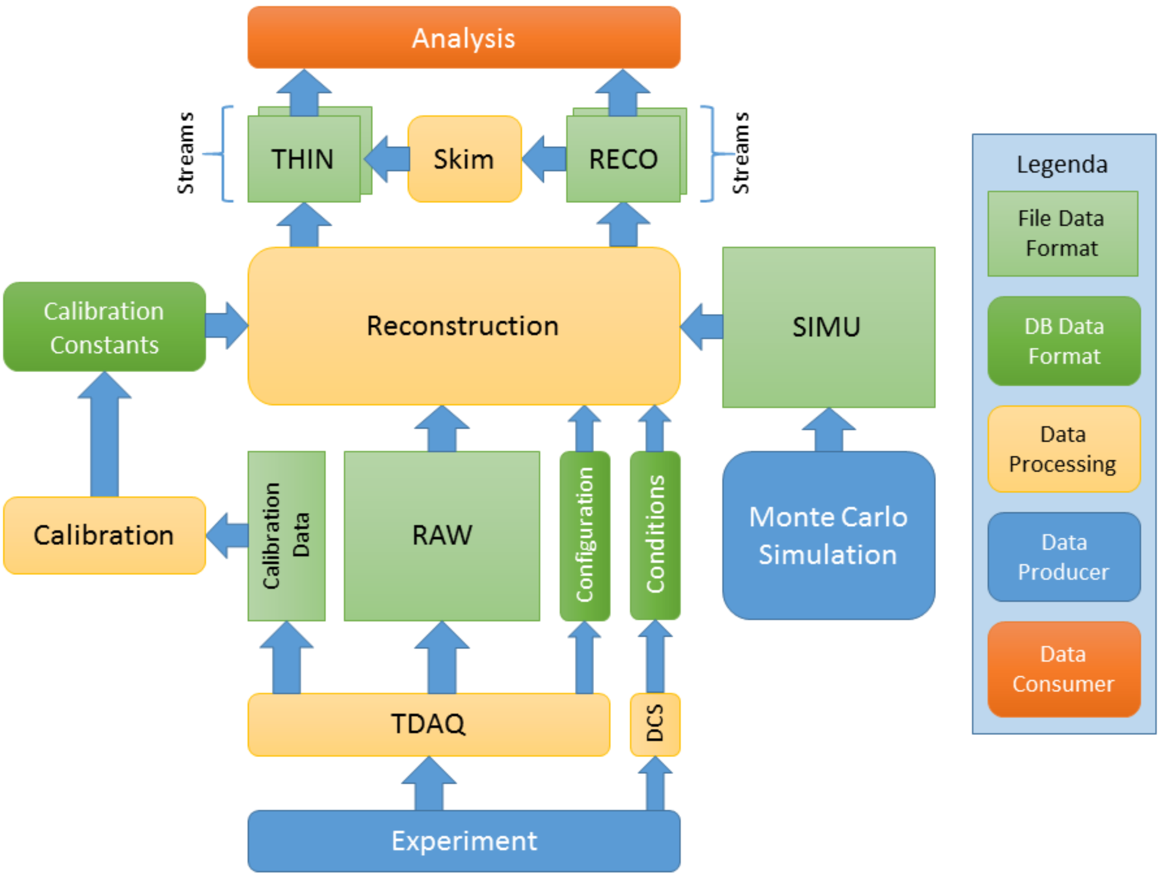

Figure 7.2: The PADME Event Reconstruction model

The Detector Control System (DCS) will collect all Condition data and write them to the central DB for use in the Reconstruction process.

In parallel, all data produced by the GEANT4 simulation will be written to SIMU files, reconstructed, and finally written to RECO and THIN files.

At any time, THIN format events can be produced from the RECO files via a Skim process.

7.4 Event size and rates

For each channel of the CAEN V1742 board, the DSR4 ADC will produce 1024 12bit samples per trigger, corresponding to 1536 bytes of data. In addition, the trigger information for each channel group of the V7142 board will also be digitized, thus contributing with 1536x4=6144 bytes per board per trigger. In total, each 32 channels board will produce 55344 bytes of data per trigger, including 48 bytes for event/group headers.

The amount of data produced by the TDC boards depends on the channel occupancy: each TDC hit within the time window associated with a trigger will contribute with a 32 bit word containing channel id and time information. In the following we assume a conservative average occupancy of 1 hit per channel per trigger for both the High Energy Positron Veto and the Spectrometer Veto.

Given the number of channels, summarized in Tab. 7.1 together with the contributions from each sub-detector, and the 50Hz rate of the BTF beam, a preliminary estimate of the the total data rate in input to the DAQ system is of ~ 63 MiB/s, largely dominated by the electromagnetic calorimeter.

Sub-detector	**Readout type**	**N. of channels**	**Channels per board**	**N. of boards**	**Data rate (MiB/s)**
Active target	ADC	30	32	1	2.64
Calorimeter	ADC	656	32	22	58.06
SAC	ADC	32	32	1	2.64
Spectrometer	TDC	200	128	2	0.04
Positron veto	TDC	50	64	1	0.01
Total		**968**		**27**	**63.38**

Table 7.1: Estimated total DAQ rate with contributions from each sub-detector.

During the L0 phase, a zero suppression algorithm is applied to each ADC channel, substantially reducing the amount of data written by the L0 DAQ process to the temporary disk buffer. Using the projected occupancies obtained from Monte Carlo studies, we can estimate the total amount of RAW data collected in a year of data taking in ~ 89 TB, as detailed in Tab. 7.2. This estimate assumes that a year of data taking corresponds to 365 useful days and does not take into account possible *ad hoc* data compression algorithms (delta compression, Huffman, etc.) and/or the data compression algorithm natively applied by ROOT. This estimate corresponds to an average RAW event size of ~ 55 KB.

A possible variation of the previous estimates can come from the handling of the data related to the digitization of the trigger signals, already explained in section 6.3. The digitization of the trigger signal is needed to optimize the time alignment resolution among channel groups. As of now, the details of this time optimization have yet to be defined. If the time optimization can be applied during the L1 trigger stage, the digitized triggers will not be saved to the RAW event structure. If, on the other hand, we want to keep this information so that the time optimization

Sub-detector	Readout type	N. of channels		Storage	
		Total	0-suppressed	MB/s	TB/year
Active target	ADC	30	9	0.92	29.1
Calorimeter	ADC	656	11	1.13	35.5
SAC	ADC	32	7	0.72	22.6
Spectrometer	TDC	200	-	0.04	1.3
Positron veto	TDC	50	-	0.01	0.3
Total		**968**		**2.82**	**88.8**

Table 7.2: Estimated total amount of RAW data collected in one year of data taking with contributions from each sub-detector. This estimate assumes 365 days of data acquisition and no data compression.

can be re-computed during future event reprocessing, saving digitized triggers data in the RAW event structure will contribute to the final storage needs. This contribution depends on the number of channels passing the zero-suppression algorithm. We assume here an average contribution due to trigger data of $\sim$ 30 KB per event[1], corresponding to additional 50 TB/y of storage to be added to the foreseen 89 TB/year of Tab. 7.2.

In parallel to the main data stream, O(1%) of the data will be written to disk without applying the L0 zero suppression algorithm (see section 6.2.1). These auto-pass events will contribute for 0.6 MB/s to the L1 data rate, corresponding to an additional 20 TB/y of storage if this stream is always enabled.

As explained in section 7.2.2, for each channel the RECO format will not include the full set of ADC samples but only reconstructed quantities, including (but not limited to) the total charge collected, the raw and calibrated energies, and the time information. In addition the RECO format will contain information about all reconstructed higher level physics objects, namely clusters and tracks. Given the average composition of the events estimated by Monte Carlo studies, we expect at least a O(50) reduction factor in the storage space needed for RECO events wrt RAW events.

As the THIN events do not include any information related to the single readout channel but only those related to high level physics objects, we expect an additional factor 10 reduction in the storage space needed for these events.

7.5 Online control system

PADME has a foreseen initial data taking period in excess of 1 year, during which the DAQ will have to function uninterrupted for long periods of time. Given the relatively small size of the collaboration, it will be very hard to guarantee a constant presence of shifters at the site, especially at night and during the week-ends.

To allow for unattended DAQ, the system will need the definition of a set of automatic recovery procedures and the creation of a remote alarm systems. While a remote control system would also

[1] As we want to keep only the digitized trigger signals associated to channels passing the zero-suppression algorithm, the total number of triggers to save will depend on the relative positions of those channels: 8 channels can require from 8 different trigger signals if they are all far apart to a single trigger signal if they belong to the same channel group of a V1742 board. The Active target will then contribute to each event with 2 to 4 trigger signals, the SAC with 1 to 4 trigger signal and the Calorimeter with 2 to 11 trigger signals, for a total of 5 to 19 signals per event, corresponding to an addition of 12 to 60 KB of data per RAW event. If we assume an average of 16 trigger signals per event, we obtain a contribution of $\sim$ 30 KB of data per event.

be highly desirable, the security implications of such a system will have to be carefully examined. We are currently examining the solutions adopted by other collaborations.

In any case, the experiment control system will have to be tightly integrated with that of the BTF, so that local intervention in case of emergencies will be always guaranteed by the 24/7 on-site support for the beam.

7.6 Networking

The networking infrastructure will connect the DAQ PCs to the local storage infrastructure and to the storage and computing resources located outside the PADME experimental area.

At the experimental site the local network connection must allow writing the data produced by the L0 DAQ stage to the local disk buffer and its consequent reading by the L1 stage for event build. Given the estimated L0 output rate of 2.8 MB/s, no special networking solutions are required to support it: all L0, L1, and disk servers can be connected via a standard (possibly redundant) Gigabit Ethernet switch.

As the final data rate to be written to the Central Data Recording facility is relatively low and can be estimated in less than 5 MB/s including RAW data production and all additional information produced in the data acquisition process, the current 1 Gbps link connecting the BTF/PADME Control Room to the LNF Central Computing Services (CCS) can be considered adequate. On the same line, the foreseen 10 Gbps general traffic geographical link from the LNF CCS to the GARR backbone satisfies all connectivity requirements for our collaboration.

A special case must be considered if the PADME Central Data Recording facility is not located at the LNF CCS but, e.g., at the INFN CNAF. In this case an appropriately sized geographical link dedicated to PADME must be created between LNF and CNAF in order to guarantee the bandwith needed by the data taking process.

7.7 Database

As explained in sections 7.2 and 7.3, data related to Calibration constants, Detector Conditions, and Run Configuration will be written to a centralized database. This database will also contain a map of all data files produced during DAQ, MonteCarlo production and data reprocessing, including a full list of replicas for each file.

For the on-going test beams, we are temporarily using a local DB system based on SQLite3. Given the DB know-how already available both within the collaboration and at the LNF CCS, the central DB will be very probably based on the MySQL database management system: this will guarantee the necessary resiliency and portability of the system.

7.8 Monte Carlo production

A GEANT4-based simulation of the full experimental setup has already been implemented for the current design and is being run on a HP Proliant DL560 server with 4 Intel Xeon E5-4610v2 2.3GHz CPUs, for a total of 32 cores, and 128 GiB of ECC RAM.

For each event we simulate the interaction of a bunch of particles with the experimental setup and record information about each active channel in term of time and energy released. A preliminary estimate shows an average SIMU event size of O(1 KB) with a production rate of 3 Hz/core, i.e. 3 fully simulated bunches per second per core. The speed of the simulation heavily depends on the possibility of simulating the full development of the electromagnetic showers in the SAC detector only if at least one photon impacts on the ECAL. This possibility has to be carefully examined and will require some manipulation of the GEANT4 particle tracking process. If the full SAC simulation is always required, a substantial increase (even in excess of a factor 10) of the simulation CPU requirements must be foreseen.

Given the functioning parameters of the PADME beam (bunches of O(5000) $e^+$with a frequency of 50 Hz) we expect a total number of O(10^{13}) e^+ per year over O($2x10^9$) bunches. If we require the Monte Carlo statistics to be 10 times that of the real data, we will need a total amount of storage of 20 TB per year and 210 dedicated CPU cores, corresponding to 7 servers analogous to the existing one. More on this point in Section 7.10.

As the average RECO event size is similar for Monte Carlo and real data, the storage of the full Monte Carlo statistics in RECO format can be very roughly estimated in 20 TB per year.

7.9 Software

The PADME computing model will be based on software packages which are considered standard in most HEP recent experiments, namely ROOT [65] for data persistency and analysis and GEANT4 [66] for detector simulation. Both packages are actively supported by CERN and by a large HEP community.

The natural environment for the basic computing tasks of the experiment (DAQ, event reconstruction, physics analysis, detector simulation) is composed by the Linux operative system in conjuction with the GCC compiler. In both cases, the choice of the version to use will depend on the requirements coming from the software packages in use.

Most of the software development will be based on the C++ programming language, with the notable exception of the on-line DAQ system, which is being developed in C for compatibility with the CAEN data acquisition libraries. We also foresee the use of the most common scripting languages (bash, Python, Perl) to handle logistic tasks and interactions with the users.

7.10 GRID

The use of GRID computing resources, if available, will be included in the final PADME Computing Model. Indeed, part or all of the Monte Carlo production can be easily migrated to the GRID to take full advantage of any available resource and we plan to explore the modalities to create a PADME VO in the immediate future.

On the other hand, given the extra complexities of migrating the main data reconstruction to the GRID and the relatively limited amount of computing resources required for this task, we expect that the Central Data Recording and Central Data Processing facilities will be located in a single computer center and will use dedicated resources.

Finally, the creation of a PADME VO will allow PADME users to access GRID resources for individual data analysis: the details for this facility will be defined at a later stage.

7.11 Costs

To give a very preliminary estimate of the costs of the computing resources needed by the PADME experiment, we will use the computing needs estimated in the previous sections and assume that all computing will be based in a single site and run on dedicated CPU, disk, and tape resources.

The cost of a CPU server analogous to the HP Proliant DL560 currently in use is at the time of writing of about 6 K€ (V.A.T. included). Given the computing requirements for DAQ, reconstruction, and Monte Carlo production, we will need about 10 such servers, for a total of 60 K€.

Storage resources are usually organized in hierarchical structures including RAID systems and tape libraries. If the storage system must be created from scratch, to the cost of the storage media one has to add the cost of the RAID servers and the tape libraries and drivers, plus the connection infrastructure. Locating the PADME computing facility in an existing data center would allow access to the local storage infrastructure, reducing the costs of its creation.

Here we assume that we will be using an existing storage infrastructure so that only the costs of minor expansions to the infrastructure (e.g. tape drives and/or disk cabinets) and of the storage media must be considered. Conventionally this assumption leads to a cost per TB of the order of 200 € for RAID disks and 100 € for tapes.

To store the 90 TB/year of RAW data we will then need 18 K€ for the disks and 9 K€ for the tapes. The addition of trigger information will require an additional 10 K€ of disks and 5 K€ of tapes, while storing autopass data will require 4 K€ of disks and 2 K€ of tapes. Storing all RECO and THIN data will only give a small contribution to these costs.

Storing the 40 TB of Monte Carlo data (20 TB SIMU + 20 TB RECO) will require 8 K€ of disks and 4 K€ of tapes.

While all produced data will be written to tape for long term storage and access, it is very likely that only part of the full RAW data statistics will be kept on disk at any one time. This will accordingly reduce the total cost of disk storage.

In total wil will need approximately 20 K€ of tape storage and up to 40 K€ of disk storage per year, this last number depending on the fraction of RAW data to be kept on disk at any one time.

Chapter 8

Simulation and sensitivity

8.1 PADME Monte Carlo simulation

To understand the actual sensitivity of the PADME experiment to A', a full GEANT4 simulation has been developed. The aim of the PADME MC is to simulate oder of 10^{13} positron interactions. For this reason the simulation is tuned to be fast avoiding in some case the full shower simulation in the detectors downstream the calorimeter. The simulation describes in detail the geometry of the experiment, when consolidated, simulate the electromagnetic showers into the electromagnetic calorimeter and produces energy deposit in each single crystal. To save computing time the absorption of the primary beam in the beam dump is not simulated, nor the shower development in the Small Angle Calorimeter.

To describe the bunch structure, a simultaneous multi-positron gun is implemented, taking into account beam spot size, energy spread, beam emittance according to measurements performed at BTF.

The simulation uses the GEANT4 low-energy electromagnetic libraries, including two photon annihilation, ionization processes, Bhabha and Møller scattering, and production of δ-rays. A custom generator was developed to simulate the A' production and its eventual decay into e^+e^- or $\chi\overline{\chi}$, and the annihilation in three photons.

The physical properties (lifetime and decay kinematics) of the A' are dependent on two external parameters (ϵ and $M_{A'}$), allowing the simulation of the acceptance for different A' mass value. A complete mass scan from 2 MeV/c^2 $< M_{A'} <$ 22 MeV/c^2 is performed in each sensitivity estimate.

8.2 Dark photon generators

Events with a single dark photon produced per bunch were generated to study the signal acceptance of the detector and the developed selection criteria. One of the positrons was treated in a custom way while the rest of the bunch particles were traced through the active target by GEANT4.

Since the A' production in $e^+e^- \to A'\gamma$ exhibits two body kinematics a separate module was developed. A' was assumed to decay consequently into e^+e^- pair. The products of the generated process were then transmitted to GEANT4 instead of the primary positron to complete the simulation of the detector response. An option was added either to consider or not the e^+e^- pair allowing to study both the visible and the invisible dark photon final states, in which the only SM particle traversing the detector is the recoil photon.

The generated dark photon events were mixed with the pure GEANT4 simulated events in a fraction according to the A' production cross section, $\sigma(e^+e^- \to A'\gamma)$, for a given M_{ee}. The

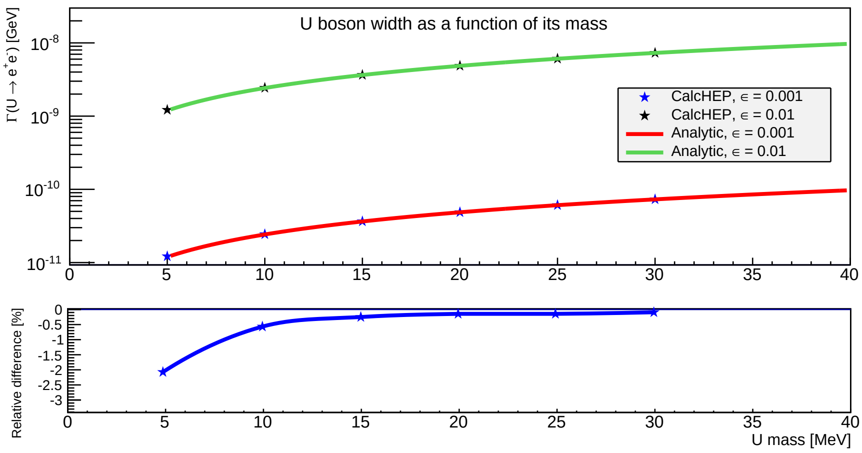

Figure 8.1: Analytically calculated $\Gamma(A' \to e^+e^-)$ compared to the model implemented in CalcHEP. Matching between the different calculation is better than 2.5%.

$\sigma(e^+e^- \to A'\gamma)$ was calculated with CalcHEP - a package for calculation of Feynman diagrams [59]. Provided the Lagrangian term CalcHEP can give the cross section for a given process, the kinematics of the final state particles and even advanced event selection can be performed.

The Lagrangian term was chosen exactly according to equation (2.6). A crosscheck was performed by comparing the width of the decay $A' \to e^+e^-$ calculated both with CalcHEP and with the analytic formula (2.13), as shown in Figure 8.1. The agreement between the results was better than 2.5%, validating the applicability of the introduced model also for study of other processes, like $e^+e^- \to A'\gamma$.

8.2.1 The annihilation generator

The cross section for two photon annihilation process of e^+e^- at a given center of mass energy is well described by the Heitler formula. Exactly this model is used by GEANT4 as one of the possible physics scenarios for a positron interaction. A comparison between GEANT4 and the cross section calculated with the CalcHEP package for positron interacting on a carbon target is shown in Figure 8.2. Due to the perfect agreement between CalcHEP and GEANT4 cross section the production of two photon final states in e^+-on-target process was left entirely to GEANT4.

However, this is not the case with the higher order processes, like for example the three photon annihilation $e^+e^- \to \gamma\gamma\gamma$. The on-shell cross section $\sigma(e^+e^- \to \gamma\gamma\gamma)$ is divergent when $E_\gamma \to 0$. This infrared divergency is cancelled out by the radiative correction but from experimental point of view a cut on the minimal photon energy E_γ^{min} is necessary at events generation level. A value of E_γ^{min} >5 MeV in the lab system was chosen. Initial state radiation (ISR) with energy less than 5 MeV decreases the visible e^+e^- invariant mass from 25.8 MeV to 25.7 MeV (for 650 MeV beam) and is taken into account through the simulation of 1% beam energy spread. The relative cross section was obtained to be

$$\sigma(e^+e^- \to \gamma\gamma\gamma)_{E(\gamma)>5MeV}/\sigma(e^+e^- \to \gamma\gamma) = 7.5 \cdot 10^7 pb/1.8 \cdot 10^9 pb = 4.2\%$$

and the generated events were traced through the experimental setup.

A crosscheck of the CalcHEP calculations with an analytical model is in progress.

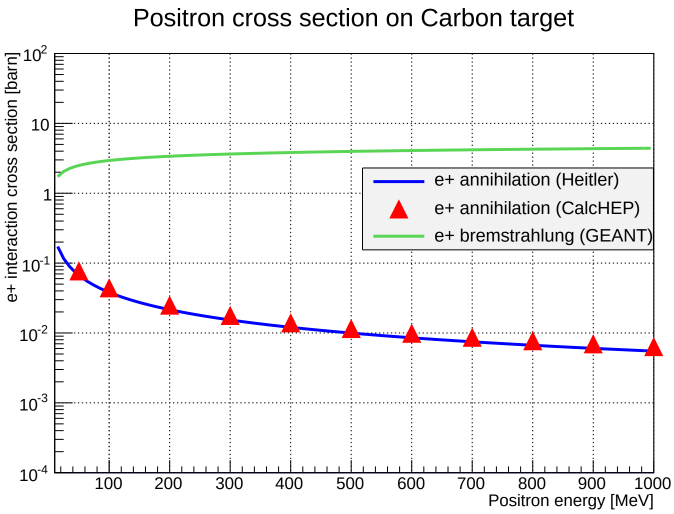

Figure 8.2: *Positron cross section on a carbon target.*

8.3 The beam line description

A critical part of the experiment simulation is the description of the beam line. In fact, since the value of the 4-momenta of the incoming positron is not measured on event by event basis, the average beam position and energy is used to reconstruct the missing mass. For this reason the estimated resolution of the M^2_{miss} strongly relies on the correct description of the beam spot size, divergence and energy spread.

In Tab. 8.1 the beam parameters used in the sensitivity estimates are summarised. The numbers

Beam Parameter	Value	Units
Beam energy E_0	550.0	MeV
Beam energy spread σ_E	1%	
Pulse length	40.0	ns
Micro-bunch spacing	0.350	ns
Micro-bunch Length	0.150	ns
Beam size y (std. dev.) σ_x	0.7	mm
Beam size x (std. dev.) σ_y	0.7	mm
Beam divergence x	10^{-3}	rad
Beam divergence y	10^{-3}	rad
Vacuum pressure	10^{-6}	mbar

Table 8.1: Simulated beam paramters

reproduce present beam performance and do not include so far the possible improvements foreseen for the BTF beam line. The beam is represented as a Gaussian beam with 1% energy spread and 1 mrad divergence (see Fig. 8.3).

The beam spot size is a little bit smaller than 1 mm radius and the micro-bunching consists of bunches of 110 ps length separated by 350 ps of no beam, repeated to fill the pulse length of 40 ns 8.4. While the spot size and beam divergence play a crucial role in the determination of

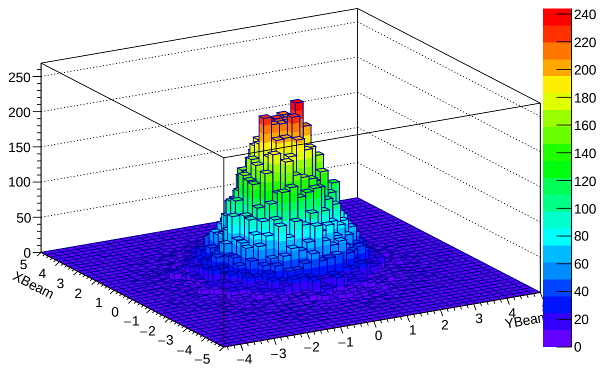

Figure 8.3: MC description of the beam spot.

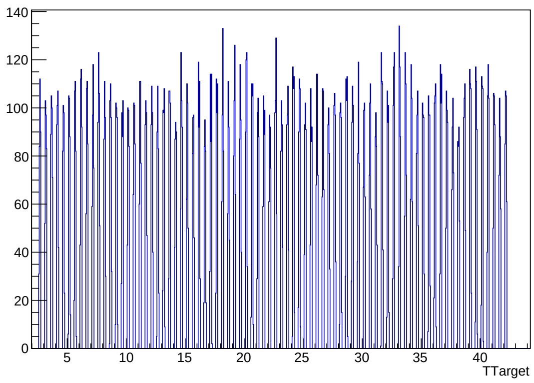

Figure 8.4: Monte Carlo simulation of the micro-bunch structure of the BTF beam

the detector performance in measuring the M^2_{Miss}, the timing structures determines the cluster multiplicity in the calorimeter.

8.4 PADME GEANT4 detector description

The Monte Carlo detector geometry includes a description of all the active detector as well as the description of known passive material distribution. The vacuum region is not yet described properly because the vacuum chamber design has been not yet finalized.

In Fig. 8.5 a view of the detector geometry implemented in GEANT4 is shown

8.4.1 The target simulation

In the PADME MC the diamond target is as a $20 \times 20 \times 0.1$ mm^3 diamond foil with currently no readout strips description. This reflect the readout technique adopted for the PADME target in which pure graphite contacts are used for the charge collection. At present no description of the supports and vacuum equipment is performed and no coordinates reconstruction is implemented. Being the beam spot size much larger with respect to the spatial resolution of the target itself, the resolution on the measured values of the beam position is expected to be negligible.

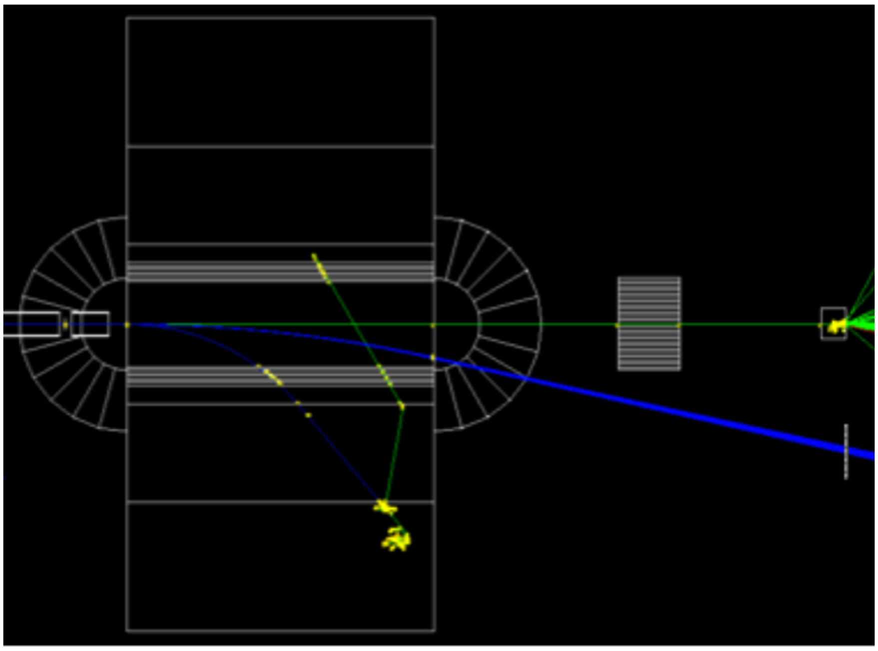

Figure 8.5: Display of the GEANT4 Monte Carlo detector description.

8.4.2 The magnet simulation

The PADME magnet is fully described in the Monte Carlo including passive material as shown in Fig. 8.5. Showers developed by electron and positrons in the magnet iron are simulated. The gap vertical dimension was fixed to 230 mm according to the modification needed for the PADME setup. The magnetic field is considered to be uniform inside a box of $200 \times 520 \times 1000$ mm^3 inside the joke region and zero outside. No fringing fields description is provided in the region of the coil. Magnetic filed mapping in figure 5.21 has not been used due to very different vertical gap dimension, just 110 mm. Better description of the magnetic field is necessary and will be implemented as soon as a new field mapping will be performed.

8.4.3 The calorimeter simulation

The PADME calorimeter geometry is described in the Monte Carlo just by placing the crystals in the proper positions. No mechanical supports and passive material description is provided as shown in Fig. 8.5. The electromagnetic showers are simulated up to the energy deposit in each crystal but no simulation of the scintillation light and of the photosensor behaviour is provided. Single crystal energy is obtained by summing the energy of all the hits in the event without checking for their time compatibility. Such approach accounts for the very long decay time of the BGO scintillation light with respect to the 40 ns bunch length. Cluster timing is obtained by assigning to each crystal the time of the first hit in the event.

8.5 PADME reconstruction

At present the Monte Carlo does not include any digitization and the computed physical quantities are obtained using energy deposits in the detectors. Only in the calorimeter energy clusters are built and cluster energy, time, and transverse coordinates (x and y) are propagated in the output variables. The cluster energy is reconstructed according to the algorithms described in section 5.4.7 starting from energy deposits in the single crystals. Cluster time is obtained as the energy weighted average of the participating crystals. Cluster coordinates are calculated as the weighted average of crystals central positions.

8.6 Monte Carlo samples

In each of the sensitivity studies different events samples are generated by using PADME Monte Carlo. A simulated bunch consists of 5,000 positrons distributed, according to the time structure described in Fig. 8.4, in a 40 ns. The background generated by Bremsstrahlung and annihilation is measured by generating sample of 2.5×10^{10} positrons impinging on the diamond target. The three photons background is not included in the GEANT4 low energy electromagnetic library and it is generated tracking into the PADME geometry photons produced by CalcHep program. In this case a three photons event is included in a 5,000 positrons bunch. Considering the cross section $\sim 15 \times 10^3$ three photons events are necessary in a 2.5×10^{10} positron on target sample.

To compute the A' acceptance after the signal selection, Monte Carlo samples including an invisibly decaying dark photon in each bunch are produced for different masses.

Chapter 9

Sensitivity

The sensitivity studies described in the following are based on simulations of a beam of 5,000 positrons/bunch of energy 550 MeV in 40 ns long bunches. The detector configuration is the one with $10 \times 10 \times 200$ mm^3 crystals, placed at 200 cm from the diamond target, and no high energy positron veto. New studies are ongoing with the upgraded detector configuration and the increased target–calorimeter distance.

9.1 Analysis strategy

The process $e^+e^- \rightarrow A'\gamma$ has the same theoretical treatment as the Standard Model annihilation process, except for the suppression factor ϵ on the coupling constant and the fact that A' is massive. The latter condition results in a resonant enhancement of the dark photon production cross section when the A' mass approaches the $\sqrt{s}$. This effect is evident in Fig. 9.1 where the ratio of the two cross sections is shown for $\epsilon = 1$.

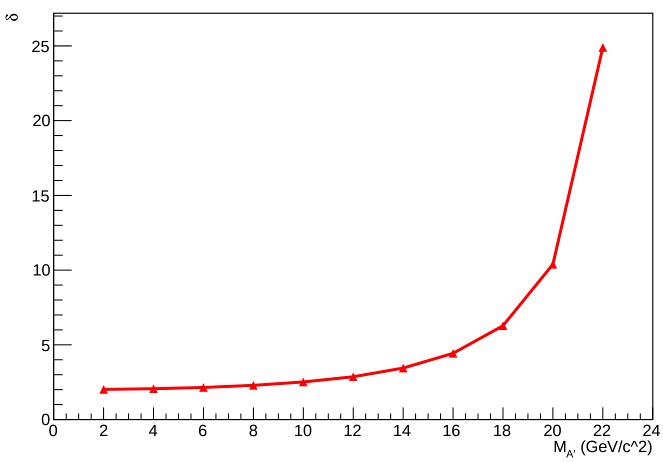

Figure 9.1: Cross section enhancement factor δ for beam energy 550 MeV.

The A' coupling constant ϵ can be determined using the formula:

$$\frac{\sigma(e^+e^- \rightarrow A'\gamma)}{\sigma(e^+e^- \rightarrow \gamma\gamma)} = \frac{N(A'\gamma)}{N(\gamma\gamma)} * \frac{Acc(\gamma\gamma)}{Acc(A'\gamma)} = \epsilon^2 * \delta, \tag{9.1}$$

where $N(A'\gamma) = N(A'\gamma)_{obs} - N(A'\gamma)_{bkg}$ is the number of the signal candidates after the background subtraction, $N(\gamma\gamma)$ is the number of observed annihilation events, δ is the $e^+e^- \to A'\gamma$ cross section enhancement factor and $Acc(\gamma\gamma)$ and $Acc(A'\gamma)$ are the corresponding acceptances for the signal and normalization channels.

The candidates selection is based on the missing mass squared variable, calculated according to formula:

$$M^2_{miss} = (P_{e^-} + P_{beam} - P_\gamma)^2. \tag{9.2}$$

with the target electrons assumed to be at rest ($\vec{P}_{e^-} = \vec{0}$) while for the beam a nominal momentum of 550 MeV along the z axis is used. Its distribution should peak at $M^2_{A'}$ for A' decays, at zero for the concurrent $e^+e^- \to \gamma\gamma$ process, and should be smooth for the remaining background. The approach described provides sensitivity for both visible and invisible searches.

The signal region is defined as $\pm 1.5\sigma_{M^2_{miss}}$ around the reconstructed value of M'^2_A, with resolution $\sigma_{M^2_{miss}}(M'_A)$. A simple and preliminary selection aiming to identify candidate $A' \to \chi\chi$ events has been developed.

9.2 Invisible decay selection

In case of A' invisible decay the final state observed in the PADME experiment will consist in a single γ cluster in the crystal calorimeter. The selection cuts applied to identify $e^+e^- \to \gamma + nothing$ are the following:

- Only one cluster in the calorimeter.

  This cut allows to reject most of the annihilation and 3γ events.

- Cluster energy within $E_{min}(M_U) < E_{Cl} < E_{max}(M_U)$.

  The energy cut is intended to reject low-energy photons from Bremsstrahlung radiation and to define a maximum energy of the positron in the spectrometer acceptance to avoid pile up. The energy spectrum of the recoil photons is different for different A' masses, resulting in $E_{min}(M_U)$ varying over the interval 50–150 MeV while $E_{max}(M_U)$ is between 120 and 350 MeV.

- Cluster radius in the calorimeter 5 cm $< R_{Cl} <$ 13 cm.

  This cut reduces the energy leakage and improves M^2_{miss} resolution.

- No in-time tracks in the charged particles veto.

  The positron veto cut aims at completely rejecting the Bremsstrahlung γ by detecting the beam positron inside the spectrometer. Due to the requirement of $E_\gamma > 50$ MeV, the positron is deflected out of the beam by the magnet and enters the acceptance of the charged particle vetos.

- No photon with $E > 50$ MeV in the small angle calorimeter.

  This cuts allows rejecting most of the 3γ events which have one of the additional clusters in the central calorimeter hole.

With this selection, an acceptance of $\sim 17\%$ has been achieved for A' boson masses up to 22 MeV. Acceptance will strongly depend on the cluster minimum and maximum energy and an optimisation in acceptance versus background rejection is needed, for each value of the A' mass.

9.2.1 Background estimation

The PADME sensitivity to $A' \to \chi\chi$ is limited by the single-photon background. It has been estimated by applying the signal selection cuts to the e^+-on-target GEANT4 Monte Carlo sample together with a dedicated 3γ sample generated with CalcHEP [59] software.

In Bremsstrahlung events, the sum of the energies of the positron track and the cluster should be equal to the beam energy since the target is very thin. In $\gamma\gamma$ events the final state has only two clusters and the sum of their energies is equal to the beam energy.

The Bremsstrahlung, the process with highest cross section, leads to production of many low energy photons emitted mostly at small angles. For carbon target and 550 MeV beam energy, about 5×10^2 photons with energy > 1 MeV are produced for each annihilation interaction The calorimeter has a central hole with an aperture of 1.15°, minimizing the sensitivity to these photons.

Because of the closed kinematics the energy and the angle of the annihilation photons are correlated. Due to detector resolution the kinematical region allowed for annihilation photons overlaps that for a low mass A'.

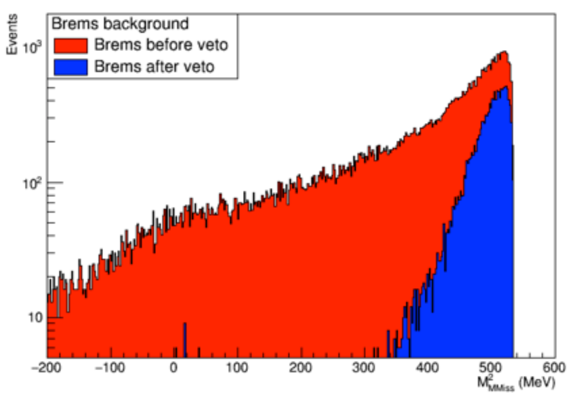

Figure 9.2: Bremsstrahlung background distribution before (red) and after (blue) applying charged veto rejection cut.

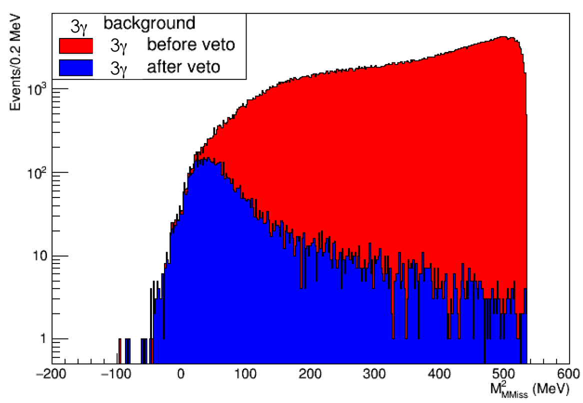

Figure 9.3: 3γ background distribution before (red) and after (blue) applying small angle calorimeter veto rejection cut.

To minimize background of this type, a veto on extra clusters in the calorimeter and the small angle calorimeter is applied, leading to a negligible contribution from $\gamma\gamma$ final states. The energies of photons produced by synchrotron radiation are very low, at most reaching the hard X-ray region (∼10 KeV). Nevertheless the deflection of the intense beam can give rise to several thousand of these photons, slightly worsening the calorimeter energy resolution.

An additional background originates from the process $e^+e^- \to \gamma\gamma(\gamma)$ when the third photon is generated in electron or postron ISR or FSR. When just a single photon is detected by the calorimeter the reconstructed missing mass is equal to the invariant mass of the two missing photons and lies in the signal region. That scenario represents an irreducible background when the two photons fly through the inner hole of the calorimeter. Initial state radiation (ISR) with energy less than 5 MeV decreases the visible e^+e^- invariant mass from 23.7 MeV to 23.6 MeV and is taken into account through simulating the 1% beam energy spread.

The emission of a hard photon has been studied using CalcHEP. The relative cross section obtained is:

$$\sigma(e^+e^- \to \gamma\gamma\gamma)/\sigma(e^+e^- \to \gamma\gamma)_{E(\gamma)>5MeV} = 7.5 \cdot 10^7 \text{pb}/1.8 \cdot 10^9 \text{pb} = 4.2\%$$

and the generated events were traced through the experimental setup to obtain the remaining background. It has been observed that this background is efficiently rejected by the condition of no cluster in the small angle calorimeter (see Fig. 9.3).

Other background processes like Bhabha scattering and pile up of annihilation events are included in the background estimation through the GEANT4 simulation of the interactions of the primary positron beam. Double annihilation events produce extra clusters and due to energy/angle relation are additionally suppressed with respect to single ones.

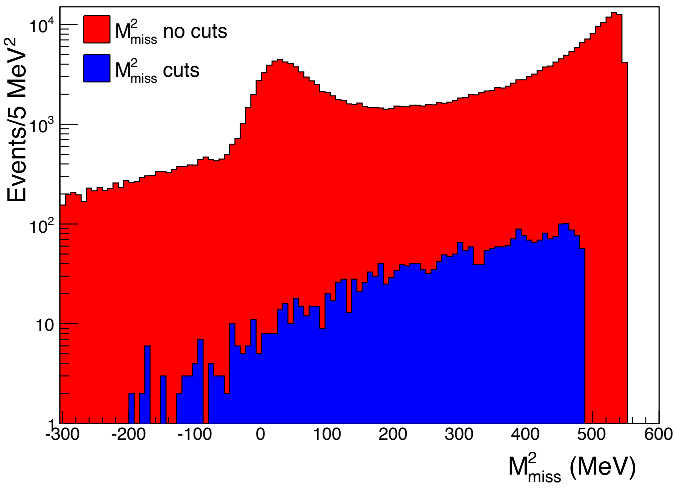

Figure 9.4: M^2_{miss} for background events. In red with no selection cuts in blue after all cuts applied.

Fig. 9.4 shows the distribution of the simulated background events before (red) and after (blue) the described selection. The annihilation background peaks at $M^2_{miss} = 0$, the Bremsstrahlung is located in the region of high M^2_{miss} values while the three photon background populates the entire region.

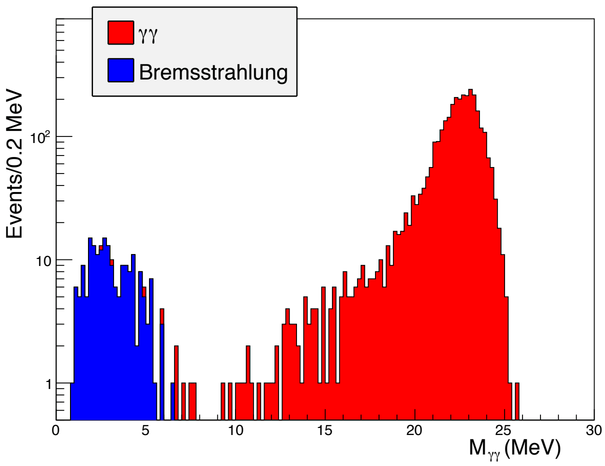

Figure 9.5: $M_{\gamma\gamma}$ mass distribution.

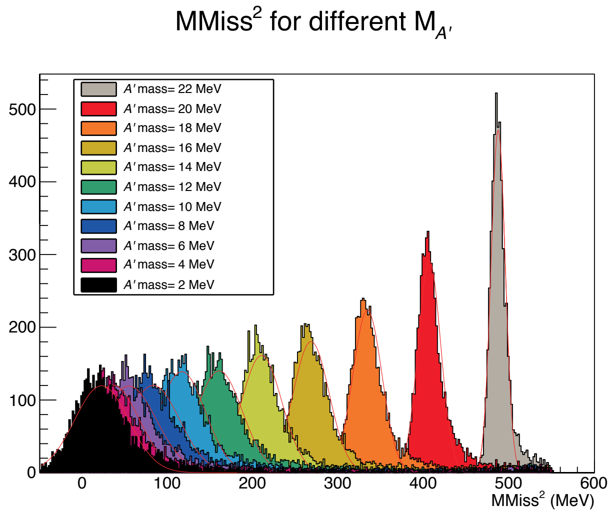

Figure 9.6: Missing mass squared distribution as a function of A' mass.

9.2.2 Positron flux measurement

The total number of annihilation events ($N(\gamma\gamma)/Acc(\gamma\gamma)$), which are used for normalization, can be determined in two independent ways. The first is to exploit the active target for the measurement of the beam flux and use the known value of $\sigma_{e^+e^-\to\gamma\gamma}$. The signal produced by the active target is proportional to the number of positrons crossing the target itself. Its calibration can be performed by shooting the beam directly onto the calorimeter through the target, measuring the energy deposit and comparing it with the signal from the active target.

Using this curve the number of primary positrons, and therefore the total flux, can be measured in each single bunch. Then the number of annihilations can be calculated as

$$N_{\gamma\gamma}^{tot} = \frac{N_{\gamma\gamma}}{Acc_{\gamma\gamma}} = Flux(e^+) \cdot \sigma_{\gamma\gamma}, \tag{9.3}$$

since the cross section for the annihilation process ($\sigma_{\gamma\gamma}$) is known with very good precision.

Alternatively, direct reconstruction of the $e^+e^- \to \gamma\gamma$ annihilation events can be performed. For the selection of $\gamma\gamma$ events the same geometrical cuts for signal events are used. Two clusters in the calorimeter are required, each with reconstructed energy 100 MeV $< E_{Cl} <$ 400 MeV and radius 5 cm $< R_{Cl} <$ 13 cm. The $\gamma\gamma$ invariant mass is reconstructed assuming the particles come from the target z position, i.e. after a flight-path of lenght D equal to the target–calorimeter front face distance, and using the formula:

$$M_{\gamma\gamma} = \frac{\sqrt{[(x_{\gamma 1} - x_{\gamma 2}) + (y_{\gamma 1} - y_{\gamma 2})]E_{\gamma 2}E_{\gamma 2}}}{D}$$

In Fig. 9.5 the distribution of $M_{\gamma\gamma}$ from Monte Carlo is shown. The genuine $\gamma\gamma$ events (in red) peak at the centre of mass energy of the e^+e^- pair while the negligible Bremsstrahlung background (in blue) is situated at small $M_{\gamma\gamma}$. The expected contamination from Bremsstrahlung processes in the signal region is well below the 0.1% level. The resolution on $M_{\gamma\gamma}$ is found to be 1 MeV.

Using the GEANT4 simulation and the invariant mass cut 20 MeV $< M_{\gamma\gamma} <$ 26 MeV, the acceptance for this selection has been measured to be $\sim$ 7%, with a calorimeter geometrical acceptance for two photons of $\sim$ 17%. The expected precision in the measurement of the flux is dominated by the value of the annihilation cross section, since the statistical error on $\gamma\gamma$ sample is $\sim$0.05 %.

Combining the two results for the number of primary positrons, the cross section for the annihilation process ($\sigma_{\gamma\gamma}$) can be measured as a by-product. This will help to cross check the reliability of the obtained flux, minimizing the systematics.

9.2.3 Sensitivity

With the described experimental setup and simulation technique $2.5 \cdot 10^{10}$ positrons on target were generated in bunches of $5 \cdot 10^3/10$ ns, in order to study the effect of pile up events. In addition, samples of 10^3 events were generated for A' masses 2, 4, 6, 8, 10, 12, 14, 16, 18, 20 and 22 MeV, with a single A', together with $5 \cdot 10^3$ positrons.

The missing mass distributions for some of the masses are shown in Fig. 9.6. The acceptance and the expected number of background events were obtained by running the events through the previously described selection.

The background has been scaled by a constant factor of 400 to account for 1 year of running at a repetition rate of 49 Hz, with $2 \cdot 10^4$ positrons in 40 ns long bunches, corresponding to a total of 10^{13} positrons on target. Under the assumption of no signal, an upper limit on the coupling ϵ

can be set, using the statistical uncertainty on the background. The expected exclusion region is shown in Fig. 9.7 by the red solid line dubbed “40 ns”.

The two dashed lines refer to the same data period but with extended bunch width and number of primary positrons per bunch scaled accordingly: the dashed line corresponds to $8 \cdot 10^4$ positrons in 160 ns long BTF bunches, while the dotted line corresponds to $2.4 \cdot 10^5$ positrons/bunch in the case that 480 ns bunches can be produced.

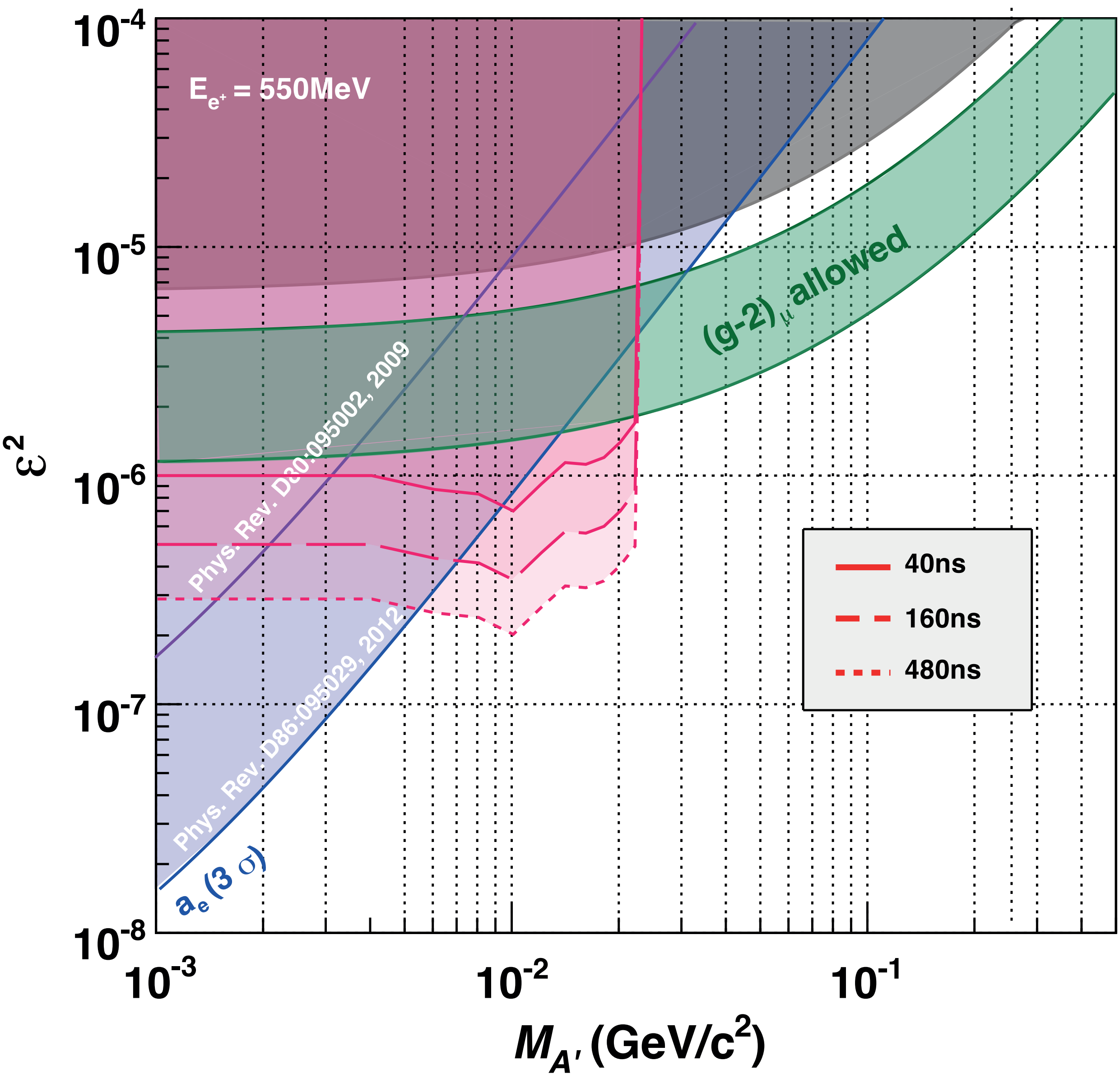

Figure 9.7: Expected exclusions in the invisible channel compared with the band of values preferred by current $g_\mu - 2$ discrepancies.

Chapter 10

PADME costs and time line

The costs we evaluate here are relative to R&D, construction and running of the PADME experiment for the search of $e^+e^- \to \gamma +$ *nothing*, excluded the costs for the improvements and upgrades of the beam infrastructure (DAΦNE LINAC and BTF).

Concerning the operations costs, they will be dominated by the cost of running the DAΦNE LINAC and the general services, which is a small fraction with respect to the cost of full complex, as summarized in Fig. 10.1. This is expected, since the LINAC magnets, RF, gun, services, etc. have a total power of 250 KW (including the BTF and the transfer line), to be compared to 2.2 MW total power of the entire DAΦNE plant.

To this power budget, for PADME we have to add the MBP-S magnet (40 KW if using the 400 A available supply) plus the experiment electronics, acquisition and ancillary services. A total power consuption of the order of 300–350 KW is thus expected.

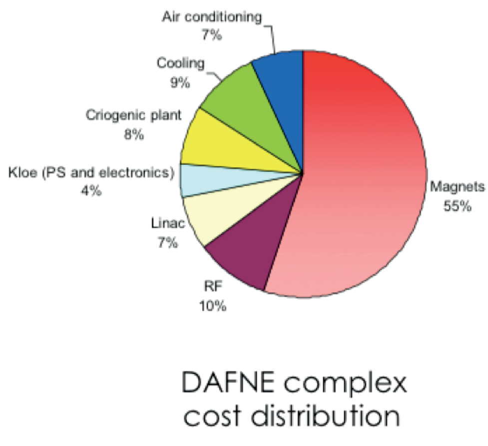

Figure 10.1: Breakdown of the DAΦNE complex running costs.

10.1 Cost estimate

10.1.1 Magnet

As discussed in the dedicated Sec. 5.3, the costs related to the MBP-S magnet will be the transport from CERN to Frascati (we have estimated 3 K€, taking into account the dimensions and weight),

Item	2015	2016	2017	2018	Total
	K€				
Scintillator and SiPM		14			**14**
Front-end electronics		40			**40**
Discriminator boards			50		**50**
Total		**54**	**50**		**104**

Table 10.1: Summary table of the costs of positron and electron veto detectors, scintillator based: VAT is included, TDC boards, crate and VME controller excluded.

and the services needed to use the magnet with the existing infrastructure of the DAΦNE complex, in particular the electrical and cooling connections, as well as a supporting structure with some capability of (rough) alignment. For these items we have preliminary estimated 20 K€.

10.1.2 Charged particles veto detectors

Inside the magnetic field, along the lateral sides of the gap of the PADME magnet (spectrometer veto), and outside the magnet (high energy positron veto), we foresee segmented detectors for detecting positrons (and electrons), mainly with the purpose of rejecting Bremsstrahlung events.

These detectors will be readout with a simpler system with respect to the DRS4 digitizer boards, based on VME TDCs.

We are planning to realize these systems with extruded scintillators with SiPM readout. We need 2×100 detector elements to cover the ≈ 1 m lenght of the magnet, plus additional 50 cm for the high energy positron veto. The relative costs are summarized in Tab. 10.1.

In the general layout we also have the option of an additional “imaging veto”, expected to be inside the positron beam, with the aim of detecting higher energy positrons irradiating soft photons. We expect this to be a Silicon pixel detector, but at this stage the characteristics of this option are not well defined. Taking into account the beam parameters, we expect this detector to be of the order of 50×100 mm^2, and we preliminarly estimate an overall cost of 150 K€.

10.1.3 Diamond target

The overall cost is of the order of 72 K€, the evolution is shown in in Tab. 10.2, including V.A.T. and contingency cost (2 K€ have been spent for diamond sensor prototypes in 2015).

Item	2015	2016	2017	2018	Total
	K€				
Diamond target construction	2	20			**22**
Mechanics and movement		10			**10**
FEE		40			**40**
Total	**2**	**70**			**72**

Table 10.2: Estimated active diamond target core cost (VAT and contingency included) per year.

10.1.4 Calorimeter

The main cost driver is of course the most valuable and complex detector: the calorimeter. In the hyphotesis of “small” crystals, i.e. 656 BGO elements 1×1 cm^2, 20 cm long, we need to cut and

Item	2015	2016	2017	2018	Total
	K€				
Crystal cutting	15	36			
Crystal wrapping		21			**122**
Mechanics		50			
Photo-sensors	5	95			**100**
FEE		32	96		**128**
Total	**20**	**234**	**96**		**350**

Table 10.3: Summary table of the costs of the calorimeter by using the BGO crystals from the L3 experiment.

polish at least 170 original L3 BGO crystals. Based on the cost of the preliminary cutting and polishing (done by Gestione SILO, Scandicci, Italy), we expect a unit cost of order 300 € (VAT included). To this 51 K€ the cost of painting or wrapping should be added. Concerning mechanics, we are already studying a self-supporting calorimeter, with a cradle holding the entire structure, for which a cost of 50 K€ overall can be estimated.

In the paragraphs devoted to the calorimeter (Sec. 5.4) we have described a few options for the photo-sensors, that will be decided on the basis of R&D studies and test-beams. As baseline for the cost estimate we rely on the quotation for APD sensors, 5×5 mm^2, of ~ 150 € (VAT included, for a large production).

In order to properly shape and amplify the light signal from the sensors, front-end electronics is needed (as discussed in Sec. 5.4), with a proper adapter board, cabling, and also we need to provide power to the FEE and the sensors themselves. For a complete custom-made system, based on the experience with the production of the large angle veto FEE for the NA62, MU2E and other experiments (done in Frascati electronics workshop), we expect an overall cost of the order of 128 K€.

In Tab. 10.3 we summarize the cost (and the breakdown per year) for the calorimeter up to the FEE electronics.

We are also studying an alternative layout, in which the distance target–calorimeter is doubled (from 2 to 4 m) and – as a consequence – to keep the acceptance, the radius of the calorimeter is also doubled. This allows to realize larger crystals, 2×2 cm^2, but of course requires **four times** more L3 BGO elements. The Moliére radius of BGO is such that this granularity will still be fine (and indeed the original L3 calorimeter cells were slightly bigger), but the missing mass resolution will improve due to the longer baseline. Moreover, in the hyphotesis that we can get the L3 crystals, the cost of the cutting will be significantly reduced, since only the work for reducing to a square prism the trapezoidal original crystal, without the additional cuts for getting four elements out of one piece.

The number of channels will be of course the same, but we probably have to equip the larger crystals with larger photo-sensors. By using, e.g. 10×10 mm^2 APDs, we can expect a cost of the order of 300 €/piece, that could be partially compensated by the reduced costs of the cutting and polishing.

We also expect a significant increase in the cost of the (much) larger vacuum vessel.

Item	2015	2016	2017	2018	Total
			K€		
FADC DAQ boards		22	218		**240**
MCX 8-channels cables kit			31		**31**
VME 6U crates			12		**12**
Acquisition servers			11		**11**
Optical links			6		**6**
Total		**22**	**278**		**300**

Table 10.4: Summary table of the costs of the DAQ system, dominated by the digitizing system for the calorimeter.

LYSO option

We have investigated also the possibility of building our calorimeter purchasing new inorganic crystals. One of the few selectable materials, as discussed in the calorimeter chapter, is the LYSO. A full cost estimate would require dedicated studies and the redesign of the detector. In order to have an order of magnitude of the cost, if we just replace the cost for cutting and polishing of L3 BGO crystals of 51 K€, with the estimated cost of 520 K€ for a same size and granularity LYSO detector, based on an estimated cost of 650 Eur (+VAT) per crystal (for large quantities).

10.1.5 DAQ, servers, cables

The readout of the main detector of PADME, i.e. the calorimeter, will be done using switching-capacitor digitizers, 12 bit resolution, 5 GS/s, based on the DRS4 ("Domino") chip. From preliminary quotations we can estimate 270 €/channel (VAT excluded). For all the boards neeeded for the entire (656 channels) calorimeter we expect then 180 K€. We have then to add the readout for the diamond (32 channels), the small angle calorimeter (32 channels), which also will be done by acquiring the waveforms. Adding three spare boards, we sum up to 210 K€.

To this cost we should add two VME crates (5 K€/unit), two servers (5 K€/unit) for the acquisition equipped with optical links (2.5 K€/unit), and MCX cables ($\sim$100 €/unit). As summarized in Tab. 10.4, the total cost for the acquisition system is of the order of 300 K€.

10.1.6 Trigger distribution, computing, calibration, services

An important aspect of the PADME setup will be the vacuum pipe for the decay region of the dark photon. The requirements in term of pressure will be relaxed, since we just want to keep the equivalent thickness of residual gas up to the calorimeter front surface, to a negligible fraction with respect to the active target. The greatest uncertainty is – at this level – the distance from the target to the calorimeter, and thus the overall dimensions of the vacuum vessel. We are estimating a 50 K€ for the "small" version, that can possibly increase in case we will go to the 4 m distance with larger calorimeter (we foresee additional 40 K€ for this purpose in 2018). We also foresee 16 K€ for the pumping system and 20 K€ for the integration of the mechanics and vacuum with the accelerator systems (including controls, feed-back and interlocks, safety system, etc.).

The computing model has been described with some detail in the dedicated chapter, together with a first estimate of the related costs (Sec. 7.11). We expect the largest part of the cost for offline computing and dedicated storage.

Concerning the trigger distribution, we will need a system for the proper distribution of the

Item	2015	2016	2017	2018	Total
	K€				
Magnet	3	20			**23**
Diamond target	2	70			**72**
Calorimeter BGO	20	234	96		**350**
Small angle calorimeter			41		**41**
Vacuum and mechanics		35	20+16	40	**111**
Charged particles veto		54	50		**104**
Calibration			20		**20**
Imaging charged veto				150	**150**
FADC DAQ boards, servers+links, cables		22	278		**300**
TDC + VME controller			29		**29**
Trigger distribution			30		**30**
Computing and storage			60	40+20	**120**
Total	**25**	**435**	**640**	**250**	**1350**

Table 10.5: Summary table of the costs of PADME detector elements per year in the period 2015–2018.

digital signals, with a suitable jitter (< 50 ps) and the proper format. We expect a cost for such equipment of the order of 30 K€.

An additional item to be considered for the calorimeters is a calibration system, in order to monitor and calibrate the response of each single channel of the main calorimeter and of the veto detectors, for which we estimate a cost of about 20 K€.

Summarizing, the overall costs for the PADME detectors, acquisition, trigger, computing and services are listed in Tab. 10.5, together with the cost evolution year by year.

10.2 Time line

A preliminary timeline for the construction of the PADME setup, including all the main elements, is show in Fig. 10.2: it can be clearly seen that the most complex system is the main crystal calorimeter, in particular cutting, wrapping, mounting of the photo-sensors, assembly in the mechanical support are operations that have to be completed before instrumenting the detector with front-end electronics and perform the last steps of integration and commissioning. Some interaction is also present with the vacuum system, that has to be completely designed before freezing the details of both the active target and positron veto detectors, which are in vacuum or just mounted on the external surface of the vessel. Considering that the refurbishing of the magnet is already under way and that R&D on the calorimeter readout and scintillators already started in the second half of 2015, we expect that one and a half year is needed for starting a commissioning run of the experiment, if proper funding is granted.

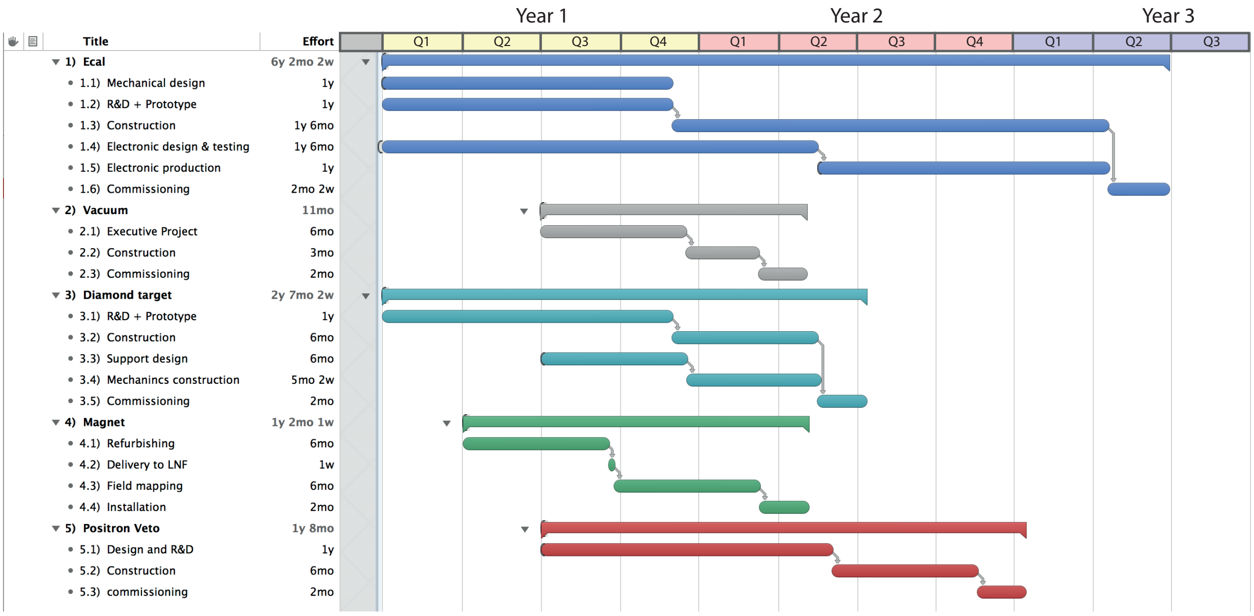

Figure 10.2: Preliminary GANTT chart for the construction of the PADME detectors.

Chapter 11

Conclusions

Concluding we compare the PADME sensitivity to other planned experiments in the world. There is a wide panorama of experimental techniques which will provide a large international community working in the field in the upcoming years.

11.1 Comparison with competitors

Due to the weak experimental signature, the search for invisibly decaying dark photon requires carefully designed dedicated experiment. Following the publication of the DP search by NA48/2, which completed the effort to constrain the region preferred by the muon $(g-2)_\mu$ anomaly in the hypothesis of DP decay to SM particles only, new attention has been devoted to 'invisible decays" models both theoretically and experimentally. In the following section we will give a detailed description of the future experiment searching for invisible dark photon decays. Not all of them are dedicated experiments and in some case the invisible sensitivity is a by product of a visible experiment.

VEPP3

The first experimental proposal to search for the dark photon in e^+e^- annihilation is described in [19]. The search method is based on a missing mass spectra in the reaction $e^+e^- \rightarrow \gamma A'$ using a positron beam incident on a gas hydrogen target, internal to the VEPP3 storage ring. It allows observation of the A' signal independently of its decay modes and life time. The internal hydrogen target and positron beam at VEPP3 allow a routine operation at a luminosity of at least 10^{32} cm^{-2}s^{-1} with the possibility of increasing by a factor of 5–10. In a six-month run the total accumulated statistics will be $3.5\cdot 10^{11}$ events, assuming 75% efficiency of time utilization. In Figure 11.1 a top view of the VEPP3 hall in the vicinity of the internal target equipment and possible locations of the photon detector are shown. In the proposal there is no definite solution for the calorimeter but a combination of PRIMEX and CLEO-II dismissed calorimeters, placed at an 8 m distance from the target is proposed. To reject the main background coming from photons emitted by bremsstrahlung in the target a positron veto is placed in front of Q2. (see Figure 11.1). The veto collects positron deflected by dipole D2 due to their energy loss associated to the emission of the radiated photon. The detector is composed of a sandwich of tungsten and plastic scintillators is divided in two parts, to avoid crossing the beam plane region where the rate of radiated photons is extremely high. The veto is expected to provide a rejection factor of 50 for the bremsstrahlung background. A preliminary study of the sensitivity based on calculations using a benchmark mass

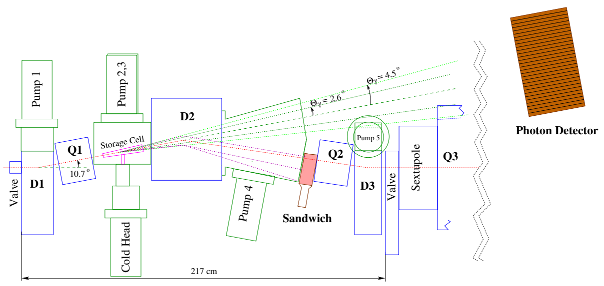

Figure 11.1: Layout of the VEPP3 experimental setup.

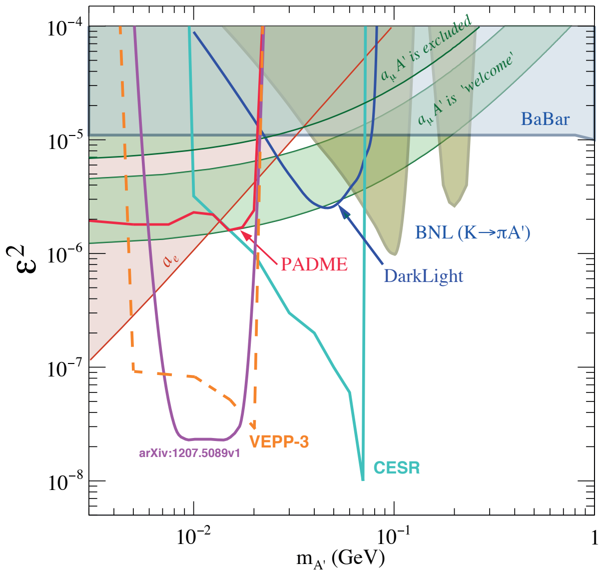

Figure 11.2: VEPP3 expected exclusion limits in the invisible channel.

of 15 MeV for the A' allowed to identify the region which will be accessible to the search in the VEPP3 experiment (see Fig. 11.2 purple line). More recent sensitivity evaluation based on new background and acceptance estimates led to the results shown by the dashed orange line in Fig. 11.2 (adapted from [53]).

Cornell

Recently a new proposal to search for the invisible decay of the dark photon has been presented at Cornell's Wilson Laboratory [54]. The experiment proposed searches for the process $e^+e^- \to \gamma A'$ in events with a positron beam extracted slowly from the CESR storage ring over an energy range 4.7–5.3 GeV, incident on a Be fixed target, and aimed at a calorimeter of CsI crystals located some distance further downstream. The ordinary photon in the final state is observed and its four-momentum is measured by the segmented EM calorimeter; the undetected A' will appear as a bump in the recoil-mass spectrum, $M^2_{rec} = (P_e + P_{beam} - P^2_\gamma)$. The calorimeter is an annular configuration of CsI crystals located about 10 m from the target. The crystals, are recovered from the CLEO endcap calorimeters, are $5 \times 5 \times 30$ cm^3 rectangular solids, well suited to stacking in simple arrays.

To assure and angular coverage $2° < \theta_\gamma < 5°$ the total number of crystals needed is about 700. As a precaution against charged particles that may reach the calorimeter, a set of scintillator slats will cover its front face, and a sweeping magnet is located just after the target to remove low energy ones. Each slat is 5 cm wide, matching the crystal size, and the slats are organized in both horizontal (x) and vertical (y) groups so a single crystal can be vetoed by an x–y coincidence. The non-interacting beam positrons are absorbed in a beam dump located downstream from the calorimeter. The planned detector configuration is illustrated in Fig. 11.3.

Within the accessible dark photon mass window provided by the 5 GeV positron beam (up to ~ 70 MeV$/c^2$) the Cornell experiment will probe values of ϵ in the range $10^{-3} - 10^{-4}$. The expected performance of the experiment, based on GEANT4 simulation, are shown in Fig. 11.4, which indicates the region of the parameter space of coupling constant versus mass that this experiment

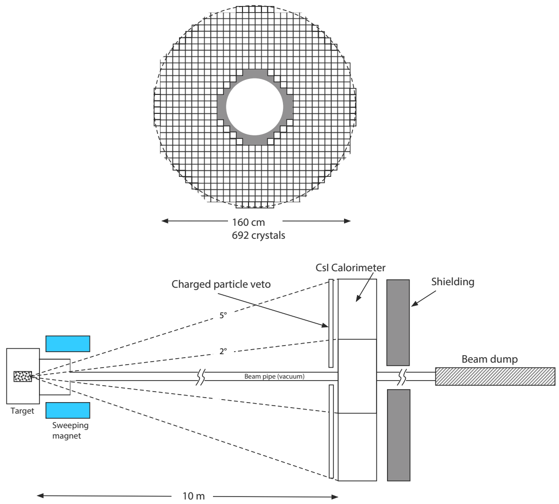

Figure 11.3: Layout of the Cornell experimental setup.

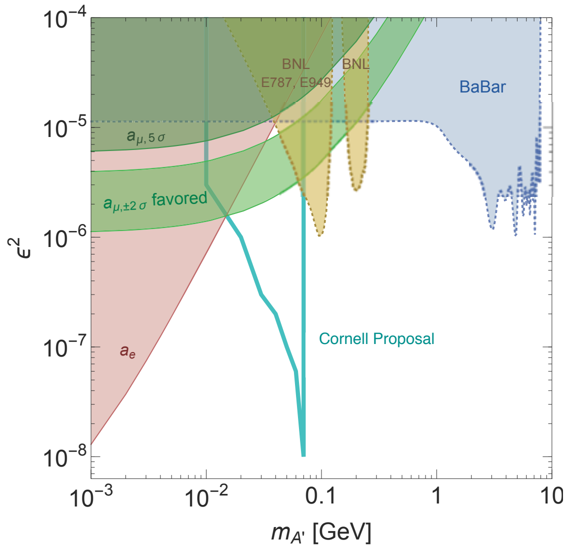

Figure 11.4: Expected exclusion in the invisible channel for the Cornell proposal.

can exclude with a run of 10^7 seconds. The collaboration is currently looking for a financial support.

P348 at CERN

A recently proposed experiment at CERN SPS [55] would also search for invisible A' decays. The experiment employs an innovative technique, by having the primarily e^- beam from the H4 line at SPS, with energy between 10 and 300 GeV, impinging on an active beam-dump, made by a calorimeter based on scintillating fibres and tungsten, ECAL1. A nearly-hermetic detector would be located behind the active beam-dump. The detector is made by a charged particle veto counter, a decay volume, two scintillating fibre counters, a second electromagnetic calorimeter ECAL2, and an hadronic calorimeter. The experimental setup, shown in Fig. 11.5, is optimized to search for visible A' decays. The expected sensitivity for different accumulated statistics is shown in Fig. 11.6. The assumed beam energy is 30 GeV.

The experiment could also search for A' invisible decays by exploiting the detector hermeticity, and requiring a single hit in ECAL1 from the e^- radiating the A' with an energy lower than 10% of the primary beam energy. The projected sensitivity for $3 \cdot 10^{12}$ electrons on target covers a very large region in the DP parameter space, with $m_{A'} < 1$ GeV and $\epsilon > 1 \cdot 10^{-5}$ (see Fig. 11.7). The orange and green lines show the expected 90% C.L. exclusion areas corresponding, respectively, to 10^9 and 10^{12} accumulated electrons at 30 GeV (dash-dotted) and 100 GeV (solid) for the background free case. To accumulate required number of electrons, a data taking period of at least 3 months is requested. Recent reanalysis [21] of the physics potential of P348 reports that the signal yield estimate at 90% C.L. exclusion is ~20-30 times lower than what is inferred from Fig. 11.7. In the event of a positive signal, the experiment would carve out a contour in the parameter space, but would not independently measure the A' properties. The experiment will have its first test run in the end of 2015 at H4 line at SPS to study beam related background.

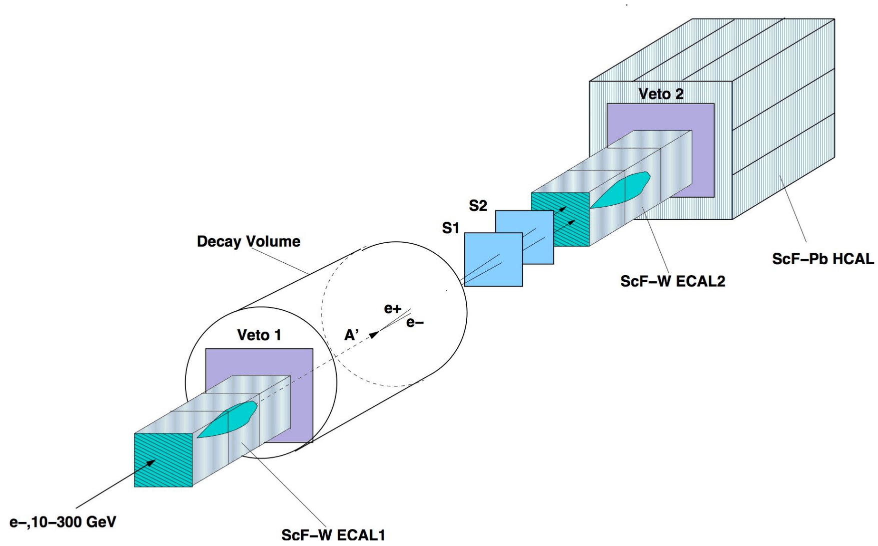

Figure 11.5: Layout of the P348 experimental setup.

Belle II at KEK

Belle II experiment at the SuperKEKB collider is a major upgrade of the Belle experiment at the KEKB asymmetric e^+e^- collider at the KEK laboratory in Japan. The upgrade of the new B-factory SuperKEKB, with a designed luminosity of $8 \cdot 10^{35}$ cm^{-2} s^{-1}, is almost finished. The Belle II experiment will focus on the search for new physics beyond the Standard Model via high precision measurement of heavy flavour decays and search for rare signals. The upgraded detector will have about 35% better resolution of the dimuon invariant mass and the sensitivity to $A' \to l^+l^-$ decays can be improved [56]. This will be done through an implementation of a low multiplicity trigger. In addition, the collaboration is also investigating the possibility to implement a single photon trigger similar to the one used in BaBar [22] to search for invisible decays of the A'. Due to the very high luminosity of the new machine the mono photon trigger will be an experimental challenge. No official statements are available on whether or not it will be implemented. Dedicated sensitivity estimates for the Belle II experiment do not exist yet and projections were obtained by scaling of the BaBar results for both the dilepton [20] and the mono photon result [22]. Exclusion limits for invisible case are shown in Fig. 11.7. First collision at the SuperKEKB are currently foreseen for mid 2017, while physics run is expected to start in October 2018.

BDX at Jefferson Laboratory

In the BDX experiment [57], a O(m^3) calorimeter will be installed behind one of the Jefferson Laboratory high intensity experimental Halls (A and C). High energy (11 GeV) electrons from the CEBAF accelerator will impinge on the beam-dump, possibly producing a secondary dark matter beam. Dark matter particles will be detected trough the scattering on the detector material (electrons and quasi free nucleons), resulting in a visible energy deposition (see Fig. 11.8 for an experiment schematic). In the foreseen setup, a O(m^3) detector is placed downstream with respect to the beam-dump, surrounded by an active veto system and by passive shielding to reduce the number of hits due to cosmogenic backgrounds (muons and energetic neutrons).

The BDX experiment reach has been computed by evaluating the foreseen number of background

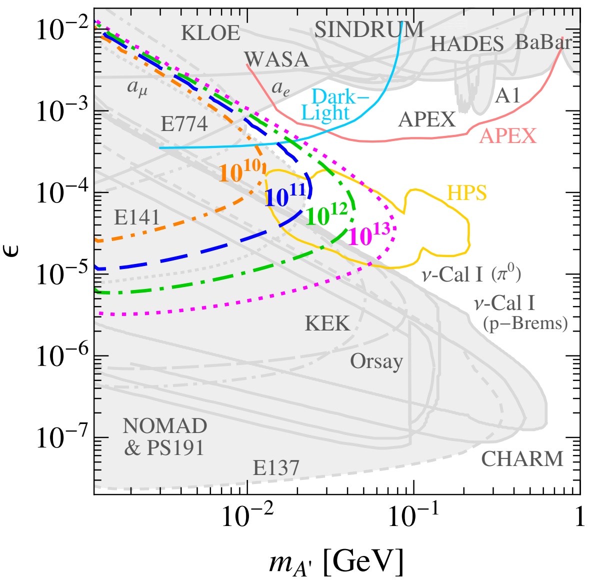

Figure 11.6: Expected 90% C.L. exclusion for different collected statistics of the P348 experiment.

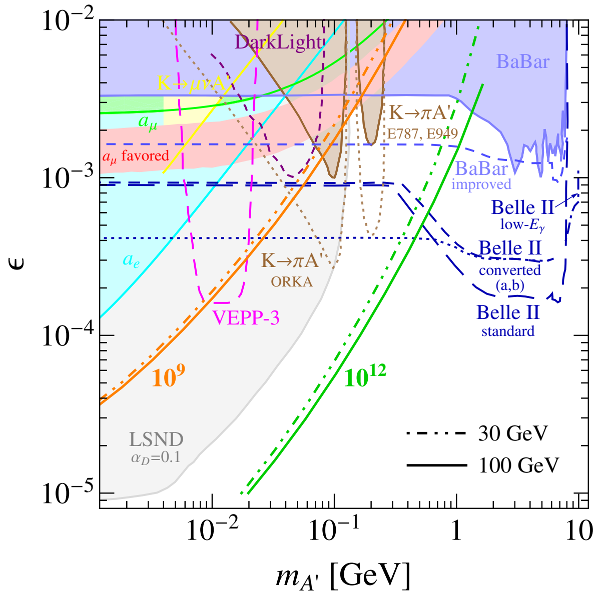

Figure 11.7: Expected exclusion in the invisible channel for the P348 proposal and for the Belle II experiment.

hits in the detector through detailed Montecarlo simulations, and comparing this to the expected number of signal events (as a function of the model parameters). Red curves in Fig. 11.9 show 10, 100, and 1000 event BDX yield projections for a kinetically-mixed dark-photon (A') coupled to a nearly-invisible fermion χ in the quasi-elastic nucleon recoil channel with 10^{22} eot. Similar sensitivity can be achieved in the electron recoil channel giving to BDX the unique capability of being sensitive to different DM interaction mechanisms at the same time. The region potentially covered by using the Jefferson Laboratory beam would therefore extend significantly the parameter space already excluded by previous experiments. A Letter of Intent [57] has been submitted to PAC 42 of the Jefferson Laboratory in mid 2013. The collaboration has been encouraged to perform further studies and to produce a Technical Design Report which is expected for the end of 2015.

11.2 Discussion

Searches for dark photons are well motivated by recently observed phenomena. The PADME experiment will be able to perform such a search exploiting the present linac of the DAΦNE facility in just one-two year of running. The expected sensitivity region with masses up to 24 MeV/c^2 and values of $\epsilon^2 < 10^{-6}$ lies exactly in the region, preferred by the $g_\mu - 2$ data, as seen in Fig. 9.7. It partially overlaps with the result of the combination of the measurements of $(g_e - 2)$ and α_{EM}, exploiting tenth-order calculations of the QED contributions. That region is still of high interest since no direct search for a A' has been performed accessing it and because of the recent shift by more than 7σ [63] of the theoretical prediction for g_e due to an error in the calculations. The PADME experiment could be the first to directly constrain the invisible channel. An upgrade of the BTF positron beam energy will extend the sensitivity of PADME to higher A' mass.

Combining the exclusion limits from PADME and the Cornell proposal, significantly extending the reach in a complementary region of higher mass, with the existing BaBar mono-photon con-

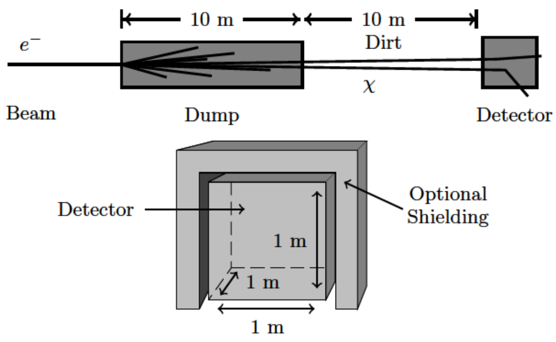

Figure 11.8: Schematic of the BDX experimental setup.

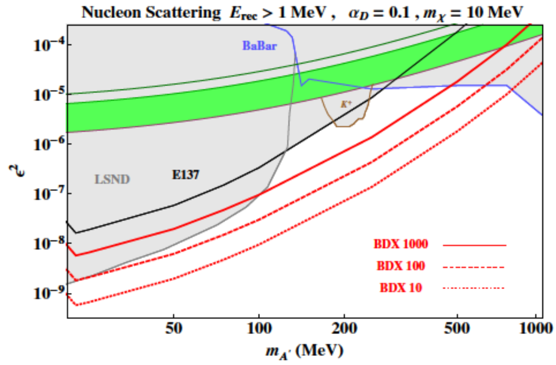

Figure 11.9: Expected exclusion in the invisible channel for the BDX proposal for $\alpha_D = 0.1$ and $m_\chi = 10$ MeV.

straints, most of the preferred $(g-2)\mu$ region could be covered by direct searches in the decay to invisible hypothesis as well. In addition being both PADME and the Cornell proposal measurement completely model independent extremely strong constraints on the theory will be derived not only in the minimal dark photon scenario.

Chapter 12

Appendix: Extended physics program

This proposal is centered on the opportunity of performing a search for a new particle, manifesting as a narrow peak in the missing mass distribution in annihilation events $e^+e^- \to \gamma +$ missing energy (Fig. 12.1), and the experimental setup, as well as the positron beam, are optimized for this main physics objective. However, the possibility of extracting a positron as well as electron beam with a wide range of energy and intensity, allows performing a series of interesting measurements in the field of dark photon or – more in general – long-lived particles.

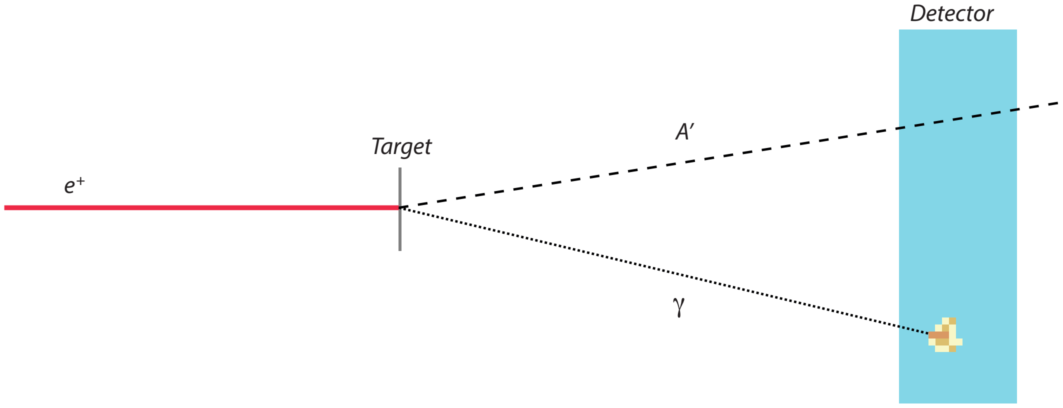

Figure 12.1: PADME-invisible looks for $e^+e^- \to \gamma +$ missing energy events.

Generally speaking, we can classify possible experiments, according to the thickness of the target, e.g. whether the products of the electromagnetic interaction are absorbed ("thick") or not ("thin"), and the final state: "invisible", just looking at Standard Model photon and missing energy, or lepton pairs (Tab. 12.1).

	"Thin" target	**"Thick" target**
$A' \to \gamma$ **nothing**	PADME-invisible	χ scattering (BDX@LNF)
$A' \to e^+e^-(\mu^+\mu^-)$	PADME-visible	PADME-dump

Table 12.1: General classification of PADME experiments.

Apart from the annihilation, typical of the PADME (invisible) approach, both in the thin and in thick target cases, the dark photon production mechanism is dominantly the A'-strahlung on the target nuclei field, so that the primary beam can be indifferently electrons or positrons (the first being much easier to produce and accelerate than the latter). This is a relevant point, since a much wider range of energy and intensity can be accessed using the primary electron beam, i.e. without the necessity of producing positrons on a dedicated target (see Tab. 4.2).

In the following sections we discuss the potential of those experimental techniques exploiting the DAΦNE linac beam and the Frascati infrastructure, in case in a subsequent phase of the PADME initiative, after the realization of PADME-invisible.

12.1 PADME-visible

As already underlined, using the more probable A'-strahlung production from the interaction of e^+ or e^- on the target nuclei, instead of the annihilation of positrons on the target electrons, implies losing the closed kinematics of the $e^+e^- \to \gamma A'$ process (where the ordinary photon is detected), unless the momentum of the recoiling electron p' is measured:

$$e^-(p)N \to e^-(p')NA',$$

since the radiated (dark) photon will exhibit the typical $1/E$ spectrum. Since the missing mass technique cannot be exploited, the only possiblity is searching for the decay of A' to Standard Model particles (e^+e^- pairs and $\mu^+\mu^-$ above the di-muon threshold), the so-called "visible" decay (see Fig. 12.2).

If on one side the energy taken by the A' is unknown, on the other this energy is no longer constrained to the center-of-mass energy $\sqrt{2m_eE_0}$ as in the annihilation case, and much higher masses of A' – up to the beam energy E_0 – will be accessible. Indeed the distribution of the energy fraction taken by the dark photon peaks sharply at 1, so that it will be emitted almost collinear to the beam direction: $\theta_{A'} \sim (m_{A'}/E_0)^{3/2}$. The e^+e^- pair from the decay of the A' will open by an angle $\sim m_{A'}/E_0$.

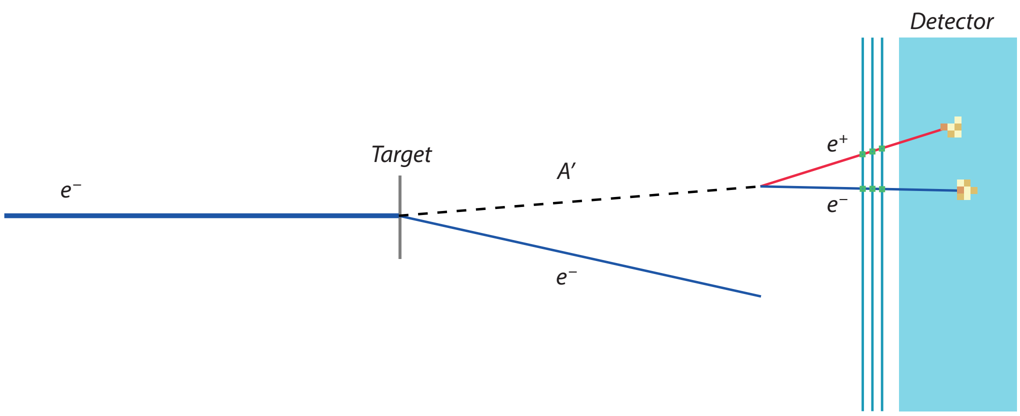

Figure 12.2: PADME-visible can search for $A' \to e^+e^-$ decays, with a dark photon produced in A'-strahlung on a thin target.

Contrary to the annihilation case, for this kind of experiment a high-Z target is desirable, since the A'−strahlung will be enhanced, even though also the ordinary Bremsstrahlung cross section will increase. Another advantage of not relying on the estimated quadri-momentum of the A' is that there is no need of requiring a very thin target, in order not to spoil the missing mass resolution, due to the uncertainty on the A' production point. The thickness of the target can thus be optimized as a compromise between the A' yield, and acceptance for very low decay lenghts.

For our estimates, we have considered a 750 MeV electron beam, i.e. the maximum currently available in Frascati, impinging on 0.5 mm Tungsten target.

The experimental technique is thus pretty simple:

- search for electron and positron pairs simultaneously detected on either side of a magnetic spectrometer;
- measure the momentum of both particles: p_+ and p_- and compute the invariant mass:

$$M_{inv}^2 = \underline{p}^2(e^+) + \underline{p}^2(e^-);$$

- search for a narrow peak in the M_{inv}^2 distribution.

Two main sources of background have to be considered, both producing the same final state as the signal ($e^- A'$, $A' \to e^+e^-$): ordinary Bremsstrahlung on the target, followed by a pair conversion, and the Bethe-Heitler process. Since there are three electrons in the final state, they are also called "tritons". The corresponding Feynman diagrams are shown in Fig. 12.3.

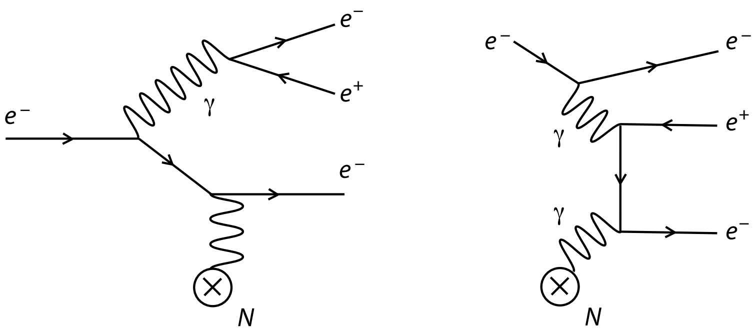

Figure 12.3: The three-electrons background (also called "tritons") for $A'-$strahlung in the interaction of e^- on a thin target, followed by dark photon decay to e^+e^-: on the left the ordinary Bremsstrahlung followed by a conversion, on the right the Bethe-Heitler process.

Concerning the intensity of the beam, the DAΦNE linac routinely delivers 1–2 nC of electrons, in 10 ns long pulses. Recently a series of measurements have been performed after the upgrade of the gun pulsing system, demonstrating that the same current is drawn from the gun cathode when applying longer waveform pulses, so that a linearly increasing charge is delivered when the pulse lenght is increased. Charges in excess of 10 nC in 40 ns long pulses have been measured, i.e. $3 \cdot 10^{12}$ electrons/s could in principle be delivered at 50 Hz repetition rate. However the limiting factor will be the density of charged tracks in the spectrometer, so that a much lower charge can be envisaged. In addition, radio-protection issues have also to be taken into account.

Even considering the maximum allowed average intensity allowed inside the BTF experimental hall ($3.25 \cdot 10^1 0$ particles/s), a full year of operations would allow reaching $\mathcal{O}(10^{18})$ eot. A preliminary estimate of a PADME-visible experiment, gives a sensitivity of the order of $\epsilon^2 \sim 10^{-7}$ in the low mass range, getting worse as higher A' masses are explored (up to the kinematical limit E_0).

12.2 PADME-dump

Assuming that the maximum electron charge produced and accelerated by the DAΦNE linac can be driven to a suitable beam-dump, we can estimate the potential of a PADME-dump experiment.

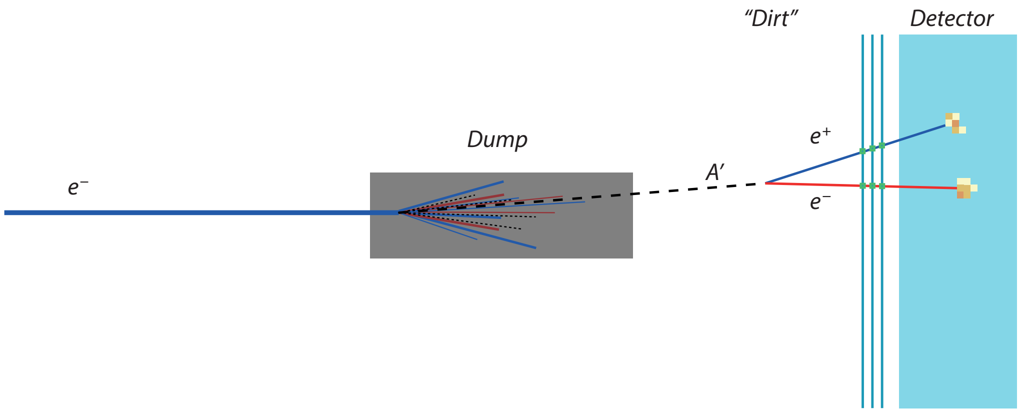

Figure 12.4: A classical dump experiment looks for e^+e^- decays of the dark photon, after having absorbed all the electromagnetic products of the interaction of the primary electron with the target.

As described above, the charge in the beam pulse accelerated by the linac linearly increases as the pulse duration is increased, up to 40 ns. In addition, by increasing the pulse height applied to the linac gun for extracting the electrons emitted by the cathode, we can further increase the beam charge (see Fig. 12.5). Even considering saturation effects, a conservative estimate of 25–30 nC/pulse would give us of the order of 10^{20} eot/year.

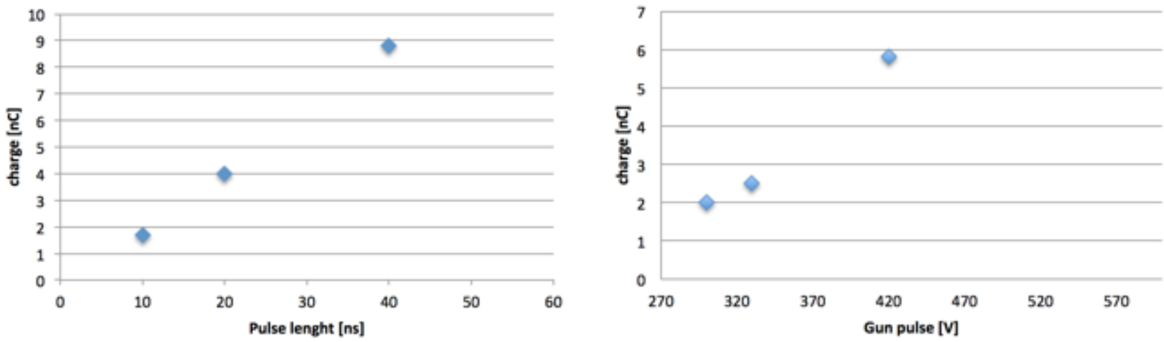

Figure 12.5: Measured linac beam pulse vs. pulse lenght (left) and height (right) applied to the gun.

Of course a suitable area should be identified in order to safely dump the full linac beam onto a high-Z target, keeping the radiation level in accessible areas within the required limits. At the end of the transfer-line from the DAΦNE linac to the accumulator (damping ring) a beam-dump is indeed already present for absorbing particles in event of a beam loss from the last 45° (pulsed) bending. This can be evaluated as an area to be adapted as target station for beam-dump experiments, in case with modifications to the biological shielding.

In Fig. 12.6 the hatched area represents the concrete wall inside which the beam-dump cavity, covered with lead bricks, has been realized, just at the end of the linac to accumulator transfer-line. Behind this dump, shown by the shaded area, a hall hosting part of the cooling pumps and pipes for the damping ring cooling, can be considered for hosting an experimental setup. Further, detailed studies, are needed in order to evaluate the modifications to the infrastructure, and in particular the impact on the other LNF facilities, complexity and costs, however the possibility of performing this kind of experiments should be explored thoroughly.

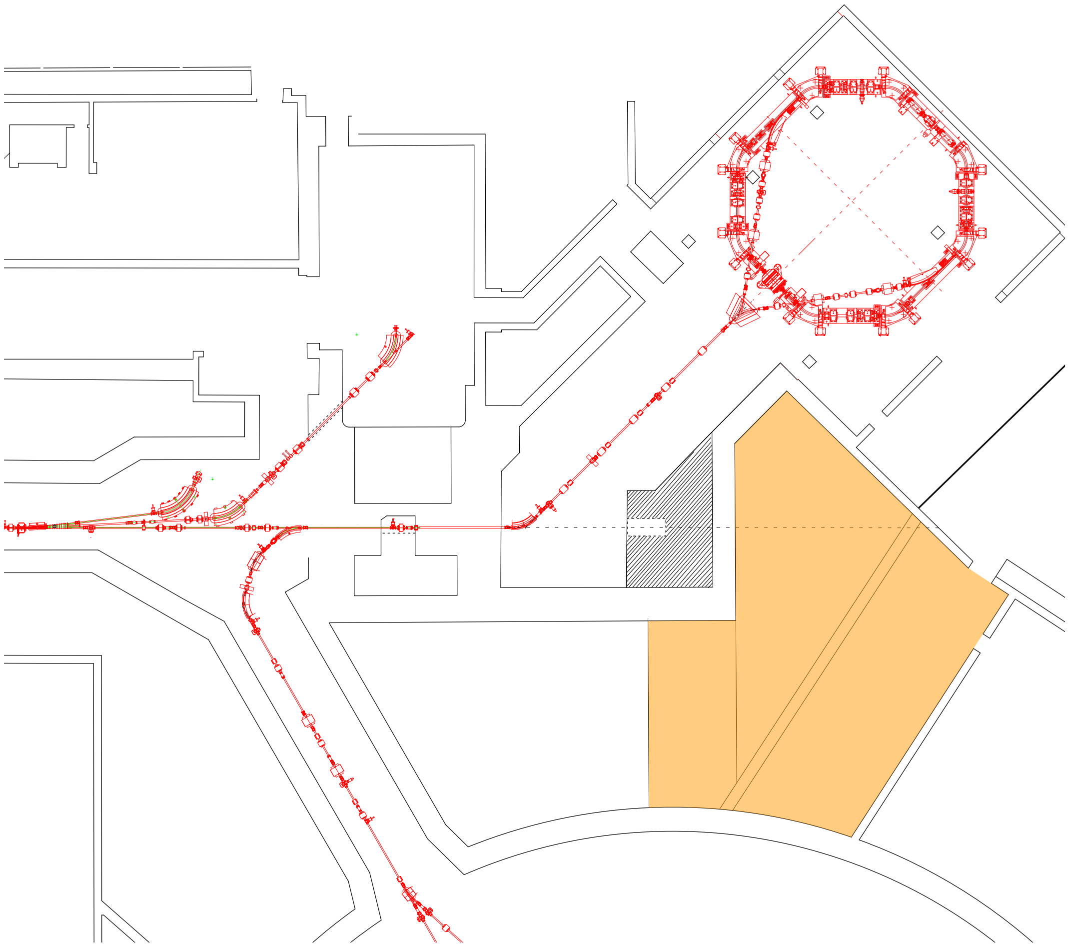

Figure 12.6: At the end of the transfer-line from the DAΦNE linac to the accumulator (damping ring) a beam-dump is present for catching lost beam from the last 45° (pulsed) bending. The hatched area represents the concrete wall inside which the beam-dump cavity, covered with lead bricks, has been realized. Behind this dump, shown by the shaded area, a hall hosting part of the cooling pumps and pipes for the damping ring cooling, can be considered for hosting an experimental setup.

In order to have an estimate of the sensitivity, a simplified Monte Carlo simulation (no interaction with matter) has been developed, following the steps listed below:

- Production cross section are calculated by MADgraph;
- Produced number of dark photons is computed;
- Dark photon number is scaled by decay length acceptance;
- Scale by electron acceptance in the detector using kinematical distribution;
- Distribution is compared with MADGraph for several $M_{A'}$ values.

The production of A' is simplified and only primary electrons are considered at the edge of the target (production along the depth of the dump by electrons having lost some energy has been not implemented).

With these approximations, we have estimated the sensitivity of an experiment modeled on the PADME-invisible setup, i.e. a 20 cm aperture for a magnetic spectrometer (we consider the MBP-S available magnet), placed at 50 cm distance from a 8 cm deep Tungsten target. The sensitivity for 10^{20} eot, 1.2 GeV energy, is shown in Fig. 12.7. The contribution of di-muon events at higher A' masses is also shown.

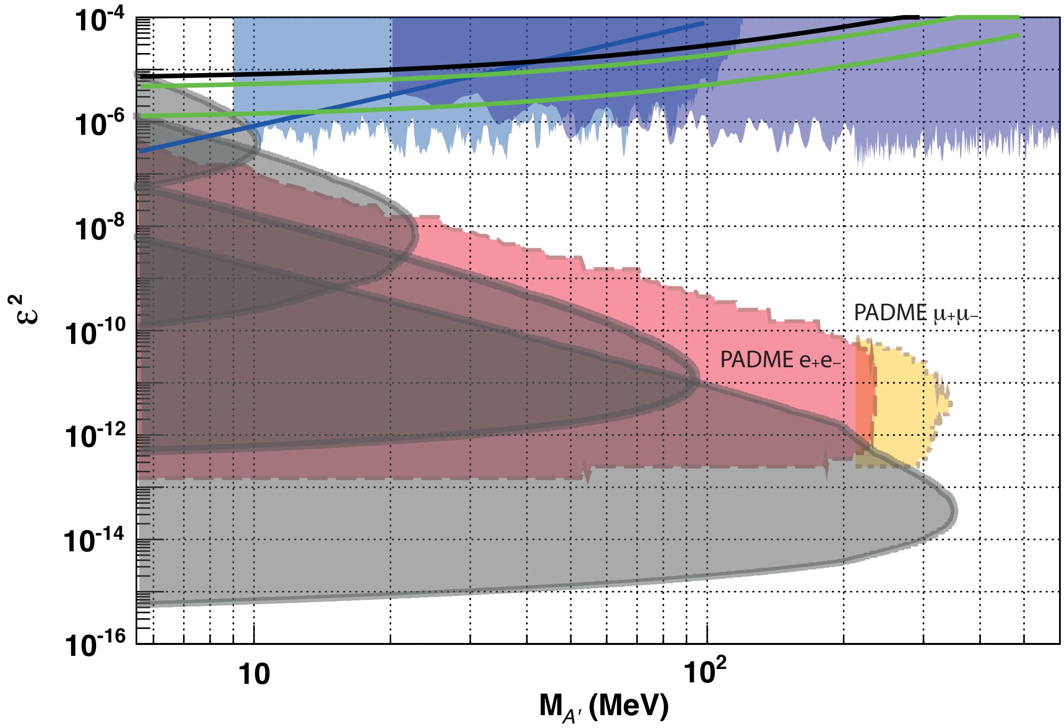

Figure 12.7: PADME-dump sensitivity for e^+e^- and $\mu^+\mu^-$ final states.

12.3 BDX@LNF

As briefly discussed in Sec. 11.1, an alternative approach for searching dark photon "invisible" decays, is to look for the scattering of daughter particles of the dark sector, i.e. coming from a decay chain $A' \to \ldots \to \chi\overline{\chi}$, scattering on the material of a massive detector (on the atomic electrons or on quasi-free nucleons) (see Fig. 12.8). As in "classical" dump experiments the detector should be placed behind a deep shielding capable of absorbing all the secondaries generated by the interaction of the beam with the target, but in order to reduce the contribution of muons and neutrons from the cosmic rays, passive and possibly active veto systems should be added.

Even though both the energy and intensity available with the DAΦNE linac are significantly lower than other accelerators, in particular CEBAF at Jefferson Laboratory, where the 11 GeV electrons are dumped from the quasi-continuous wave accelerator, allowing to reach $\mathcal{O}(10^{22})$ eot that is the intensity at which the BDX proposal is aiming, the time structure, pulsed at 50 Hz, and the perspective of upgrading the DAΦNE linac up to 1–1.2 GeV, stimulated some preliminary

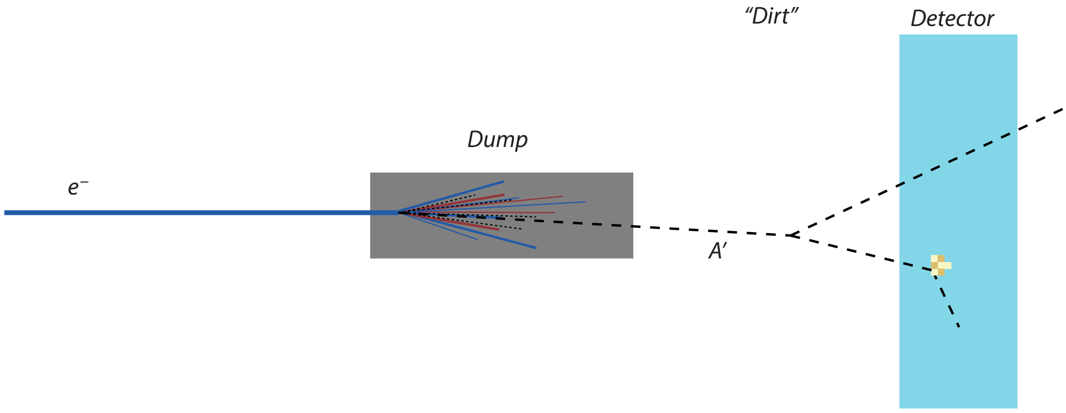

Figure 12.8: Scattering experiments need a recoil detector due to the interaction of A', with a dark photon produced in $A'-$strahlung on a thick target absorbing all the electromagnetic background.

studies of the sensitivity of a BDX-like experiment in Frascati [67]. In Fig. 12.9 two exlusions plots are shown, fixing the coupling costant to $\alpha_D = 0.1$ and a mass for the daughter dark sector particles of $m_\chi = 10$ MeV$/c^2$, for the scattering on electrons and quasi-free protons, the solid line limit is obtained for $2.5 \cdot 10^{20}$ eot, using a recoil detector of $60 \times 60 \times 225$ cm^3, made by scintillating crystals, e.g. reusing the CsI(Tl) crystals from the BaBar electromagnetic calorimeter. The dashed line shows the same limit by increasing the statistics to 10^{21} eot.

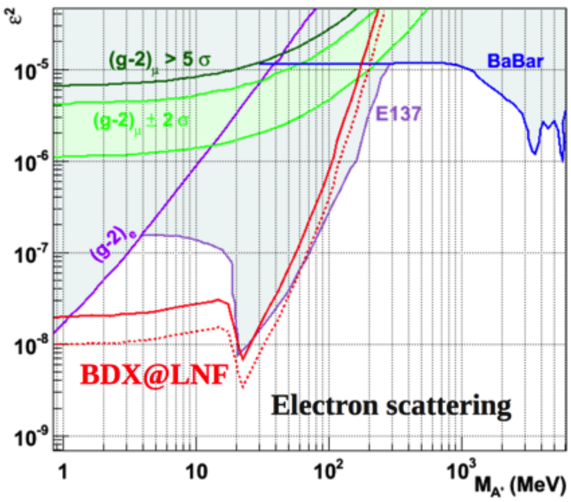

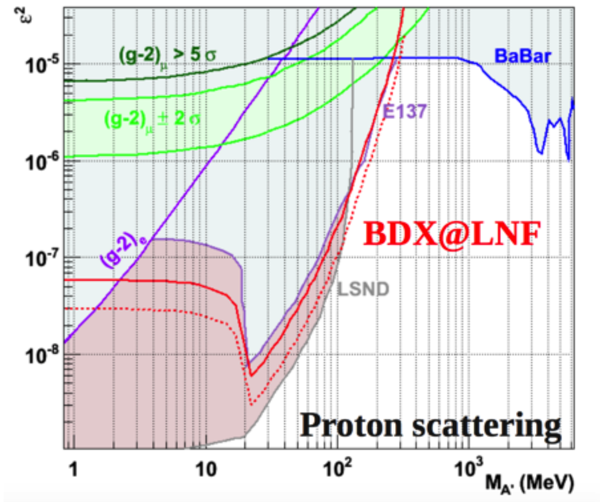

Figure 12.9: Preliminary estimate of a scattering experiment using the DAΦNE linac electron beam, upgraded at 1.2 GeV energy accumulating $2.5 \cdot 10^{20}$ (solid line) or 10^{21} eot (dashed line), on a $60 \times 60 \times 225$ cm^3 scintillating crystals detector (e.g. reusing the BaBar electromagnetic calorimeter): on electrons (left) and on protons (right).

As for the dump experiment at LNF, a suitable location should be identified to cope with radioprotection issues, in order to drive the full electron beam from the linac onto a target. Most probably, an infrastructure similar to what can be foreseen for PADME-dump should be envisaged, with the additional requirement of hosting a sizeable and rather complex detector, at a suitable distance from the production target and with an optimized shielding in front.

Acknowledgments

The PADME experiment idea itself has been taking shape during the process of strategic planning of INFN named “What Next”. We are thus indebted to Antonio Masiero and to the convenors and contributors of the “What Next” working groups and workshops. Among them, we would like to thank especially Franco Bedeschi, former president of the INFN Commissione Scientifica Nazionale I, for having encouraged us constantly and for having given us the opportunity of discussing and improving our idea. A large contribution, in this context, came and is still coming from our referees: Stefano Giagu and Giacomo Sguazzoni, recently joined by Gabriele Simi.

Negotiations for getting the L3 crystals have been patiently carried on by the INFN executive committee, Antonio Masiero and Speranza Falciano in particular, and of course INFN president Fernando Ferroni. Francesca Cavallari and the CMS colleagues from INFN Rome have constantly shared with us their expertise on the crystals.

We would like to thank Davide Tommasini for helping us in finding and getting on loan from CERN the PADME magnet (MBP-S from the SPS transfer line), and Roberto Lopez for the invaluable work in preparing and adapting the magnet for our purposes.

Idea sharing, useful discussions and encouragement also come from a number of distinguished colleauges in the field of secluded sectors, in particular we would like to thank Sarah Andreas, Brian Batell, Jim Alexander, Marco Battaglieri, Andrea Celentano,

Bibliography

[1] R. Essig, J. A. Jaros, W. Wester, P. H. Adrian, S. Andreas, *et al.*, (2013), arXiv:1311.0029 [hep-ph].

[2] J. F. Cherry, A. Friedland and I. M. Shoemaker, arXiv:1411.1071 [hep-ph].

[3] L. B. Okun, Sov. Phys. JETP **56** , 502 (1982) Zh. Eksp. Teor. Fiz. **83** , 892 (1982)

[4] B. Holdom, Phys. Lett. B **166**, 196 (1986)

[5] P. Galison and A. Manohar, Phys. Lett. B **136**, 279 (1984).

[6] G. Anelli *et al.*, CERN-SPSC-2005-013, CERN-SPSC-P-326.

[7] E. Izaguirre and I. Yavin, arXiv:1506.04760 [hep-ph].

[8] B. Echenard, R. Essig and Y. M. Zhong, JHEP **1501**, 113 (2015)

[9] H. Davoudiasl, H. S. Lee and W. J. Marciano, Phys. Rev. D **89**, 095006 (2014)

[10] M. Raggi and V. Kozhuharov, Adv. High Energy Phys. **2014**, 959802 (2014)

[11] J. Jaeckel and M. Spannowsky, arXiv:1509.00476 [hep-ph].

[12] J. D. Bjorken, R. Essig, P. Schuster and N. Toro, Phys. Rev. D **80**, 075018 (2009).

[13] T. Beranek and M. Vanderhaeghen, Phys. Rev. D **89**, no. 5, 055006 (2014).

[14] P. Fayet, Phys. Rev. D **75**, 115017 (2007) [hep-ph/0702176 [hep-ph]].

[15] S. Andreas, C. Niebuhr and A. Ringwald, Phys. Rev. D **86**, 095019 (2012)

[16] S. Alekhin *et al.*, arXiv:1504.04855 [hep-ph].

[17] B. Batell, R. Essig and Z. Surujon, Phys. Rev. Lett. **113**, no. 17, 171802 (2014)

[18] R. Dharmapalan *et al.* [MiniBooNE Collaboration], arXiv:1211.2258 [hep-ex].

[19] B. Wojtsekhowski, D. Nikolenko and I. Rachek, arXiv:1207.5089 [hep-ex].

[20] J. P. Lees *et al.* [BaBar Collaboration], Phys. Rev. Lett. **113**, no. 20, 201801 (2014)

[21] E. Izaguirre, G. Krnjaic, P. Schuster and N. Toro, Phys. Rev. D **91**, no. 9, 094026 (2015)

[22] B. Aubert *et al.* [BaBar Collaboration], arXiv:0808.0017 [hep-ex].

[23] R. Essig, J. Mardon, M. Papucci, T. Volansky and Y. M. Zhong, JHEP **1311**, 167 (2013)

[24] M. Ablikim *et al.* [BESIII Collaboration], Phys. Rev. D **87**, no. 1, 012009 (2013)

[25] A. V. Artamonov *et al.* [BNL-E949 Collaboration], Phys. Rev. D **79**, 092004 (2009)

[26] I. Jaegle [Belle Collaboration], Phys. Rev. Lett. **114** (2015) 21, 211801

[27] B. Buomomo and L. Foggetta, IPAC 2015, Richmond (USA), TUPWA057 (2015).

[28] B. Buomomo, L. Foggetta and G. Piermarini, IPAC 2015, Richmond (USA), TUPWA056 (2015).

[29] G. Mazzitelli, A. Ghigo, F. Sannibale, P. Valente and G. Vignola, Nucl. Instrum. Meth. A **515**, 524-542 (2003).

[30] B. Buomomo, L. Foggetta and P. Valente, IPAC 2015, Richmond (USA), MOPHA048 (2015).

[31] F. Sannibale and G. Vignola, DAΦNE Technical Note LC-2 (1991).

[32] R. Page, CPS Users Handbook, CERN (1974).

[33] F. J. Decker, D. Farkas, L. Rinolfi and J. Truher, SLAC-PUB-7214 (1996).

[34] E. Berdermann for the NoRDHDia, Nucl. Phys. News, 19, 25 (2009).

[35] www.usapplieddiamond.com

[36] H. Spieler, IEEE Trans. Nucl. Sci. NS-29/3,1982,1142.

[37] http://www.cividec.at

[38] E. Alemanno, A. Caricato, G. Chiodini, M. Martino, P. M. Ossi, R. Perrino and S. Spagnolo, Appl. Phys. B113 (2013) 373-378.

[39] E. Alemanno, A. Caricato, G. Chiodini, M. Corrado, G. Fiore, M. Martino, R. Perrino, C. Pinto and S. Spagnolo, Diamond and Related Materials, 38, 32-35 (2013).

[40] G. Chiodini *et al.*, Nucl. Instr. Meth., A730 , 152-154 (2013).

[41] N. Cartiglia *et al.*, JINST 9 C02001 (2014).

[42] F. Burkart *et al.*, in "Proceedings of IPAC 2014, Dresden', THPME172 (2014).

[43] K. A. Olive *et al.* [Particle Data Group Collaboration], Chin. Phys. C **38**, 090001 (2014).

[44] G. Eigen *et al.*, Nucl. Instrum. Meth. A **718**, 107 (2013).

[45] Y. Karyotakis, In "Beijing 1994, Proceedings, Calorimetry" 27-35, and
Annecy Lab. Part. Phys. - LAPP-EXP-95-002 (95/02,rec.Apr.) 9 p. (510187).

[46] http://www.psi.ch/drs/DocumentationEN/DRS4_rev09.pdf

[47] https://indico.inr.ru/event/4/session/13/contribution/60/material/slides/0.pdf

[48] http://advansid.com/attachment/get/up_53_1432731710.pdf

[49] http://sensl.com/products/silicon-photomultipliers/mseries/

[50] http://sensl.com/products/silicon-photomultipliers/cseries/

[51] "The WaveDAQ system for the MEG II upgrade", 13th Pisa Meeting on Advanced Detectors, La Biodola - Elba, 24-30/5/2015

[52] B. Wojtsekhowski, AIP Conf. Proc. **1160**, 149 (2009), arXiv:0906.5265 [hep-ex]
B. Wojtsekhowski, D. Nikolenko and I. Rachek, arXiv:1207.5089 [hep-ex].

[53] I.Rachek, B.Wojtsekhowski, D.Nikolenko, IEBWorkshop Cornell University June 18, 2015, https://indico.classe.cornell.edu/event/38/session/0/contribution/30/material/slides/0.pdf

[54] J. Alexander, "LDM search at Cornell",
http://www.ge.infn.it/ ldma2015/LDMA2015/Program.html

[55] S. Andreas, S. V. Donskov, P. Crivelli, A. Gardikiotis, S. N. Gninenko, N. A. Golubev, F. F. Guber and A. P. Ivashkin *et al.*, arXiv:1312.3309 [hep-ex].

[56] I. Jaegle [for the Belle/Belle II Collaborations], talk given at "International Workshop on Baryon & Lepton Number Violation", 26-30 April (2015).

[57] M. Battaglieri *et al.* [BDX Collaboration], arXiv:1406.3028.

[58] P. Fayet, Phys. Lett. B **675**, 267 (2009).

[59] A.Pukhov *et al.*, Preprint INP MSU 98-41/542,arXiv:hep-ph/9908288
A.Pukhov, e-Print Archive: hep-ph/0412191.

[60] D. Hanneke, S. Fogwell Hoogerheide, and G. Gabrielse, Phys. Rev. A **83**, 052122 (2011).

[61] R. Bouchendira *et al.*, Phys. Rev. Lett. **106**, 080801 (2011).

[62] E. Meschi, T. Monteiro, C. Seez and P. Vikas, CMS Note 2001/034.

[63] T. Aoyama, M. Hayakawa, T. Kinoshita, and M. Nio, Phys. Rev. Lett. **99**, 110406 (2007).

[64] P. Valente, B. Buonomo and L. Foggetta, INFN-14-06/LNF report (2014).

[65] R. Brun, F. Rademakers, Nucl. Instrum. Meth. A **389**, 81 (1997).

[66] S. Agostinelli *et al.*, Nucl. Instrum. Meth. A **506**, 250 (2003).

[67] A. Celentano *et al.*, "What Next" LNF workshop, Nov. 2014,
https://agenda.infn.it/getFile.py/access?contribId=29&resId=0&materialId=slides&confId=8563